

MASTER THESIS

PHYSICS AND ASTRONOMY:
PARTICLE- AND ASTROPHYSICS



RADBOUD UNIVERSITY NIJMEGEN

Learning the Phases of the cpMSSM

CP VIOLATION AND THE DARK MATTER RELIC DENSITY

Author:

Dirren A. P. van Vlijmen

Supervisors:

Prof. Dr. Wim J. P. Beenakker

Jochem W. Kip

Second reader:

Dr. Timothy G. Budd

December 7, 2023

Acknowledgements

Theses are never the work of one person alone, and this thesis is no exception to that rule. Therefore, there are plenty of people that need to be mentioned before the actual content starts. First of all, my two supervisors: Prof. Dr. Wim Beenakker and Jochem Kip, without whom I would not have known, or understood anything, about the wonders of supersymmetry and the possibilities of Machine Learning in it. More specifically, I would like to thank Wim for his ability to always see opportunities, and be willing to work hard for them, for me. Starting when I came to your office for the first time, not expecting to be able to do anything with my ‘Machine Learning requirement’, and ending with the countless hours of essential feedback given in an almost unrealistic tempo. Jochem, thank you for answering the numerous questions that came your way, sometimes multiple times. Also thanks to your colleagues in your office, who did not seem bothered by the number of times I came asking questions. The way you were always able to directly answer these questions, with some humour when needed, was essential to this thesis and my internship, although I would have still liked the weather of your Valencia trip to come along with you to Nijmegen. Further, I also have to thank two contacts from the Data Science department. Dr. Twan van Laarhoven for your broad experience, and especially the help with thinking of validation methods. And Alex Kolmus for your code of, and experience with, normalizing flow models, together with your always-present enthusiasm they made the success of my internship possible. Lastly, gratitude also goes towards Dr. Bob Stienen and Dr. Marrit Schutten. Bob Stienen for guiding me in the right direction of possible models at the beginning, and Marrit for basically guiding me in the right direction for the whole process. For me and this thesis, your PhD thesis is on par with the great literature works of SUSY.

Outside of the people who, knowingly or not, helped me from a technical perspective, my thanks also go out to my family, girlfriend and friends, giving me continuous support and belief when needed, and presenting me with distractions when this was most needed. I hope that you know that this would have never been possible without you.

Abstract

This thesis presents a new sampling method to sample cpMSSM parameter configurations based on pMSSM parameter configurations, while providing a theoretical guide to understand its physics context. The sampler is a normalizing flow model that directly learns to optimize its sampling method with regards to the target distribution. After creating the necessary dataset, and performing a small optimisation of the learning process, the result is an automatic, efficient sampler that generated >50% correct samples. This presents the possibility to more realistically explore and study the parameter space of the cpMSSM. This thesis exhibits this by using the new sampler for a study into the CP-violating effects of the cpMSSM on the dark matter relic density. It is shown that these effects are very restricted by limits on the electron electric dipole moment. However, a novel effect of $\phi_{\mathbf{A}_t}$ on the neutralino composition was also observed.

Contents

1	Motivation: from SM to cpMSSM	3
2	Used Conventions	5
2.1	Used Abbreviations	6
3	Theory	7
3.1	Standard Model	7
3.1.1	Discrete Symmetries	8
3.2	Supersymmetry	8
3.2.1	Supersymmetric Lagrangians	9
3.2.2	Other Supersymmetric Arguments	11
3.2.3	Hierarchy Problem	12
3.3	Minimal Supersymmetric Standard Model (MSSM)	14
3.3.1	Particle Content	14
3.3.2	Introducing Interactions	15
3.3.3	Breaking Mechanism	18
3.3.4	Particle Sectors	19
3.4	pMSSM	24
3.4.1	Parameters	25
3.5	cpMSSM	25
4	Observables	27
4.1	Electron Electric Dipole Moment	27
4.2	Relic Density	31
5	Machine Learning Methodology	34
5.1	Context	34
5.2	Normalizing Flow	35
5.2.1	Motivation	35
5.2.2	Explanation	35
5.2.3	Rational Quadratic Spline	36
5.3	Dataset: The Creation Pipeline	37
5.3.1	pMSSM points	38
5.3.2	Naive Sampling	39
5.3.3	Calculation Software	39
5.3.4	Augmentation Possibilities	39
5.3.5	The Result	40
5.4	Learning	40
5.4.1	The effect of the naive sampling method	41
5.5	The Inference Pipeline	42

6	Model Validation	43
6.1	Likelihood Ratio	43
6.2	Other Methods: Model Characteristics	45
6.2.1	Scatter Plots	45
6.2.2	Volume Approximation	45
6.2.3	Uniformity Plots	46
6.3	Acceptance Percentage	46
6.4	Results	46
6.4.1	Likelihood Ratio	46
6.4.2	Scatter Plots	47
6.4.3	Uniformity Plots	49
6.4.4	Volume Approximation	51
6.4.5	Acceptance Percentages	52
7	Study: CP violation effects on the Relic Density	54
7.1	H_1 -funnel	54
7.2	H_2 -funnel	58
7.3	Z-funnel	61
7.4	Neutralino Co-Annihilation	63
7.5	Chargino Co-Annihilation	66
7.6	Stau Co-Annihilation	68
7.7	Slepton co-annihilation	71
7.8	Sbottom Co-Annihilation	73
7.9	Bulk	75
8	Conclusion and Outlook	77
8.1	Outlook	77
A	Extra Material	83
A.1	All Generic Interactions within Supersymmetry	83
A.2	Couplings	84
A.3	Loop Functions	88
A.4	Augmentation Study	88
B	Additional Figures	90
B.1	Validation Figures Bias-Corrected Model	91
B.2	Scatter plot for a different correct pMSSM point	93
C	Calculation Software	94
C.1	The Software Packages	94
C.2	Visualization of the internal calculation Pipeline	95
C.3	Experimental Limits	95

Chapter 1

Motivation: from SM to cpMSSM

The Standard Model (SM) of Particle Physics stands as the most successful model ever crafted by physicists to explain natural phenomena all around us. It describes all, currently known, fundamental particles within matter (fermions), while also describing their fundamental interactions, mediated by force-carrying bosons. The model's successes range from an extremely accurate 1 in 100 billion prediction of the magnetic dipole moment of the electron [1] to the prediction of the Higgs boson [2] and the heavy top quark [3].

However, it has become clear that the SM cannot be the ultimate model due to its inherent flaws. Consequently, the physics community is focusing on theories and models that offer solutions to these problems. One of the more often-seen ideas is that of supersymmetry (SUSY). Apart from being motivated by a symmetry principle, it also solves various flaws of the SM, including dark matter and the hierarchy problem. Additionally, it allows for an embedding into a grand-unification theory. The hierarchy problem is often attributed to be the main motivation for SUSY research, as it is one of the few proposals for solving this issue. In contrast, dark matter and grand unification proposals are more abundant. However, having a model that addresses all of those issues of the SM while allowing grand-unification is surely enough to spark academic interest around the world.

Supersymmetry itself is more of a concept or a framework to work in. It could be summarised as the idea that each fermion has a superpartner with bosonic characteristics and vice versa. The motivation for the idea lies within the fact that such a *symmetry*, non-trivially expands the known symmetries of space-time: Poincaré transformations [4]. Physicists conceptualized different models to 'work' with SUSY, each presenting a different mechanism of how supersymmetry manifests. The main differences are on how supersymmetry is spontaneously broken at lower energies. This breaking is necessary because experiments have clearly ruled out the possibility of superpartners having the same mass as their partner.

This thesis will focus on the Minimal Supersymmetric Standard Model (MSSM) [5]. This choice is based on the two fundamental ingredients of the MSSM: minimal particle content and the soft SUSY breaking mechanism. The first adheres to the guiding principle of Occam's Razor: the simplest or smallest model that works should have the preference. The second ingredient acknowledges the current limit of knowledge regarding the breaking mechanism: we do not know how the symmetry is broken. So, why not just add all SUSY-breaking terms that do not cancel wanted SUSY characteristics?¹ This presents us with the ability to 'choose' the correct breaking mechanism as soon as signs of SUSY are observed in the future.

Problematic for MSSM research is, contrary to what the name suggests, its enormous possible parameter space. The model contains 105 additional real-valued parameters relative to the SM,² ranging from the mass parameters of the superpartners to trilinear coupling strengths. This enormous parameter space makes it impractical to significantly rule out parameter regions, hindering effects to constrain the MSSM and to

¹To be more exact we only add extra terms that contain couplings with positive mass dimension. More details will be given in chapter 3.

²Of course, some parameters might be complex variables, however these are counted as two real-valued parameters.

identify focus points for future experiments.

Therefore, a variant of the MSSM has been introduced: the pMSSM [6]. Through knowledge-based and experimentally motivated requirements, the parameter space is reduced to 19 parameters. The motivation for these requirements lies in minimisation of flavour violation, experimentally verified-to-be-rare decays and meson mixing effects. Another motivation is the explicit omission of any CP violation in addition to what the SM has to offer. However, it is the removal of this last assumption that lies at the heart of this thesis. Previous research has studied the pMSSM quite well. However, to study the effect of SUSY on CP violating observables one needs to take consider the existence of CP violation within the model. Furthermore, introducing more CP violation might be necessary to solve, for example, the matter-antimatter asymmetry in the universe [7]. This model carries the name cpMSSM. The cpMSSM is essentially the same as the pMSSM, only with the addition of CP violation. In practice, the addition of CP violation results in 6 independent phases added to the pMSSM. This partially brings back the problematic side of the MSSM parameter space. Especially when considering the complex relationship between the phases themselves and the pMSSM parameter point. This relationship needs to be either understood, or calculation software needs to be used to determine if a point is interesting and/or viable.

To conduct research on the workings of the cpMSSM, a substantial number of not experimentally excluded parameter combinations are required. Currently, at the HEP department of the Radboud University, these combinations are produced using Gaussian Particle Filters [8]. This method samples new parameter configurations (referred to as points) from a n-dimensional Gaussian distribution. However, this filter heavily relies on finetuning by the user since every Gaussian distribution has two configurable parameters (mean and variance) per dimension. Also, in order to make points, one already needs correct points to center the Gaussian distribution on. This introduces a potential bias into the sampled points, as it becomes harder to explore unknown regions effectively.

This thesis aims to explore a potential solution for this challenge within the world of Machine Learning (ML). In other words, the goal is to use ML to efficiently and effectively ‘transform’ a pMSSM point into large numbers of cpMSSM points. This eliminates the need for a ‘handcrafted’ Gaussian Particle Filter. Additionally, there is an expectation that an ML model will generate more diverse samples within the cpMSSM parameter space.

After training such a model and, ideally, enabling it to generate a substantial number of non-excluded cpMSSM points, this thesis will seek to demonstrate its usefulness beyond adhering to the CP violating eEDM limit.³ Therefore, we explore one of the main advantages of SUSY: its potential dark matter candidate. One of the observables related the dark matter candidate is that of the dark matter relic density⁴. Astronomical observations confirm the existence of exotic, yet-to-be-understood, matter must exist that does not interact electromagnetically. Commonly this matter is referred to as dark matter [9]. SUSY models can feature a viable dark matter candidate, particularly when the lightest supersymmetric particle (LSP) is a superpartner of the neutral SM bosons and R-parity⁵ is assumed. The quantity of dark matter remaining in the universe is termed the dark matter relic density, and this should align with current experimental observations. Currently, no extensive research has been done on what the effect of CP violation is on the relic density within SUSY, although the existence of an effect has been shown before [10]. Such effects are anticipated since couplings that determine the annihilation of the LSP, are (indirectly) affected by CP violating phases [10]. However, existing research has predominantly concentrated on very specific points with very specific values for the added phase(s), as they were limited in the amount and diversity of cpMSSM points they could create. By introducing a new ML-based sampler we hope to significantly contribute to a better understanding of CP-violating effects on the dark matter relic density and other CP-violating effects within supersymmetry.

³electron Electric Dipole Moment, see 4.1.

⁴From here on the dark matter relic density will just be called the relic density. No other form of relic density is of interest within this thesis. Therefore, as is often done, we abbreviate to relic density only.

⁵For an explanation: see the end of section 3.3.2.

Chapter 2

Used Conventions

This chapter will present the conventions and notations used within this thesis. Given the subject of supersymmetry this is especially important, as there are many conventions possible.

First a small list of the more basic notations:

- We use all ‘normal’ conventions with regards to indices: Greek indices are used for four-vectors, etc.
- Repeated indices are summed over.
- We have $\hbar = c = \epsilon_0 = k_B = 1$ for the natural units.
- We define the electron charge as $q_e = Q_e e = -1e$.
- g' , g and g_3 represent the couplings of U(1), SU(2) and SU(3) respectively.
- σ^μ or $\bar{\sigma}^\mu$ represent the Pauli matrices: where $\sigma^\mu = (I_2, \vec{\sigma})$ and $\bar{\sigma}^\mu = (I_2, -\vec{\sigma})$, and $\vec{\sigma} = (\sigma_1, \sigma_2, \sigma_3)$.
- $\sigma^{\mu\nu} \equiv \frac{i}{4}(\sigma^\mu \bar{\sigma}^\nu - \sigma^\nu \bar{\sigma}^\mu)$ and $\bar{\sigma}^{\mu\nu} \equiv \frac{i}{4}(\bar{\sigma}^\mu \sigma^\nu - \bar{\sigma}^\nu \sigma^\mu)$.

Further we use the mostly-plus spacetime metric:

$$\eta_{\mu\nu} = \text{diag}(-1, +1, +1, +1), \quad (2.1)$$

in contrast to many other QFT-related works. However, this choice is made because its consequences are mostly reflected within the basis of the supersymmetry theory. For this basis [11] is used as a guide, and thus the same convention is used. If results or other expressions are presented using the mostly-minus metric, this is mentioned if important for the result. Most prominently this results in $p^2 = -m^2$ for on-shell particles and the generator of spacetime translations, \mathcal{P}_μ , being $-i\partial_\mu$ instead of $i\partial_\mu$.

The basics of SUSY are given using 2-dimensional Weyl spinors. The specific representation used of the 4×4 gamma matrices, in 2×2 blocks, is:

$$\gamma^\mu = \begin{pmatrix} 0 & \sigma^\mu \\ \bar{\sigma}^\mu & 0 \end{pmatrix}, \quad \gamma_5 = \begin{pmatrix} -I_2 & 0 \\ 0 & I_2 \end{pmatrix}. \quad (2.2)$$

Within this representation a four component Dirac spinor can be written as follows:

$$\Psi_D = \begin{pmatrix} \xi_\alpha \\ \chi^{\dagger\dot{\alpha}} \end{pmatrix}, \quad \bar{\Psi}_D = (\chi^\alpha \ \xi_{\dot{\alpha}}^\dagger) \quad (2.3)$$

Here ξ and χ represent Weyl spinors (respectively a left and right-handed version), and we directly see the convention to index the ‘lower’ spinor representation using dotted indices. To work within the space of Weyl spinors we also need a definition of an inner product:

$$\xi\chi \equiv \xi^\alpha \chi_\alpha = \epsilon_{\alpha\beta} \xi^\alpha \chi^\beta. \quad (2.4)$$

Here $\epsilon_{\alpha\beta}$ is an antisymmetric symbol defined as follows:

$$\epsilon^{12} = -\epsilon^{21} = \epsilon_{21} = -\epsilon_{12} = 1, \quad \epsilon_{11} = \epsilon_{22} = \epsilon^{11} = \epsilon^{22} = 0. \quad (2.5)$$

For some intuition we briefly look at how this translates to the Standard Model. Dirac spinors are used to represent the fermions within the Standard Model. We then get for the electron:

$$\begin{pmatrix} e \\ \bar{e}^\dagger \end{pmatrix} \equiv \begin{pmatrix} e_L \\ e_R \end{pmatrix}, \quad (2.6)$$

where the e_L can be found within a chiral doublet together with ν_{e_L} and we can find e_R as a chiral singlet, the right handed electron. Thus, compared to the general example we have: $\xi = e = e_L$ and $\chi = \bar{e} = e_R^\dagger$, where we have suppressed spinor indices.

Lastly, it is nice to state the nomenclature used for particles within supersymmetry. Each SM particle has their corresponding superpartner (called sparticle). This extends to fermions, having sfermions as scalar superpartner, which holds for all subcategories of fermions. On the other hand we denote the superpartner of bosons by appending -ino. Thus gauge bosons have gauginos as spin-1/2 superpartner and the Higgs bosons have higgsino superpartners.

2.1 Used Abbreviations

This section presents a list of all commonly used abbreviations in this thesis

BSM	Beyond the Standard Model
C	Charge conjugation
cpMSSM	pMSSM with explicit CP violation
CPV	CP Violation
DM	Dark Matter
eEDM	electron Electric Dipole Moment
GPF	Gaussian Particle Filter
HEP	High Energy Physics
LEP	Large Electron Positron collider
LHC	Large Hadron Collider
LR	Likelihood Ratio
LSP	Lightest Supersymmetric Particle
ML	Machine Learning
MLP	Multi Layer Perceptron
MSSM	Minimal Supersymmetric Standard Model
P	Parity
pMSSM	phenomenological Minimal Supersymmetric Standard Model
QFT	Quantum Field Theory
RQS	Rational Quadratic Spline
SM	Standard Model
SUSY	Supersymmetry
T	Time reversal

Chapter 3

Theory

3.1 Standard Model

Before we delve into the world of supersymmetry (SUSY) we first need a small, and very brief, look into the Standard Model (SM).

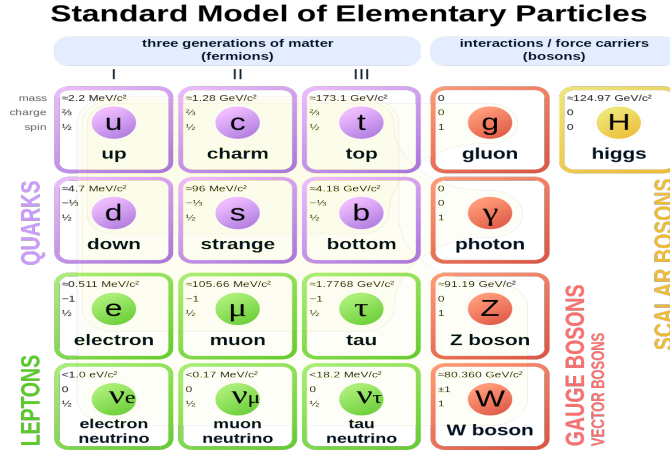


Figure 3.1: The elementary particles of the Standard Model. This includes the fermions, subdivided into leptons and quarks, and the Higgs boson and gauge bosons [12].

Figure 3.1 shows all bosons and fermions within the SM. Fermions consist of two groups: quarks and leptons. Quarks come in three generations, each generation having an up and down variant under the electroweak force. Leptons also come in those same three generations, but instead of an up and down variant they come in a chargeless neutrino and charged, electron-like variants. The weak force is one of three fundamental forces described by the SM.¹ These forces are carried by four different types of gauge bosons. In the SM these are a result of demanding *local* gauge invariances (gauge symmetries) under the gauge group:

$$SU(3)_C \times SU(2)_L \times U(1)_Y.$$

Within the SM Lagrangian invoking these gauge invariances locally also leads to interactions between those gauge bosons and fermions. These interactions thus represent the force at the level of elementary particles. The particle that is involved with the introduction of this interaction, the gauge boson, can therefore be seen as its carrier. More specifically, the $SU(3)_C$ gauge group gives rise to the strong force and its corresponding

¹The fourth force, gravity, can currently not be understood within a QFT framework, which is the framework of the SM. The description of general relativity in a QFT framework is therefore a separate field of study.

eight massless gluons. The combination $SU(2)_L \times U(1)_Y$ gives rise to the electroweak interactions, a combination of the electromagnetic and weak force. The involved gauge bosons are the W^\pm and Z for the weak interaction and the γ , denoting the photon, for the electromagnetic force. A small note should be made that the coupling strength belonging to $U(1)_Y$, the hypercharge, is not equal to the coupling strength belonging to $U(1)_Q$, the electromagnetic charge. This difference is an (essential) part of electroweak symmetry breaking.

We have one boson left to explain: the Higgs Boson. The Higgs boson is introduced via the Higgs mechanism, which also gives the W^\pm and Z their mass. This concept is called electroweak symmetry breaking and boils down to introducing a new complex scalar doublet of Higgs fields: the Higgs doublet, and a corresponding Higgs potential involving this doublet. The main characteristic of the doublet is that it has a specific, non-zero vacuum expectation value in the ground state ('vacuum state') of the SM theory. The principal idea is that due to the $SU(2)_L \times U(1)_Y$ gauge symmetry we have degenerate states in the SM ground state for the newly-introduced Higgs doublet. By setting a vacuum expectation value (vev) for the doublet we 'choose' one of those states as the actual ground state of the doublet. The idea is to make this choice in a specific manner: in the ground state we still need invariance under $U(1)_Q$. Therefore, we only set a vev for the electromagnetically, neutral scalar field of the doublet. As a result, the $SU(2)_L \times U(1)_Y$ symmetry 'spontaneously' breaks into a $U(1)_Q$ symmetry in the SM ground state. Consequently, the W^\pm and Z acquire mass terms related to the non-zero vev. In contrast by only setting a vev for the neutral field, the photon remains massless.

The above mechanism is introduced into the SM to remain consistent with the experimentally measured masses of the W^\pm and Z gauge bosons. However, due to this mechanism, we also introduce a new boson with non-zero mass: the Higgs boson. This boson, and its mass, was experimentally verified in 2012 [2].

The W^\pm and Z masses, together with the Higgs mass, fermions masses, and their respective interaction strengths are the free parameters of the SM. Aside from the interaction between the Higgs boson and the lightest fermions and the four-point coupling strengths associated with the Higgs mechanism, all of these have at this point been experimentally confirmed and measured. This verification shows the success of the SM and its predictions. For a more detailed look into both the Standard Model and its QFT framework, as well as electroweak symmetry breaking we refer to the extensive work of [13].

3.1.1 Discrete Symmetries

One of the more abundant topics within this thesis will be that of CP violation. CP violation is a form of violating a discrete symmetry, in this case violating the combined action of charge conjugation (C) and parity (P). A system is symmetric under 'C' if it is invariant under charge conjugation, which interchanges particles and antiparticles. It is symmetric under 'P' if it is invariant under a parity transformation, i.e spatial inversion: $\vec{x} \rightarrow -\vec{x}$, where \vec{x} is the three-dimensional spatial vector. The third important discrete symmetry of nature is T: Time-reversal. Naturally, a system is symmetric under 'T' if it is invariant under the reversal of time. A system, or interaction, that breaks one of these symmetries is then, for example, called C violating. The SM, as all physical laws and models, has something called CPT symmetry. This means that under the simultaneous action of C, P and T the system remains invariant.

In the SM (and SUSY) CP violation is introduced by non-absorbable phases. The best example of this is the CKM matrix of the SM. This matrix introduces mixing between up and down-like quarks. Thus the complex-valued 3×3 matrix is always sandwiched between two three-dimensional vectors. Therefore by assigning phases to these vectors we can always absorb 5 of the 9 possible phases in the CKM matrix. By other characteristics of the matrix, like unitarity, 3 other phases can be rotated away, leaving 1 phase that in no way can be absorbed. If such a phase becomes non-zero, CP violation is introduced within the theory.

3.2 Supersymmetry

This section will introduce the basics of supersymmetry using the method of supersymmetric Lagrangians, while also shortly showcasing the arguments for using superfields. Although the former will be slightly more

in-depth, it will not be fully detailed and not all calculations will be present. For more details and/or calculations the reader is referred to [11, 4].

3.2.1 Supersymmetric Lagrangians

The idea of supersymmetry is easiest to explain when looking at a small ‘toy model’ containing only the minimal content: a left-handed two-component (Weyl) fermion, denoted by ψ , and its superpartner, a complex scalar field ϕ . Within such a model it is possible to define the simplest working transformation that represents supersymmetry.

We can start with the simplest form of a Lagrangian containing these two fields and only kinetic terms. Such a model, including supersymmetry, is called a non-interacting *Wess-Zumino Model* [14]:

$$\mathcal{L} = \mathcal{L}_{\text{scalar}} + \mathcal{L}_{\text{fermion}}, \quad (3.1)$$

$$\mathcal{L}_{\text{scalar}} = -\partial^\mu \phi^* \partial_\mu \phi, \quad \mathcal{L}_{\text{fermion}} = i\psi^\dagger \bar{\sigma}^\mu \partial_\mu \psi. \quad (3.2)$$

Now we introduce supersymmetry and thus need to define a transformation of the scalar field into the fermion field and vice versa, in other words:

$$\delta\phi \propto \psi, \quad \delta\psi \propto \phi. \quad (3.3)$$

As we want this transformation to correspond to a symmetry, namely supersymmetry, two requirements can be used to determine the actual expression for the transformation.

1. The action of the theory needs to be invariant under the transformation.
2. The algebra of supersymmetry needs to be closed.

We first set the transformation of the scalar field to be of the simplest form possible.

$$\delta\phi = \epsilon\psi, \quad \delta\phi^* = \epsilon^\dagger\psi^\dagger. \quad (3.4)$$

Here the ϵ^α represents a generic, infinitesimal, two-component, fermionic (Weyl) object. In essence, it represents/parameterizes the supersymmetry transformation, while also making sure that the transformation is consistent at the level of spinorial indices. Given the mass dimension of $\frac{3}{2}$ for the fermionic field and 1 for the scalar field, ϵ needs to have a mass dimension of $-\frac{1}{2}$. We then need the aforementioned two requirements to set the second transformation. The first requirement is mathematically formulated as follows:

$$\delta\mathcal{S} = \int d^4x (\delta\mathcal{L}_{\text{scalar}} + \delta\mathcal{L}_{\text{fermion}}) = 0 \quad (3.5)$$

This means that the Lagrangian itself can only transform up to a total derivative.² By calculating $\delta\mathcal{L}_{\text{scalar}}$ and demanding that $\delta\mathcal{L}_{\text{fermion}}$ cancels all terms up to a total derivative, the following candidate SUSY transformation for fermions can be found:

$$\delta\psi_\alpha = -i(\sigma^\mu \epsilon^\dagger)_\alpha \partial_\mu \phi, \quad \delta\psi^\dagger_{\dot{\alpha}} = i(\epsilon\sigma^\mu)_{\dot{\alpha}} \partial_\mu \phi^* \quad (3.6)$$

Now we need to check the second requirement: does this transformation result in a closed algebra? To check this we apply the commutator of two transformations with two different ϵ ’s to the two fields (fermion and scalar). In that case, we find a derivative of the field the commutator was applied to. In other words, we find a space-time translation, which is one of the main symmetries of any QFT theory. We could therefore conclude the algebra of the symmetry to be closed under the Poincaré group, were there not a small catch. When applying the commutator to the fermionic field, ψ , extra terms are present if ψ is off-shell, i.e. when its equations of motion are not valid. These terms are problematic, as we want to use supersymmetry within a QFT framework, in which particles can be off-shell as well.

²Or, in other words, only a term representing a 4-divergence can be added to the Lagrangian.

This can be solved by using a trick: introducing a new complex, scalar field F , without any kinetic terms and thus with trivial equations of motion: an auxiliary field³. This idea is quite logical, as we are introducing a symmetry between a scalar field with two degrees of freedom and a fermionic field that, when off-shell, has four degrees of freedom. If the fermion is on-shell, two of those degrees of freedom become dependent on the other via the equations of motion, and thus only then the symmetry 'works'. However, in the off-shell case we need the extra two degrees of freedom of the fermion to be present in its partner, scalar field as well. These off-shell degrees of freedom are now present in the degrees of freedom of the F field, which, by design, disappear when they are not needed (i.e. in the on-shell case).

All in all, this results in a new part for the Lagrangian.

$$\mathcal{L}_{aux} = F^* F, \quad (3.7)$$

which also directly shows the mass dimension of 2 of the F field. The trick now consists of adding this field F to the transformation rule of ψ , while also defining a suitably chosen transformation for F . The new transformation for ψ becomes:

$$\delta\psi_\alpha = -i(\sigma^\mu \epsilon^\dagger)_\alpha \partial_\mu \phi + \epsilon_\alpha F, \quad \delta\psi_\alpha^\dagger = i(\epsilon \sigma^\mu)_{\dot{\alpha}} \partial_\mu \phi^* + \epsilon_{\dot{\alpha}}^\dagger F^* \quad (3.8)$$

The next step is to determine the transformation of the new field F . This transformation is specified by the fact that we need the algebra to be closed at all times. Thus, the transformation of F needs to cancel the equation of motion terms that remain when applying the commutator of transformations to ψ , as mentioned earlier. This leads to:

$$\delta F = -i\epsilon^\dagger \bar{\sigma}^\mu \partial_\mu \psi, \quad \delta F^* = i\partial_\mu \psi^\dagger \bar{\sigma}^\mu \epsilon, \quad (3.9)$$

and due to this transformation we find:

$$[\delta_{\epsilon_1}, \delta_{\epsilon_2}] \mathbf{X} = i(-\epsilon_1 \sigma^\mu \epsilon_2^\dagger + \epsilon_2 \sigma^\mu \epsilon_1^\dagger) \partial_\mu \mathbf{X}, \quad (3.10)$$

where \mathbf{X} denotes any of the involved fields: $\phi, \phi^*, \psi, \psi^\dagger, F, F^*$. As mentioned, we see the term $-i\partial_\mu$, which corresponds with the generator of space-time translations.

This last point can be written in a slightly more convenient way. For this one needs to use Noethers theorem: any continuous symmetry⁴ of the Lagrangian results in a conserved current. Through this current, it is possible to construct the conserved charges, which are the generators of the supersymmetry transformations. These generators are denoted by \mathcal{Q}_α and $\mathcal{Q}_\alpha^\dagger$. After this procedure⁵ the algebra of supersymmetry can be neatly written down:

$$\{\mathcal{Q}_\alpha, \mathcal{Q}_\alpha^\dagger\} = -2\sigma_{\alpha\dot{\alpha}}^\mu \mathcal{P}_\mu \quad (3.11)$$

$$\{\mathcal{Q}_\alpha, \mathcal{Q}_\beta\} = \{\mathcal{Q}_\alpha^\dagger, \mathcal{Q}_\beta^\dagger\} = 0. \quad (3.12)$$

Here \mathcal{P}_μ is the generator of space-time translations, the same transformations of which we saw signs within equation 3.10. Furthermore, we note that the new generators are fermionic generators,⁶ which was to be expected as we need fermions to transform to scalars and vice versa. This is also the reason for anti-commutators instead of commutators.

We can now make quite an interesting remark, although mostly unimportant to this thesis. Within the above algebra we notice the link of SUSY with spacetime translations. To some this raises the question: what if, like gauge symmetries, we make SUSY a locally valid transformation? In other words, the ϵ that parameterizes the SUSY transformations becomes dependent on spacetime. At that point we would introduce a new boson, in analogy with other gauge bosons. But now that boson would be one that interacts

³To be more exact: the equations of motion for this field are: $F = F^* = 0$

⁴As noted before, we speak of a symmetry if the Lagrangian is invariant under the transformation up to a total derivative. Officially only the action needs to be truly symmetric.

⁵Again: for these, and other steps omitted within this thesis, see [11]

⁶This can be noticed by the fact that the generators have a spinorial index.

with spacetime. Could such a boson then be regarded/used as a carrier of gravity? In other words, would that introduce general relativity on the scale of quantum mechanics? This is an actual idea looked into for a quantum theory of gravity. The interested reader is referred to [15] for more details.

3.2.2 Other Supersymmetric Arguments

The previous section introduced the theory of supersymmetry through the idea of introducing a supersymmetric Lagrangian, or more specifically a supersymmetric transformation. However, there is another motivation to introduce supersymmetry, one that is even a little more fundamental as it more motivates the *idea*.

The SM is a model that has inherent symmetries. Since it contains the symmetries that any QFT model in flat spacetime needs to respect: the symmetries under Lorentz transformations and translations. These symmetries are grouped within the Poincaré group. The Poincaré group is the largest set of (non-trivial) spacetime symmetries that are currently found within nature. It is then interesting to try to extend this symmetry as far as nature allows. Be it out of curiosity or in an attempt to resolve flaws of the SM.

In some way, this is already being done, through gauge symmetries. Only these symmetries can not be seen as a ‘true extension’, as all generators of gauge groups commute with the generators of the Poincaré group:

$$[T^a, T^b] = if^{abc}T^c \quad (3.13)$$

$$[T^a, \mathcal{P}^\mu] = [T^a, M^{\rho\sigma}] = 0. \quad (3.14)$$

Here T denotes a generic generator of a generic $SU(N)$ gauge group. In other words, gauge symmetries extend the Poincaré group *trivially*, and the resulting ‘extended’ symmetry group is just a direct product of both initial groups. It has been shown, through the *Coleman-Mandula no-go theorem* [16], that there does not exist any symmetry with bosonic generators that can extend the Poincaré group in a non-trivial way.

It is exactly within this theorem that lies the motivation for supersymmetry. The theorem refers to bosonic generators. Bosonic generators are generators that change a bosonic (fermionic) state into another bosonic (fermionic) state. Therefore, instead of bosonic operators we introduce the only other option: fermionic operators. Fermionic generators change the amount of spin by $\frac{1}{2}$. Thus we introduce the core idea of supersymmetry, in more mathematical terms:

$$\mathcal{Q}_\alpha |\text{Boson}\rangle = |\text{Fermion}\rangle_\alpha, \quad \mathcal{Q}_\alpha |\text{Fermion}\rangle^\alpha = |\text{Boson}\rangle. \quad (3.15)$$

It turns out that this does extend the Poincaré group in a non-trivial and closed way:

$$[\mathcal{Q}_\alpha, \mathcal{P}^\mu] = 0 \quad (3.16)$$

$$\{\mathcal{Q}_\alpha, \mathcal{Q}_\alpha^\dagger\} = -2\sigma_{\alpha\dot{\alpha}}^\mu \mathcal{P}_\mu \quad (3.17)$$

$$[M^{\rho\sigma}, \mathcal{Q}_\alpha] = -(\sigma^{\rho\sigma})_\alpha^\beta \mathcal{Q}_\beta \quad (3.18)$$

$$\{\mathcal{Q}_\alpha, \mathcal{Q}_\beta\} = \{\mathcal{Q}_\alpha^\dagger, \mathcal{Q}_\beta^\dagger\} = 0. \quad (3.19)$$

The attentive reader might have seen the similarities with equation 3.11, thus showing supersymmetry to be a very good and interesting extension of the current spacetime symmetries within the SM.

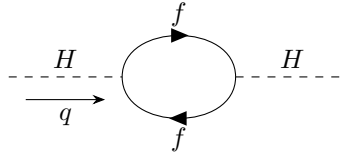
To work upwards from the above-mentioned, generic, symmetry towards a working supersymmetric model, a lot of technicalities are required. One of these is the usage of two new coordinates, just as a fourth was needed within space-time and Lorentz transformations. Out of this idea superfields emerged. Superfields are fields that contain multiple, smaller component fields. These component fields then represent the particles, with both the particle and its corresponding sparticle being present within one superfield. Thus, superfields could be seen as ‘overlapping’ fields that represent the symmetry per SM particle. The background theory for this endeavour can be found in [4].

3.2.3 Hierarchy Problem

Within chapter 1, it is mentioned that one of the advantages of supersymmetry is its natural solution to the hierarchy problem. This section will both explain the hierarchy problem, as well as present (the idea of) the solution that supersymmetry provides for this problem.

The hierarchy problem has to do with the experimentally found Higgs mass of 125 GeV. First of all, it is a perfectly possible value for the Higgs mass according to the SM. The problem more lies with the fact that it is much lower than ‘naturally’ expected. As we know, the SM is most likely a ‘low energy’ theory, that in one way or another originates from a higher energy theory. Therefore, in some way, the SM is expected to couple to (new) particles at this high energy scale. Most of the particles are stable against the effects this could introduce. The scalar Higgs boson as described within the SM, however, would not be. Thus we, kind of, would expect the mass of the Higgs boson to be closer to the high energy scale.

To quantify this, we can look at the 1-loop corrections to the Higgs mass using a fermion residing at that higher scale:



For this diagram we need the following Feynman rule:

$$= -i\lambda_f. \quad (3.20)$$

If we calculate these corrections we find:⁷

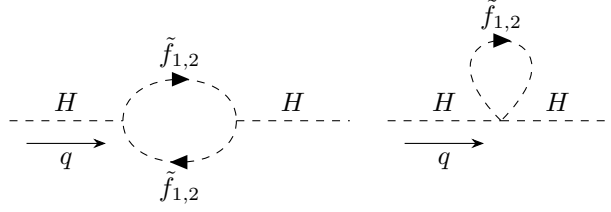
$$\delta m_H^2 = \frac{-2\lambda_f^2}{(2\pi)^4} \left(2 \int \frac{d^4 l}{l^2 - m_f^2} + \int \frac{d^4 l (4m_f^2 - q^2)}{(l - m_f^2)((l + q)^2 - m_f^2)} \right) \Big|_{q^2=m_H^2}, \quad (3.21)$$

where $\lambda_f = m_f/v$ is the dimensionless Yukawa coupling between the Higgs boson and the heavy fermions. Furthermore, we have m_f as the mass of the fermion, which is assumed to be at the scale of new physics. By counting the powers of the integral we see that the first integral therefore is quadratically divergent, and the second logarithmically divergent. In other words, the first term seems to suggest a much higher correction than the observed Higgs mass itself. So either we have very high fine-tuning⁸ or we need a new mechanism that cancels that first integral.

That is where SUSY comes in. SUSY introduces two new interactions that contribute to the 1-loop corrections of the Higgs mass:

⁷Note that these calculations use the mostly-minus metric.

⁸And let it be known that physicists really hate this word, both people who use it as an argument against theories, as well as people who use it against those people. For more on this, see the thesis of Marrit Schutten [17]



In these diagrams the fermion has been replaced by two sfermions: one for the left-handed fermion field and one for the right-handed field. The two scalar fields have the exact same, high, mass as the original fermion.

To calculate the above diagrams we need the associated Feynman rules:

$$\begin{aligned}
 & \text{Vertex 1: } H \text{ (dashed line) connects to } f_i \text{ and } \bar{f}_i \text{ (solid lines with arrows). Value: } = -2i\lambda_s v, \\
 & \text{Vertex 2: } H \text{ (dashed line) connects to } \tilde{f}_i \text{ and } \tilde{f}_i \text{ (dashed lines with arrows). Value: } = -2i\lambda_s.
 \end{aligned} \tag{3.22}$$

A small, but important, remark regarding these rules needs to be made. We see that the first rule contains a triple scalar coupling of mass dimension one. The second rule, on the other hand, contains a dimensionless quartic scalar coupling.

Now we first look at the expression resulting from the second interaction that is introduced by SUSY. The contribution of that interaction is:

$$\frac{4\lambda_s}{(2\pi)^4} \int \frac{d^4 l}{l^2 - m_{\tilde{f}}^2}, \tag{3.23}$$

here $m_{\tilde{f}}$ is the mass of both the left and right-handed sfermion, which we naturally assume to be equal. As mentioned, within exact SUSY, this mass of the sfermion equals the mass of the fermion. Due to these masses being the same this term perfectly cancels with the quadratically divergent term of 3.21 if $\lambda_s = \lambda_f^2$. This relation holds true due to the way we introduce fermion/sfermion interactions, more on this will be given in 3.3.2. Further, the relative minus sign emerged because of the difference in loop contents: a fermion loop gets a relative minus sign with respect to a bosonic loop according to the Feynman rules.

However, even if the mass of the fermion and sfermion are not exactly equal⁹ we find the following difference term:

$$\int d^4 l \left(\frac{1}{l^2 - m_{\tilde{f}}^2} - \frac{1}{l^2 - m_f^2} \right) = (m_{\tilde{f}}^2 - m_f^2) \int d^4 l \frac{1}{(l - m_{\tilde{f}}^2)(l - m_f^2)}, \tag{3.24}$$

which is still only logarithmically divergent.

Thus the only thing left to check is that the first diagram does not re-introduce quadratic divergences. For this diagram we find:

$$8\lambda_s^2 v^2 \int \frac{d^4 l}{(2\pi)^4} \frac{1}{(l - m_{\tilde{f}}^2)((l + q)^2 - m_{\tilde{f}}^2)} \Big|_{q^2 = m_H^2}, \tag{3.25}$$

which is only logarithmically divergent. Therefore SUSY proposes a working solution to the Hierarchy problem, due to the SUSY couplings for fermions and sfermions being related. Again, how we introduce these related couplings is explained in 3.3.2.

⁹In other words, we are in a broken SUSY theory, which actually are more prominent than unbroken theories.

3.3 Minimal Supersymmetric Standard Model (MSSM)

In this section, we introduce the most well-known SUSY model: the MSSM. The Minimal Supersymmetric Standard Model is defined by the fact that it contains the minimal needed number of particles for a working supersymmetric version of the SM.

3.3.1 Particle Content

This section presents the particles present within the MSSM.

Table 3.1: The gauge eigenstates of the MSSM, showing the ‘conventional’ SM state, its spin and the corresponding SUSY state and its spin.

Particles	Spin	Notation	Sparticles	Spin	Notation
B, W - Bosons	1	B^0, W^\pm, W^0	Bino, Wino	$\frac{1}{2}$	$\tilde{B}^0, \tilde{W}^\pm, \tilde{W}^0$
Higgs	0	$H_u^0, H_d^0, H_u^+, H_d^-$	Higgsino	$\frac{1}{2}$	$\tilde{H}_u^0, \tilde{H}_d^0, \tilde{H}_u^+, \tilde{H}_d^-$
Gluon	1	g	Gluino	$\frac{1}{2}$	\tilde{g}
L/R up-type quarks	$\frac{1}{2}$	u_L/u_R^\dagger	L/R up-type squarks	0	$\tilde{u}_L/\tilde{u}_R^*$
L/R down-type quarks	$\frac{1}{2}$	d_L/d_R^\dagger	L/R down-type squarks	0	$\tilde{d}_L/\tilde{d}_R^*$
L/R charged leptons	$\frac{1}{2}$	e_L/e_R^\dagger	L/R charged sleptons	0	$\tilde{e}_L/\tilde{e}_R^*$
neutrinos	$\frac{1}{2}$	ν_L	sneutrinos	0	$\tilde{\nu}_L$

There are two important things to note from table 3.1. Firstly, we note that there are no new ‘conventional’ particles. All particles on the left-hand side of the table, disregarding the Higgs sector, are also part of the SM. For example, no fourth-generation quark has been introduced. In addition, in analogy with the SM, no right-handed neutrinos are added.¹⁰ However, there is one exception: the MSSM contains two Higgs doublets. Why this is necessary will be explained in section 3.3.2.

A point of notation: within this thesis as well as in [11] the notation of superfields (see section 3.2.2) is used from time to time. The notation itself is presented in table 3.2 for chiral supermultiplets. These superfield symbols represent both the conventional particle as well as the sparticle within a chiral supermultiplet. To get some intuition: \tilde{u} here truly denotes a ‘supermultiplet’: $\tilde{u} \propto (u_R^\dagger, \tilde{u}_R^*)$, whereas Q denotes a doublet

Table 3.2: The notation of superfields and the chiral supermultiplet they represent for the superfield symbols used within this thesis. This means that the vector superfields representing the gauge bosons and their gauginos are not listed, as their superfield notation is not used within this thesis.

Superfield	Particles	Sparticles
Q	(u_L, d_L)	$(\tilde{u}_L, \tilde{d}_L)$
\tilde{u}	u_R^\dagger	\tilde{u}_R^*
\tilde{d}	d_R^\dagger	\tilde{d}_R^*
L	(ν_L, e_L)	$(\tilde{\nu}_L, \tilde{e}_L)$
\tilde{e}	e_R^\dagger	\tilde{e}_R^*
H_u	(H_u^+, H_u^0)	$(\tilde{H}_u^+, \tilde{H}_u^0)$
H_d	(H_d^0, H_d^-)	$(\tilde{H}_d^0, \tilde{H}_d^-)$

of supermultiplets: $Q \propto \begin{pmatrix} (u_L, \tilde{u}_L) \\ (d_L, \tilde{d}_L) \end{pmatrix}$. Although this notation is not conventional, it does provide some

¹⁰The idea of right-handed neutrinos is becoming more conventional. However, the MSSM does not incorporate them, following the path of minimal particle content.

intuition. Further, the convention for \bar{u}, \bar{d} and \bar{e} reflects the SUSY way to handle the right-handed (singlet) fields that feature in the SM. This way involves using conjugation to turn a right-handed Weyl spinor into a left-handed variant and treating the scalar superpartner accordingly. At this point it is also good to note that these superfields behave similarly to Weyl spinors in an inner product:

$$Q \cdot H_u = \epsilon_{ab} Q^a H_u^b. \quad (3.26)$$

Here $a, b = 1, 2$ and the \cdot is explicitly used to showcase that the inner product is of two superfields and therefore follows 3.26 and not the conventional four-vector inner product.

3.3.2 Introducing Interactions

Now we know the particle content of the MSSM we can start to have a more insightful look at interactions within a SUSY model. The Wess-Zumino model of section 3.2.1 did not contain any interaction terms. The introduction of non-gauge interactions within a SUSY model will be performed in general terms, thus also following the notation of section 3.2.1.

We start by writing down all possible interaction terms that can be contained within a renormalizable theory. In other words, the included terms must have a mass dimension from the fields and derivatives that does not exceed four. We get the following interaction Lagrangian:

$$\mathcal{L}_{\text{int}} = \left(-\frac{1}{2} W^{ij} \psi_i \psi_j + W^i F_i + x^{ij} F_i F_j\right) + c.c. - U, \quad (3.27)$$

here i/j are summed over for repeated indices, and i/j run over the different fields that correspond with a particle and its linked sparticle from table 3.1. Further, W^{ij}, W^i, x^{ij} and U are polynomials of the (complex) scalar fields with degrees 1, 2, 0 and 4 respectively.

The first important thing to note is that all terms within $\delta\mathcal{L}_{\text{free}}$ sum to zero by themselves. Therefore \mathcal{L}_{int} needs to be invariant under SUSY on its own as well. This has as a first consequence that both U and x^{ij} are zero, since the corresponding terms that arise within $\delta\mathcal{L}_{\text{int}}$ after a SUSY transformation contain specific combinations of spinors and scalar fields that cannot be compensated by the other terms within equation 3.27 [11]. Thus we are left with the following, general, interaction Lagrangian:

$$\mathcal{L}_{\text{int}} = \left(-\frac{1}{2} W^{ij} \psi_i \psi_j + W^i F_i\right) + c.c.. \quad (3.28)$$

Now it is good to note that W^{ij} and W^i currently are not related, but will later turn out to be and therefore follow a very similar notation.

It is now easiest to separate $\delta\mathcal{L}_{\text{int}}$ into several parts, which must all cancel separately. The first part is the part that contains 4 spinors in each term.¹¹

$$\delta\mathcal{L}_{\text{int}}|_{4 \text{ spinors}} = \left(-\frac{1}{2} \frac{\delta W^{ij}}{\delta \phi_k} (\epsilon \psi_k) (\psi_i \psi_j) - \frac{1}{2} \frac{\delta W^{ij}}{\delta \phi_k^*} (\epsilon^\dagger \psi_k^\dagger) (\psi_i \psi_j)\right) + c.c.. \quad (3.29)$$

By imposing that this expression needs to be zero we get two characteristics of W^{ij}

1. $\frac{\delta W^{ij}}{\delta \phi_k}$ is totally symmetric under the interchange of i, j and k .
2. W^{ij} is holomorphic in the complex field ϕ .

The first characteristic follows from the first term in 3.29. This term can become zero through the Fierz identity.¹² Therefore the first term cancels if and only if $\frac{\delta W^{ij}}{\delta \phi_k}$ is symmetric under any interchange of the its superscripts.

¹¹For the ones that are counting along: ϵ is, of course, also a spinor.

¹²To be a little more detailed, we have: $(\epsilon \psi_i)(\psi_j \psi_k) + (\epsilon \psi_j)(\psi_k \psi_i) + (\epsilon \psi_k)(\psi_i \psi_j) = 0$.

For the second term, there is no other way to become zero than for $\frac{\delta W^{ij}}{\delta \phi_k^*}$ to be zero. We can not use the fierz identity due to $\epsilon^\dagger \psi^\dagger$ being conjugated and $\psi_i \psi_j$ not. In other words, W^{ij} is not allowed to contain terms with ϕ_k^* . This is the same as saying that W^{ij} is holomorphic in the complex field ϕ . It is, however, essential to note that this does not constrain our choice for which field is this complex conjugated field, it is merely a relative choice.¹³ There only needs to be a consistent choice, either we use ϕ or ϕ^* for a specific particle within W , but not both. This property in itself is a reason for the existence of another Higgs doublet within SUSY. As will be explained later.

The found properties of W^{ij} give us the possibility to write:

$$W^{ij} = \frac{\delta^2}{\delta \phi_i \delta \phi_j} W = \frac{\delta^2}{\delta \phi_i \delta \phi_j} \left(\frac{1}{2} M^{kl} \phi_k \phi_l + \frac{1}{6} y^{klm} \phi_k \phi_l \phi_m \right). \quad (3.30)$$

Here we introduced the object W , which is called the *superpotential*: a scalar potential that is a holomorphic function of the complex variable ϕ_k .¹⁴ We note that according to the above ‘definition’ it is possible to add a linear term to the superpotential. Such a term would require the existence of a full gauge invariant chiral supermultiplet within the theory. Given the minimal particle content of the MSSM (see table 3.1) this is not the case. Thus the term is omitted from the superpotential.

The focus then shifts to the rest of $\delta \mathcal{L}_{\text{int}}$. All other terms are terms containing 2 spinors or, equivalently, a space-time derivative. For brevity, the corresponding terms are not written here, but can be found in [11]. This part of the Lagrangian becomes a total derivative if:

$$W^i = \frac{\delta W}{\delta \phi_i} = \frac{\delta}{\delta \phi_i} \left(\frac{1}{2} M^{kl} \phi_k \phi_l + \frac{1}{6} y^{klm} \phi_k \phi_l \phi_m \right), \quad (3.31)$$

thus motivating that all non-gauge interactions are determined by one scalar, holomorphic potential: the superpotential.

The last step is to eliminate the auxiliary field F . Due to the introduction of the second term in equation 3.28 its equation of motion has become:

$$F_i = -W_i^* \quad F^{i*} = -W^i \quad (3.32)$$

This leads to the following Lagrangian, containing both the ‘free’ and the interaction part:

$$\mathcal{L} = -\partial^\mu \phi^{*i} \partial_\mu \phi_i + i \psi^{\dagger i} \bar{\sigma}^\mu \partial_\mu \psi_i - \frac{1}{2} (W^{ij} \psi_i \psi_j + W_{ij}^* \psi^{\dagger i} \psi^{\dagger j}) - W^i W_i^* \quad (3.33)$$

$$\begin{aligned} &= -\partial^\mu \phi^{*i} \partial_\mu \phi_i + i \psi^{\dagger i} \bar{\sigma}^\mu \partial_\mu \psi_i - V(\phi, \phi^*) \\ &\quad - \frac{1}{2} M^{ij} \psi_i \psi_j - \frac{1}{2} M_{ij}^* \psi^{\dagger i} \psi^{\dagger j} - \frac{1}{2} y^{ijk} \phi_i \psi_j \psi_k - \frac{1}{2} y_{ijk}^* \phi^* i \psi^{\dagger j} \psi^{\dagger k}. \end{aligned} \quad (3.34)$$

Here in the second step we wrote out the superpotential in general terms (equation 3.30) and introduced the scalar potential. The scalar potential is:

$$V(\phi, \phi^*) = W^i W_i^* = \quad (3.35)$$

$$M_{ij}^* M^{ik} \phi^{*j} \phi_k + \frac{1}{2} M^{nk} y_{jin}^* \phi_k \phi^{*j} \phi^{*i} + \frac{1}{2} M_{nk}^* y^{jin} \phi^{*k} \phi_j \phi_i + \frac{1}{4} y^{kjm} y_{ilm}^* \phi_k \phi_j \phi^{*i} \phi^{*l}. \quad (3.36)$$

With these equations one can look at, and compare, the Klein-Gordon equation for the fermions and the scalars:

$$\partial^\mu \partial_\mu \phi_i = M_{ki}^* M^{kj} \phi_j + \dots \quad (3.37)$$

$$\partial^\mu \partial_\mu \psi_i = M_{ki}^* M^{kj} \psi_j + \dots \quad \partial^\mu \partial_\mu \psi^{\dagger i} = \psi^{\dagger j} M_{kj}^* M^{ki} + \dots \quad (3.38)$$

¹³Because $(\phi^*)^* = \phi$.

¹⁴As we will see within the MSSM, the actual object should be only scalars. However it introduces all interactions, also SM interactions. Therefore it is often denoted using superfields as that directly shows these interactions as well, instead of first needing derivatives.

Thus the fermions and the scalars have the exact same squared mass matrix:

$$(M^2)_i^j = M_{ki}^* M^{kj} \quad (3.39)$$

After diagonalization through a unitary matrix, and combining our ϕ and ψ into a chiral supermultiplet we arrive at a similar conclusion as for superfields, with all multiplets containing a mass-degenerate complex scalar and a Weyl spinor.

This section does not contain the introduction to gauge interactions, as this description is deemed slightly outside the scope of this theory block. However, a full description can be found in [11] and [15]. In appendix A.1 all diagrams of both the gauge interactions as well as the non-gauge interactions can be found.

Now the only thing left to do is to specify the superpotential in the case of the MSSM.¹⁵

$$W_{\text{MSSM}} = \bar{u} \mathbf{y}_u Q \cdot H_u - \bar{d} \mathbf{y}_d Q \cdot H_d - \bar{e} \mathbf{y}_e L \cdot H_d + \mu H_u \cdot H_d. \quad (3.40)$$

Before we go into the consequences of this potential, we need to resolve a possible misunderstanding that could emerge at this point. Equation 3.40 uses a superfield notation, which is given in table 3.2. As a consequence, the above terms also include non-scalar, and SM terms. Within the definition of the superpotential especially the former are not present. However, after following the full procedure in section 3.3.2 to get to \mathcal{L}_{int} we would, of course, also get interactions involving fermions and a scalar Higgs boson. Therefore, they are already included here, skipping the full procedure. Further through this notation the superpotential is responsible for *all* non-gauge interactions within the MSSM, not just the SUSY interactions. Lastly, the superfield notation is the less cluttered option.

Beyond notation, the main point this potential postulates is that within the MSSM there is a need for two Higgs doublets. This has to do with the fact that W needs to be holomorphic. For example, for the second term $\bar{d} \mathbf{y}_d Q \cdot H_u^C$, with $H_u^C = i\sigma_2 H_u^*$, is an option, but the first term already contains a non-conjugated H_u . Similarly, $\bar{u} \mathbf{y}_u Q \cdot H_d^C$, with $H_d^C = i\sigma_2 H_d^*$, is not an option for the first, as H_d is already included in the first term. Therefore the first three terms, often called Yukawa terms, need two different doublets to have terms that have a zero net charge, as is required for $U(1)_Q$ gauge invariance.¹⁶ For completeness' sake, the last term, called the μ term, is the supersymmetric version of the Higgs boson mass term in the SM.

Secondly, we note that there could have been more terms within this potential, without using new superfields:

$$W_{\Delta L=1} = \frac{1}{2} \lambda^{ijk} L_i \cdot L_j \bar{e}_k + \lambda'^{ijk} L_i \cdot Q_j \bar{d}_k + \mu' L_i \cdot H_u \quad (3.41)$$

$$W_{\Delta B=1} = \frac{1}{2} \lambda''^{ijk} \bar{u}_i \bar{d}_j \bar{d}_k. \quad (3.42)$$

However, as seen from the notation, these terms either break lepton or baryon number conservation. Experiments¹⁷ tell us that these should be conserved, as is accidentally the case in the SM. To make sure this is also the case within the MSSM, we explicitly require the conservation of R-parity:

$$R = (-1)^{2s+3B+L}. \quad (3.43)$$

Here B is the baryon number, L is the lepton number and s is the spin of the (s)particle. This definition ensures that all conventional SM particles and all Higgs bosons have $R = 1$, and all superpartners have $R = -1$. R-parity conservation has very important consequences. It ensures that all interactions involve an even number of SUSY particles, therefore the lightest supersymmetric particle (LSP) cannot decay, which will be important in 4.2. If the LSP also has no charge and colour, it becomes a dark matter candidate.

¹⁵It is possible to also write down this superpotential in the corresponding scalar fields as well. However, then we would need to go through the procedure of derivatives to see the SM interactions as well.

¹⁶To see that using H_u in place of H_d and vice versa leads to non-zero net charge terms within the Lagrangian, one needs to write out the multiplets included in equation 3.40 using the inner product rule of 3.26.

¹⁷Such as proton-decay experiments.

3.3.3 Breaking Mechanism

As mentioned in the previous section, particles and their corresponding sparticles have the same mass under supersymmetry. However, it is clear from experiments they cannot have the same mass. Otherwise, we would already have observed sparticles. Therefore, we need a mechanism that breaks supersymmetry spontaneously, like in the case of electroweak symmetry breaking through the Higgs mechanism. We need the Lagrangian to be invariant under supersymmetry, but to not respect this in the ground state by specifically selecting one from a set of degenerate ground states. Furthermore, it is good to note that breaking SUSY always will result in also breaking the electroweak symmetry and vice versa. We will get back to this in the discussion of the Higgs sector in 3.3.4.

A lot of breaking mechanisms have been proposed. All of them with their reasoning for where and how the breaking is introduced. The MSSM takes a different approach. Instead of claiming one idea and therefore using only some of the possible terms, all possible mass-breaking terms are used and parameterized. The idea is that if SUSY is observed or discovered one can then try to determine the correct parameters for the MSSM at that point in time.

There is, however, one main point of consideration for all terms that can be included. The terms are not allowed to re-introduce the hierarchy problem (3.2.3). In other words, if the term re-introduces a quadratic divergence within the mass corrections of the Higgs boson, the term is not allowed. In practice this results in the mass dimension of the coupling of the added term having to be positive. We can see this by looking back at section 3.2.3. In that section we see that the four-point SUSY vertex (that has a dimensionless coupling) resolves the problem perfectly. However, this does require that no new four-point interactions are introduced, because these new interactions would reintroduce a quadratic divergence that is no longer cancelled anywhere. On the other hand, we see that three-point interactions only introduce logarithmic divergences. Therefore, adding the corresponding terms with a positive mass dimension coupling does not re-introduce the problem. Also, as explained in section 3.2.3, introducing a mass difference between fermions and sfermions does not spoil the cancellation of quadratic divergences (see equation 3.24). So terms with a positive mass dimension coupling are also acceptable in that regard. All terms that adhere to this condition, while still spontaneously breaking supersymmetry, are called soft-breaking terms.

After careful consideration [15, 11, 18] this leads to the following terms to be added to the Lagrangian:

$$\begin{aligned}\mathcal{L}_{\text{soft}}^{\text{MSSM}} = & -\frac{1}{2}(M_3\tilde{g} \cdot \tilde{g} + M_2\tilde{W} \cdot \tilde{W} + M_1\tilde{B} \cdot \tilde{B} + c.c.) \\ & -(\tilde{u}\mathbf{A}_u\tilde{Q} \cdot H_u^S - \tilde{d}\mathbf{A}_d\tilde{Q} \cdot H_d^S - \tilde{e}\mathbf{A}_e\tilde{L} \cdot H_d^S + c.c.) \\ & -\tilde{Q}^\dagger \mathbf{m}_Q^2 \tilde{Q} - \tilde{L}^\dagger \mathbf{m}_L^2 \tilde{L} - \tilde{u}m_u^2\tilde{u}^\dagger - \tilde{d}m_d^2\tilde{d}^\dagger - \tilde{e}m_e^2\tilde{e}^\dagger \\ & -m_{H_u}^2|H_u^S|^2 - m_{H_d}^2|H_d^S|^2 - (bH_u^S \cdot H_d^S + c.c.).\end{aligned}\tag{3.44}$$

A slightly different than usual notation is used within this equation. The first three lines do seem to contain superfields, but the tilde refers to only the sparticle part of those superfields. In addition, the superscript S above the Higgs doublets explicitly notes that these terms only refer to the scalar fields and not the fermionic superpartner. To be a little more explicit, the second line is written out in terms of sparticles and Higgs particles:

$$\begin{aligned}& +\tilde{u}_R^*\mathbf{A}_u\tilde{u}_L H_u^0 - \tilde{u}_R^*\mathbf{A}_u\tilde{d}_L H_u^+ - \tilde{d}_R^*\mathbf{A}_d\tilde{u}_L H_d^- \\ & +\tilde{d}_R^*\mathbf{A}_d\tilde{d}_L H_d^0 - \tilde{e}_R^*\mathbf{A}_e\tilde{\nu}_e H_d^- + \tilde{e}_R^*\mathbf{A}_e\tilde{e}_L H_d^0 + c.c.. \end{aligned}\tag{3.45}$$

If we look back at equation 3.44 we see that the first line represents the mass terms for the gauginos. The second line contains trilinear (scalar)³ terms. These resemble the scalar sparticles part of the Yukawa terms within the superpotential 3.40. As such it is sometimes the case that the trilinear couplings: \mathbf{A}_u , \mathbf{A}_d and \mathbf{A}_e are written as proportional to those Yukawa couplings. In equation 3.44 this has *not* been done. The third line contains 3×3 mass terms for the squarks and sleptons. Note that tildes are required on the subscripts of the squared mass matrices, but these are omitted for readability. The last line contains the supersymmetry

breaking terms of the Higgs, which involves the Higgs doublets only. These terms will contribute to the MSSM Higgs potential additional to $\mu H_u \cdot H_d$ generated terms present in the (unbroken) superpotential. An important remark that stems from how $\mathcal{L}_{\text{soft}}^{\text{MSSM}}$ is determined is the following expectation:

$$M_1, M_2, M_3, \mathbf{A}_u, \mathbf{A}_d, \mathbf{A}_e \sim m_{\text{soft}}, \quad (3.46)$$

$$\mathbf{m}_Q^2, \mathbf{m}_L^2, \mathbf{m}_{\bar{u}}^2, \mathbf{m}_{\bar{d}}^2, \mathbf{m}_{\bar{e}}^2, m_{H_u}^2, m_{H_d}^2, b \sim m_{\text{soft}}^2, \quad (3.47)$$

where m_{soft} is a characteristic scale expected to not be (much) larger than 10^3 GeV [11]. This expectation kind of proposes a hierarchy of parameters within the MSSM soft-breaking mechanism.

The main downside of the soft-breaking mechanism is the introduction of an enormous number of parameters. After rotating away all dependent parameters we are left with 105 additional parameters relative to the SM. This leaves a small blemish on the MSSM, as the sheer amount of parameters is phenomenologically challenging.

We now have discussed all parts of the MSSM. For some overview, it is good to explicitly see which parts are contained within the full Lagrangian of the MSSM.

$$\mathcal{L}_{\text{MSSM}} = \mathcal{L}_{\text{free}}^{\text{MSSM}} + \mathcal{L}_{\text{chiral}}^{\text{MSSM}} + \mathcal{L}_{\text{gauge}}^{\text{MSSM}} + \mathcal{L}_{\text{soft}}^{\text{MSSM}}, \quad (3.48)$$

here $\mathcal{L}_{\text{free}}^{\text{MSSM}}$ is the Lagrangian as explained in section 3.2, generalized over all fields as mentioned in section 3.3.1. $\mathcal{L}_{\text{chiral}}^{\text{MSSM}}$ is the interaction Lagrangian for the chiral supermultiplets using the superpotential as discussed in section 3.3.2. $\mathcal{L}_{\text{gauge}}^{\text{MSSM}}$ contains the gauge interactions in the MSSM. This part is not discussed in this thesis but is explored in [11]. The last part, $\mathcal{L}_{\text{soft}}^{\text{MSSM}}$ denotes the soft breaking terms introduced in the MSSM, as described in this section.

3.3.4 Particle Sectors

At this point, we have discussed the important building blocks of the MSSM: particle content, interactions and the mechanism to separate the masses of sparticles and particles. Now we can have a look into some sectors of the MSSM in more detail, where the focus will be on those sectors that will play an important role for the research in this thesis.

Higgs Sector

The first sector we will have a look at is that of the two Higgs doublets and the electroweak symmetry-breaking mechanism of the MSSM. Within the MSSM the Higgs doublets are defined as follows:

$$H_u = e^{i\eta} \begin{pmatrix} H_u^+ \\ H_u^0 \end{pmatrix} \quad H_d = \begin{pmatrix} H_d^0 \\ H_d^- \end{pmatrix}. \quad (3.49)$$

This definition pulls out a relative phase between the doublets: η . As a consequence, the vacuum expectation values, which will be introduced later, are allowed to both be real. Given that we now have two doublets this leads to a different potential, compared to the potential of the symmetry breaking mechanism of the SM [15].

$$\begin{aligned} V(H_u, H_d) = & (|\mu^2| + m_{H_u}^2)(|H_u^0|^2 + |H_u^+|^2) + (|\mu^2| + m_{H_d}^2)(|H_d^0|^2 + |H_d^-|^2) \\ & + (be^{i\eta}(H_u^+ H_d^- - H_u^0 H_d^0) + c.c.) \\ & + \frac{1}{8}(g^2 + g'^2)(|H_u^0|^2 + |H_u^+|^2 - |H_d^0|^2 - |H_d^-|^2)^2 \\ & + \frac{1}{2}g^2 |H_u^+ H_d^{0*} + H_u^0 H_d^{-*}|^2. \end{aligned} \quad (3.50)$$

The next step is to note that, like the SM breaking mechanism, we have the opportunity to use a $SU(2)_L$ gauge rotation. This freedom is used to demand $\langle H_u^+ \rangle = 0$. In other words, its vacuum expectation value is

zero. The linked minimisation requirement of $\frac{\partial V(H_u, H_d)}{\partial H_u^+} = 0$ means that we also get $\langle H_d^- \rangle = 0$. Ultimately, this leads to a simplified potential:

$$V(H_u, H_d) = (|\mu|^2 + m_{H_u}^2)|H_u^0|^2 + (|\mu|^2 + m_{H_d}^2)|H_d^0|^2 - (be^{i\eta}H_u^0H_d^0 + c.c.) + \frac{1}{8}(g^2 + g'^2)(|H_u^0|^2 - |H_d^0|^2)^2. \quad (3.51)$$

Just as in the SM, by setting vacuum expectation values (vevs) for the left-over, neutral, scalar fields we introduce spontaneous electroweak symmetry breaking. In contrast to the SM, we now have two values to set, therefore we need some labelling and notation:¹⁸

$$\langle H_u^0 \rangle = v_u/\sqrt{2}, \quad \langle H_d^0 \rangle = v_d/\sqrt{2}, \quad \tan \beta = \frac{v_u}{v_d}. \quad (3.52)$$

A nice remark to make here is the fact that the electroweak symmetry breaking laid out at this point is intrinsically connected with the breaking of supersymmetry itself. For the electroweak symmetry breaking to work, we need the potential (equation 3.51) to be bounded from below and its minimum to be stable, away from the origin. Due to these two requirements it is no longer possible to have both $m_{H_u}^2$ and $m_{H_d}^2$ being zero [17]. As these parameters are SUSY breaking parameters introduced in section 3.3.3, we explicitly introduce SUSY breaking through electroweak symmetry breaking.

The SM vev (v) is related to the masses of the electroweak bosons: M_Z and M_W . As we want the MSSM to be an extension of the SM, and thus keep the same observed masses for these bosons, we require the following relation between the vev's:

$$v^2 = v_u^2 + v_d^2 = \frac{4m_Z^2}{g^2 + g'^2}, \quad (3.53)$$

where the last equation only holds at tree level.¹⁹ With all of the above definitions and relations we can expand the Higgs doublets around the vevs:

$$e^{i\eta} \begin{pmatrix} H_u^+ \\ H_u^0 \end{pmatrix} = \frac{e^{i\eta}}{\sqrt{2}} \begin{pmatrix} 0 \\ v_u + \phi_u + i\sigma_u \end{pmatrix}, \quad \begin{pmatrix} H_d^0 \\ H_d^- \end{pmatrix} = \frac{1}{\sqrt{2}} \begin{pmatrix} v_d + \phi_d + i\sigma_d \\ 0 \end{pmatrix} \quad (3.54)$$

Subsequently, we then minimize the potential, in such a way that $v_{u,d}$ stay the corresponding vacuum expectation value:²⁰

$$0 = \frac{\partial V(H_u, H_d)}{\partial \phi_{u,d}}|_{\sigma_{u,d}=\phi_{u,d}=0}, \quad 0 = \frac{\partial V(H_u, H_d)}{\partial \sigma_{u,d}}|_{\sigma_{u,d}=\phi_{u,d}=0}. \quad (3.55)$$

This leads to four equations, of which three are independent:

$$\begin{aligned} |\mu|^2 + m_{H_u}^2 - |b| \cot \beta \cos(\phi_b + \eta) - \frac{1}{2}m_Z^2 \cos 2\beta + \frac{1}{v_u} \frac{\partial V(H_u, H_d)_{\text{corr}}}{\partial \phi_u} &= 0 \\ |\mu|^2 + m_{H_d}^2 - |b| \tan \beta \cos(\phi_b + \eta) + \frac{1}{2}m_Z^2 \cos 2\beta + \frac{1}{v_d} \frac{\partial V(H_u, H_d)_{\text{corr}}}{\partial \phi_d} &= 0 \\ \sin(\phi_b + \eta)|b| + \frac{1}{v_d} \frac{\partial V(H_u, H_d)_{\text{corr}}}{\partial \phi_u} &= \sin(\phi_b + \eta)|b| + \frac{1}{v_u} \frac{\partial V(H_u, H_d)_{\text{corr}}}{\partial \phi_d} = 0, \end{aligned} \quad (3.56)$$

where $b = |b|e^{i\phi_b}$. The above equations are what are called the *tadpole equations*. Any valid MSSM model has to satisfy these equations. As a result, we are left with three fewer free parameters within all those possible parameter configurations for the MSSM. To make sure that the used parameter configurations follow these equations, phenomenological calculation software takes N - 3 parameters as input and calculates the other 3. The problem is that not all software has made the same choice of 'independent parameters', resulting in convention problems [17]. Possible choices for the free parameters are given in section 3.4.1.

¹⁸Again, given the explicit phase within equation 3.49 these are real-valued numbers.

¹⁹Equations given are conventionally at tree-level, if not specified otherwise.

²⁰The mixing of ϕ and σ seen here is due to the introduction of $e^{i\eta}$.

Due to the two doublets we have eight fields associated with the Higgs mechanism. Three of those are absorbed by the longitudinal polarisation of the W and Z bosons through Goldstone bosons. The other five contribute to five mass eigenstates: the charged scalars H^+ and H^- and three neutral ones. Our interest lies with the three neutral bosons.

To discuss the three neutral bosons, we first look at the case in which no extra CP violation is allowed in SUSY.²¹ In this case, we have two Higgs bosons (denoted by the h^0 and H^0 mass eigenstates) that are CP even, and one CP-odd, pseudo-scalar boson (denoted by the A^0 mass eigenstate). If there is no added CP violation, these do not mix, and we find the following relation between gauge eigenstates and mass eigenstates [17, 15]:

$$\begin{pmatrix} H_u^0 \\ H_d^0 \end{pmatrix} = \frac{1}{\sqrt{2}} \begin{pmatrix} v_u \\ v_d \end{pmatrix} + \frac{1}{\sqrt{2}} R_\alpha \begin{pmatrix} h^0 \\ H^0 \end{pmatrix} + \frac{i}{\sqrt{2}} R_{\beta_0} \begin{pmatrix} G^0 \\ A^0 \end{pmatrix}. \quad (3.57)$$

Here G^0 is one of the Goldstone bosons that has been introduced. The rotation matrices are defined as follows:

$$R_\alpha = \begin{pmatrix} \cos \alpha & \sin \alpha \\ -\sin \alpha & \cos \alpha \end{pmatrix}, \quad R_{\beta_0} = \begin{pmatrix} \sin \beta_0 & \cos \beta_0 \\ -\cos \beta_0 & \sin \beta_0 \end{pmatrix}, \quad (3.58)$$

where in practice β_0 coincides with β as introduced in equation 3.52.

However, if extra CP violation is introduced the three neutral states start to mix. In that case, we need to make a constraining remark on the possibilities. CP violation would introduce rare decays from the lightest neutral Higgs boson to W and Z bosons [19]. These decays are experimentally limited [20], resulting in a limit on the mixing of the pseudo-scalar component (A^0) and the SM-like Higgs (h^0) of about 10%.

In the case that extra CP violation relative to the SM is allowed we define the gauge eigenstates slightly differently:

$$\phi^0 = (\sqrt{2}(\Re\{H_d^0 - \frac{v_d}{\sqrt{2}}\}, \Re\{H_u^0 - \frac{v_u}{\sqrt{2}}\}, \Im(H_d^0), \Im(H_u^0))^T). \quad (3.59)$$

This definition does still include the neutral Goldstone boson. As in the case without extra CP violation, we have to define a mixing matrix. This mixing matrix defines the physical mass eigenstates in terms of ϕ^0 , in other words [21]:

$$-\phi^{0T} \mathcal{M}_{\phi^0}^2 \phi^0 = -\phi^{0T} S^T S^* \mathcal{M}_{\phi^0}^2 S^\dagger S \phi^0, \quad (3.60)$$

where the mass eigenstates in this case will be mass ordered: (H_1, H_2, H_3) . This mixing matrix S should be defined in such a way that the neutral Goldstone boson is explicitly projected out as that Goldstone boson should not be represented within the mass eigenstates but within the longitudinal polarization of the electroweak bosons. There are multiple conventions [17], one of which is written out below:

$$\begin{pmatrix} H_1 \\ H_2 \\ H_3 \end{pmatrix} = S \phi^0 = \begin{pmatrix} \mathcal{O}_{3 \times 3} & 0 \\ 0 & 0 \end{pmatrix} \begin{pmatrix} \sqrt{2}(\Re\{H_d^0 - \frac{v_d}{\sqrt{2}}\}) \\ \sqrt{2}(\Re\{H_u^0 - \frac{v_u}{\sqrt{2}}\}) \\ A^0 \\ G^0 \end{pmatrix} = \begin{pmatrix} \mathcal{O}_{3 \times 3} & 0 \\ 0 & 0 \end{pmatrix} \begin{pmatrix} 1 & 0 & 0 & 0 \\ 0 & 1 & 0 & 0 \\ 0 & 0 & \sin \beta & \cos \beta \\ 0 & 0 & -\cos \beta & \sin \beta \end{pmatrix} \phi^0. \quad (3.61)$$

Within this convention, $\mathcal{O}_{3 \times 3}$ defines the decomposition of the physical mass eigenstates in an intermediate basis of states. This intermediate basis of states is shown in the explicitly given column vector in 3.61. We recognize the second rotation matrix of equation 3.58 in the lower right corner of the explicit 4×4 matrix in the last step of 3.61, as it mixes the same states as the imaginary part of 3.57. Since the third and fourth components of ϕ^0 are defined as the imaginary part of H_d^0 and H_u^0 we do not see explicit imaginary contributions in 3.61. There is no explicit form of $\mathcal{O}_{3 \times 3}$ given because it is computed through loop corrections, as there is no extra CP violation present (within the Higgs potential) at tree level.

There are two last remarks. It can be estimated [22] that the mass of the lightest, neutral Higgs boson is bounded by

$$m_{h^0} \lesssim 135 \text{ GeV}. \quad (3.62)$$

²¹Relative to the CP violation present within the SM.

This bound is very important as it is the only currently falsifiable prediction of the MSSM, which has been found consistent with experiment. Therefore keeping the MSSM alive as a viable theory beyond the SM.

Furthermore, given its closeness to the observed SM Higgs-boson mass, the lightest Higgs boson within the MSSM is often called the SM-like Higgs. If we compare its properties with that of the SM Higgs, they also act similar unless the two CP-even Higgs bosons are particularly close in mass. However, that scenario is mostly ruled out by experiments [20]. The opposite scenario, where the two CP-even Higgs bosons are very far apart in mass, is also possible and not yet ruled out by experimental data. In this scenario, the SM-like Higgs decouples from the other bosons. As a result, the couplings and vertices of the SM Higgs bosons all coincide with the couplings of the h^0 boson. All new physics then becomes related to the H^0 boson. This decoupling limit is found when α (of equation 3.57) goes towards the limit of $\beta - \pi/2$. For more details the reader is referred to [17, 15].

Neutralino Sector

The next sector to have a look at is that of the neutral electroweak gauginos, the superpartners of the neutral gauge bosons of the SM. Beforehand it is important to note that all expressions in the next two sections are at tree level. Beyond tree level, masses become sensitive to loop corrections. This makes general expressions very difficult as these corrections are dependent on the chosen particle spectrum as well. Therefore, in practice, non-tree level terms are always calculated using software.

It is possible to combine the neutral electroweak gauginos and the neutral higgsinos into mass eigenstates. The combination of these four mass eigenstates is called *neutralinos*. In the gauge eigenstates, $\psi^0 = (\tilde{B}, \tilde{W}^0, \tilde{H}_d^0, \tilde{H}_u^0)$, the mass term is given as follows:²²

$$\mathcal{L} = -\frac{1}{2}(\psi^0)^T \mathbf{M}_{\tilde{\chi}^0} \psi^0 + c.c., \quad (3.63)$$

where the mass matrix is²³

$$\mathbf{M}_{\tilde{\chi}^0} = \begin{pmatrix} M_1 & 0 & -g'v_d/\sqrt{2} & g'v_u/\sqrt{2} \\ 0 & M_2 & gv_d/\sqrt{2} & -gv_u/\sqrt{2} \\ -g'v_d/\sqrt{2} & gv_d/\sqrt{2} & 0 & -\mu \\ g'v_u/\sqrt{2} & -gv_u/\sqrt{2} & -\mu & 0 \end{pmatrix}. \quad (3.64)$$

In this matrix M_1 , M_2 are the parameters introduced in $\mathcal{L}_{\text{MSSM}}^{\text{SOFT}}$ and μ is introduced in the superpotential. The other off-diagonal terms arise due to the result of couplings between Higgs bosons and other gauginos, where the Higgs fields are replaced by their respective vevs. Note that these last terms can also be written in terms of β , defined via $\tan \beta = \frac{v_u}{v_d}$, and Weinberg angles [11].

To obtain the mass eigenstates that we would call neutralinos, we diagonalize the matrix in equation 3.64 via a unitary matrix \mathbf{N} :

$$\tilde{\chi}_i^0 = \mathbf{N}_{ij} \psi_j^0. \quad (3.65)$$

such that:

$$\mathbf{N}^* \mathbf{M}_{\tilde{\chi}^0} \mathbf{N}^{-1} = \begin{pmatrix} m_{\tilde{\chi}_1^0} & 0 & 0 & 0 \\ 0 & m_{\tilde{\chi}_2^0} & 0 & 0 \\ 0 & 0 & m_{\tilde{\chi}_3^0} & 0 \\ 0 & 0 & 0 & m_{\tilde{\chi}_4^0} \end{pmatrix}. \quad (3.66)$$

Due to the symmetry of the complex mass matrix, there is only the need for one unitary matrix for diagonalization. Normally we would need two, to both diagonalize $\mathbf{M}\mathbf{M}^\dagger$ and $\mathbf{M}^\dagger\mathbf{M}$.

²²Small note: If we were to be working in a 4-component (Dirac) notation there would be a h.c. instead of c.c.. In that case we would first find the 2-spinor component of a Majorana field with the hermitian conjugate term providing the other 2-spinor component for the full Dirac spinor.

²³We omit the relative Higgs doublet phase $e^{i\eta}$ within the lowest row and right-most column whenever v_u is also present. This choice is made for clarity and the fact that within the research of this thesis we choose $\eta = 0$ through phase rotations.

On the diagonal of 3.66 we then find the mass terms of the neutralinos, which are the absolute values of the eigenvalues of 3.64. The convention is to use a mass hierarchy for the neutralinos. Therefore we have: $m_{\tilde{\chi}_1^0} < m_{\tilde{\chi}_2^0} < m_{\tilde{\chi}_3^0} < m_{\tilde{\chi}_4^0}$. It is possible to determine these masses in closed form, in terms of $M_1, M_2, \mu, \tan\beta, g, g'$ and the Higgs vevs. However, these expressions are not that illuminating as they are very complicated. In the literature, it is not uncommon to choose \mathbf{N} as real and orthogonal when there is no extra CP violation. But note that this does allow for negative mass terms for the neutralinos. These can be rotated away using chiral rotations, thus negative mass terms do not equal negative physical masses [17]. In this thesis this convention is adopted, as it is also adopted within the calculation software used.

If the lightest of the neutralinos is the lightest of all sparticles it is a very good dark matter candidate. It would be stable since it can only decay into SM particles, which violates R-parity, while also having no electromagnetic charge and strong-force colour. Naturally, if the lightest neutralino is the LSP, research into its composition and the important couplings that can be derived from that becomes very relevant. Its composition is determined by the first row of \mathbf{N} , where the amount of bino, wino and higgsino mixing of the lightest neutralino is given by $|\mathbf{N}_{11}|, |\mathbf{N}_{12}|$ and $\sqrt{|\mathbf{N}_{13}|^2 + |\mathbf{N}_{14}|^2}$ respectively. In general, if $|\mu| \gg |M_{1,2}|$ we expect the LSP to be dominated by the gauginos, thus being wino or bino-like. If the situation is reversed, the LSP is more higgsino-like. Note that this requires these parameters to be much larger than M_Z while still having a clear hierarchy among themselves, as otherwise the other off-diagonal terms within 3.64 introduce more mixing.

Chargino Sector

We now have discussed the neutral sector. Naturally, the next point of attention is then given to the charged electroweak gauginos and the charged higgsinos. These are called *charginos* and can be denoted by $\tilde{\chi}_i^\pm$ within their mass eigenstates. Again, these are mass ordered, thus $\tilde{\chi}_1^\pm$ is the lightest chargino.

If we use $\psi^\pm = (\tilde{W}^+, \tilde{H}_u^+, \tilde{W}^-, \tilde{H}_d^-)$ we get the following mass term for the charginos:²⁴

$$\mathcal{L} = -\frac{1}{2}(\psi^\pm)^T \mathbf{M}_{\tilde{C}} \psi^\pm + c.c.. \quad (3.67)$$

Here the mentioned mass matrix can be written in 2×2 block form as:

$$\mathbf{M}_{\tilde{C}} = \begin{pmatrix} 0 & \mathbf{M}_{\tilde{\chi}^\pm}^T \\ \mathbf{M}_{\tilde{\chi}^\pm} & 0 \end{pmatrix}, \quad (3.68)$$

where the 2×2 mass matrix of charginos reads:²⁵

$$\mathbf{M}_{\tilde{\chi}^\pm} = \begin{pmatrix} M_2 & \frac{gv_u}{\sqrt{2}} \\ \frac{gv_d}{\sqrt{2}} & \mu \end{pmatrix}. \quad (3.69)$$

The next step is, of course, analogous to the neutralino sector: introduce a way to diagonalize this matrix towards mass terms for the individual charginos. However, in this case we need two unitary matrices to do so: \mathbf{U} and \mathbf{V} , due to the mass matrix not being symmetric. In this case, we design the unitary matrices such that:

$$\mathbf{U}^* \mathbf{M}_{\tilde{\chi}^\pm} \mathbf{V}^{-1} = \begin{pmatrix} m_{\tilde{\chi}_1^\pm} & 0 \\ 0 & m_{\tilde{\chi}_2^\pm} \end{pmatrix}. \quad (3.70)$$

This in turn means that we can define the relation between gauge eigenstates and physical mass eigenstates as:

$$\begin{pmatrix} \tilde{\chi}_1^+ \\ \tilde{\chi}_2^+ \end{pmatrix} = \mathbf{V} \begin{pmatrix} \tilde{W}^+ \\ \tilde{H}_u^+ \end{pmatrix}, \quad \begin{pmatrix} \tilde{\chi}_1^- \\ \tilde{\chi}_2^- \end{pmatrix} = \mathbf{U} \begin{pmatrix} \tilde{W}^- \\ \tilde{H}_d^- \end{pmatrix}. \quad (3.71)$$

²⁴The same note as for neutralinos regarding 4-component vs 2-component notation and h.c. instead of c.c. can be made here. However in this case we do not work with a Majorana field due to the charges present.

²⁵Just as in 3.64 we have omitted the phase factor $e^{i\eta}$ in the v_u term as we will fix $\eta = 0$ through phase rotations.

We get four eigenvalues of the 4×4 matrix of 3.68, but due to its block form and the usage of two unitary matrices these four values are doubly degenerate. Thus, the lightest negatively charged chargino has the same mass term as the positively charged one.

It is now possible to again have a look at the possible compositions of the charginos, where a chargino can be wino-like or higgsino-like. For a good overview of the possible compositions of the charginos and neutralinos table 3.3 is presented.

Table 3.3: The dominant contribution within the composition of the neutralinos and charginos. Note that for the charginos the \pm sign is omitted for clarity. Furthermore, we assume all three parameters: μ , M_1 and M_2 to be much larger than M_Z while still having a clear hierarchy among themselves, as otherwise more complicated mixing is present. [17]

Parameter Hierarchy	Chargino Composition $\tilde{\chi}_1^\pm, \tilde{\chi}_2^\pm$	Neutralino Composition $\tilde{\chi}_1^0, \tilde{\chi}_2^0, \tilde{\chi}_3^0, \tilde{\chi}_4^0$
$ M_1 < M_2 < \mu $	\tilde{W}, \tilde{H}	$\tilde{B}, \tilde{W}, \tilde{H}, \tilde{H}$
$ M_2 < M_1 < \mu $	\tilde{W}, \tilde{H}	$\tilde{W}, \tilde{B}, \tilde{H}, \tilde{H}$
$ M_2 < \mu < M_1 $	\tilde{W}, \tilde{H}	$\tilde{W}, \tilde{H}, \tilde{H}, \tilde{B}$
$ M_1 < \mu < M_2 $	\tilde{H}, \tilde{W}	$\tilde{B}, \tilde{H}, \tilde{H}, \tilde{W}$
$ \mu < M_1 < M_2 $	\tilde{H}, \tilde{W}	$\tilde{H}, \tilde{H}, \tilde{B}, \tilde{W}$
$ \mu < M_2 < M_1 $	\tilde{H}, \tilde{W}	$\tilde{H}, \tilde{H}, \tilde{W}, \tilde{B}$

3.4 pMSSM

All of the above sections denote particle sectors of the MSSM. However, as already mentioned before, the MSSM has a phenomenological downside: its enormous parameter space. Therefore, the focus of this thesis is on two more restricted versions of the MSSM: the pMSSM and the cpMSSM. In this section the focus will be on the first, explaining its assumptions and their consequences.

To reduce the number of parameters, the pMSSM imposes four requirements on the theory:

1. No new sources of CP violation, relative to the SM.
2. The first and second generation sfermions are mass-degenerate.
3. The sfermion mass matrices are diagonal, i.e. no sfermion mixing.
4. The trilinear couplings within equation 3.44 for the first and second generation sfermions are set to zero.

The first and third requirements follow from strict experimental bounds. For the first this is of course the amount of CP violation, whereas the third is based on the upper bound of flavour violation [23]. The other two constraints limit the enhancement of rare decays and meson mixing. Examples of rare decays are: $\mu^- \rightarrow e^- \gamma$, $B_s \rightarrow \mu^+ \mu^-$ and $\tau^- \rightarrow \mu^- \gamma$. The fourth constraint also has a further justification in the fact that, as explained, the trilinear couplings are linked with the Yukawa couplings. As we know, the Yukawa couplings are related to the mass of the corresponding fermion, therefore we can use that relative to the top, bottom and τ mass the other Yukawa couplings are approximately zero. Then, given the mentioned link, we can somewhat justifiably assume the trilinear couplings to also be zero, except for the heaviest (third) generations. Lastly, the Higgs sector is now as described without CP violation, as demanded by the first requirement,

3.4.1 Parameters

Through the usage of these requirements the parameter space of the MSSM has been reduced to 19 parameters. All these parameters are shown and briefly explained in table 3.4.

Table 3.4: The 19 (soft) SUSY breaking parameters of the pMSSM and a small description [17].

Symbol	Description
$m_{\tilde{Q}_1}$	Mass of the left-handed squarks of the first and second generation.
$m_{\tilde{Q}_3}$	Mass of the left-handed squarks of the third generations.
$m_{\tilde{u}_R}$	Mass of right-handed up-type squarks of the first and second generation.
$m_{\tilde{d}_R}$	Mass of right-handed down-type squarks of the first and second generation.
$m_{\tilde{t}_R}$	Mass of right-handed top squark.
$m_{\tilde{b}_R}$	Mass of right-handed bottom squark.
$m_{\tilde{L}_1}$	Mass of the left-handed sleptons of the first and second generation.
$m_{\tilde{L}_3}$	Mass of the left-handed slepton of the third generation.
$m_{\tilde{e}_R}$	Mass of right-handed sleptons of the first and second generation.
$m_{\tilde{\tau}_R}$	Mass of right-handed stau.
M_1, M_2, M_3	Masses of the bino, wino and gluino.
$\mathbf{A}_t, \mathbf{A}_b, \mathbf{A}_\tau$	Trilinear couplings of the third generation: stop, sbottom and stau.
$\tan \beta$	Ratio of the vacuum expectation values of the two Higgs doublets.
$m_{H_u}^2, m_{H_d}^2$	The squared Higgs masses within $\mathcal{L}_{\text{SOFT}}^{\text{MSSM}}$.

At this point two model parameters are left: $|\mu|$ and b . These can be calculated using the tadpole equations (3.56). However, this choice of dependent and free parameters is no more than a choice. It is possible to have $|\mu|$ and/or b as a free parameter as well. To be more precise, we can choose four free parameters from the set of $m_{H_u}^2, m_{H_d}^2, \tan \beta, b, |\mu|$ and M_Z ,²⁶ where the remaining two are then determined by the tadpole equations.²⁷

3.5 cpMSSM

The pMSSM is studied quite a lot, however we are also looking slightly beyond. One of the possibilities is to have a look at CP-violating observables with SUSY. For these observables, the pMSSM is not a suitable model, as the pMSSM explicitly does not introduce extra CP violation. Therefore we will look at another model for these observables called the cpMSSM. Within the cpMSSM the first requirement of the pMSSM (as listed in section 3.4) is lifted, resulting in extra CP violation being allowed compared to the SM. All other requirements mentioned remain intact.

Aside from research into interesting CP-violating observables within SUSY, lifting the removal of CP-violation has more benefits. One of such benefits is related to the antimatter-matter asymmetry within the universe, the so-called baryon asymmetry. This asymmetry describes the fact that within the observable universe there is a clear imbalance between the amount of matter and anti-matter. Currently, we do not know how this imbalance came to be, as the SM itself cannot fully explain it. In 1967, Andrei Sakharov proposed three requirements for an interaction that could generate this imbalance [7], one of which is the existence of enough CP violation. Therefore by allowing extra CP violation within SUSY, we might also solve another problem.

As a result of re-introducing CP-violation, nine parameters can, in principle, obtain a phase. These are listed in table 3.6. However, only six of those are independent. Firstly, it should be noted that there are two

²⁶Here note that even though M_Z is an experimentally measured parameter, there is no inherent reason in the context of the theory for this parameter/value to not depend on other parameters.

²⁷The sign of μ cannot be determined from the tadpole equations, and should always be specified as input for any calculation software.

accidental global $U(1)$ symmetries present within the MSSM Lagrangian. These are:

$$\phi \rightarrow e^{iQ_a\omega_a}\phi, \quad \phi \rightarrow e^{iQ_b\omega_b}\phi, \quad (3.72)$$

where ϕ represents an arbitrary field. Further Q_a and Q_b are the $U(1)$ charges and ω_a and ω_b the generators [24, 25, 26, 17]. These rotations leave the Lagrangian invariant if we use the correct charges (table 3.5) and transform the parameters according to:

$$\begin{aligned} \mu &\rightarrow e^{2i(\omega_a+\omega_b)}\mu \\ b &\rightarrow e^{4i\omega_a}b \\ M_j &\rightarrow e^{2i(\omega_a-\omega_b)}M_j \\ \mathbf{A}_k &\rightarrow e^{2i(\omega_a-\omega_b)}\mathbf{A}_k \end{aligned} \quad (3.73)$$

Table 3.5: Charges associated with the $U(1)_a$ and $U(1)_b$ symmetries that can still be introduced, while keeping the Lagrangian invariant. Note that for the first row, the charges are for the left-handed fields. The non-conjugated right-handed fields would have had opposite charges.

Sparticles	Q_a	Q_b	Particles	Q_a	Q_b
sfermions	0	1	fermions	1	0
higgsinos	-1	-1	Higgs bosons	-2	0
gauginos	-1	1	gauge bosons	0	0

The above transformations present us with the possibility to rotate away two phases that can be introduced for these parameters. These would be introduced through a $e^{i\phi}$ factor that can now be absorbed by the transformation of 3.73 by setting ω_a and ω_b appropriately. Typical choices in this case are to set the phase of b and M_3 to zero, which is also the case within this thesis. Secondly, we, again, have the tadpole equations (3.56), which on top of two parameters also fix one phase. In the case of this thesis this is used to set $\eta = 0$.

As was the case within the pMSSM we still can use the tadpole equations to set our free parameters. Table 3.6 lists all parameters of the cpMSSM and the possible CP-violating phases that can be introduced, of which 25 are free.

Table 3.6: All cpMSSM parameters and the possible phases, of which 25 (19 real parameters and 6 phases) are independent [17].

Real Parameters								Phases		
$m_{\tilde{Q}_1}$	$m_{\tilde{Q}_3}$	$m_{\tilde{L}_1}$	$m_{\tilde{L}_3}$	$\tan\beta$	$ M_1 $	$ \mathbf{A}_t $	ϕ_{M_1}	$\phi_{\mathbf{A}_t}$	η	
$m_{\tilde{u}_R}$	$m_{\tilde{t}_R}$	$m_{\tilde{e}_R}$	$m_{\tilde{\tau}_R}$	$ b $	$ M_2 $	$ \mathbf{A}_b $	ϕ_{M_2}	$\phi_{\mathbf{A}_b}$	ϕ_b	
$m_{\tilde{d}_R}$	$m_{\tilde{b}_R}$	$m_{\tilde{H}_d}^2$	$m_{\tilde{H}_u}^2$	$ \mu $	$ M_3 $	$ \mathbf{A}_\tau $	ϕ_{M_3}	$\phi_{\mathbf{A}_\tau}$	ϕ_μ	

Chapter 4

Observables

As mentioned in chapter 1 this thesis will have a look at the effect of CP-violating phases within the cpMSSM on the dark matter relic density. As mentioned in section 3.5 the introduction of those phases is very limited by experimental observations. This chapter will present and explain the observables in the context of the (c)pMSSM that are important for this thesis.

4.1 Electron Electric Dipole Moment

We first will have a look at the electric dipole moment and magnetic moment of leptons. These two observables are very closely related and are both very sensitive to physics beyond the SM. In the case of the electric dipole moment of the electron the SM itself predicts a value that is orders of magnitudes below the current limits. Depending on the SUSY parameters, SUSY can give rise to large measurable contributions, making these observables prime objects to study SUSY itself.

In this thesis we will mostly focus on the electric dipole moment of the electron. The electron Electric Dipole Moment (eEDM) is one of the most stringent observables for the added phases of the cpMSSM. A smaller focus within this thesis will also be on the magnetic moment of the muon. This observable partially constrained the training data used within this thesis, cf. chapter 5. Also, the magnetic moment of the muon is of further interest due to a long-standing, possible 4σ discrepancy of its experimental value and the SM prediction [27, 28, 29].¹ However, there is much discussion about this discrepancy. This discussion mostly focuses on the value that is predicted by the SM. Two different ways to determine that value (data-driven and lattice QCD) report quite different results [30, 28, 29, 31, 32, 33]. With enough difference between them to either have agreement between SM and experiment or fully falsify the SM prediction.

Both observables represent an interaction of the lepton's spin with the electromagnetic field. In the classical Hamiltonian this is represented as:

$$H = -\vec{\mu} \cdot \vec{B} - \vec{d} \cdot \vec{E}, \quad (4.1)$$

where we define the moments for the lepton l as

$$\vec{d}_l = d_l \vec{\sigma} = 2d_l \vec{S}, \quad (4.2)$$

$$\vec{\mu}_l = g_l \frac{-e}{2m_l} \vec{S}, \quad (4.3)$$

with $\vec{S} = \vec{\sigma}/2$ the spin of the lepton. Here g_μ is called the 'g-factor', and at tree level is calculated to be 2 for all leptons. Actually, the interest goes to the anomalous magnetic moment:

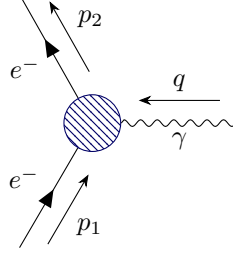
$$a_l = \frac{g_l - 2}{2}, \quad (4.4)$$

¹Note that officially the discrepancy is with the anomalous magnetic moment (a_μ), which is defined in this section.

which defines the difference of that g-factor with respect to its tree-level value.

The CP violation of the EDM term is understood classically in equation 4.1. A T transformation will flip the spin and the magnetic field. Because the magnetic field is present in the first term, this does not flip the sign of the first term. However, for the second term we do get a flip in sign: $-d(\vec{S} \cdot \vec{E}) \rightarrow +d(\vec{S} \cdot \vec{E})$. By the CPT invariance of the full model we then directly get that CP must also be violated by the EDM term.

To determine the exact expressions for the eEDM we start at the general structure of the electromagnetic interaction of an electron:



The corresponding matrix element is given by:

$$i\mathcal{M} = -ie\bar{u}(p_2)\Gamma^\mu u(p_1)\epsilon_\mu(q), \quad (4.5)$$

where Γ^μ denotes the correct vertex structure and $\epsilon_\mu(q)$ the polarization vector of the photon. For intuition, at tree level this would reduce to:

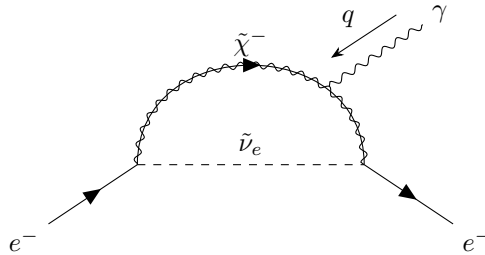
$$i\mathcal{M} = -ie\bar{u}(p_2)\gamma^\mu u(p_1)\epsilon_\mu(q). \quad (4.6)$$

The next step is to determine which part of that general diagram corresponds to an observable associated with it. This procedure first requires us to know which loop diagrams we should consider. SM diagrams only start to contribute to the eEDM at four-loop order. The only source of CP violation within the SM is the CKM matrix,² which will not emerge in matrix elements at one-loop order. At second loop order the non-absorbed phases of the CKM matrices will cancel each other, and thus no CP violation is present. At three-loop level the diagrams, unexpectedly, add up to zero [34]. Finally, at 4-loop order there is an SM contribution towards the eEDM [35]:

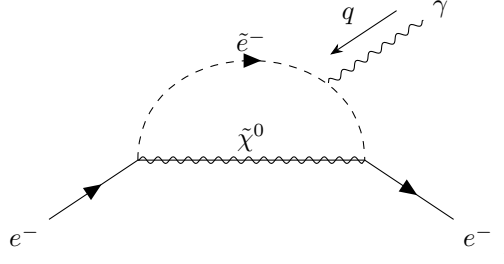
$$d_e \leq 10^{-38} \text{ e cm}, \quad (4.7)$$

denoted in the conventional unit for an EDM: [e cm], which corresponds with $1/1.973269788 \cdot 10^{-14} \text{ e GeV}^{-1}$ [36]. Within the calculation software the baseline eEDM value of the SM is actually set to 10^{-37} .

Given this extremely low SM value, for the main contribution to the prediction of the eEDM by the cpMSSM we only have to look at SUSY diagrams. At first order the contributing SUSY diagrams are:



²As mentioned before we assume only left-handed neutrinos to exist, if right-handed neutrinos were present the PMNS matrix would introduce another source of CP violation.



It is possible to single out the contribution of those diagrams to the eEDM [17].³ The 1-loop contribution of the cpMSSM becomes:

$$\begin{aligned} \left(\frac{d_e}{e}\right)^{\tilde{\chi}^\pm} &= \frac{1}{16\pi^2} \sum_{k=1}^2 \frac{m_{\tilde{\chi}_k^\pm}}{m_{\tilde{\nu}_e}^2} \Im(-gV_{k1}\mathbf{y}_e U_{k2}) A(m_{\tilde{\chi}_k^\pm}^2/m_{\tilde{\nu}_e}^2), \\ \left(\frac{d_e}{e}\right)^{\tilde{\chi}^0} &= \frac{-1}{16\pi^2} \sum_{i=4}^4 \sum_{m=1}^2 \frac{m_{\tilde{\chi}_i^0}}{m_{\tilde{e}_m}^2} \Im((G_{im}^R)^* G_{im}^L) B(m_{\tilde{\chi}_i^0}^2/m_{\tilde{e}_m}^2). \end{aligned} \quad (4.8)$$

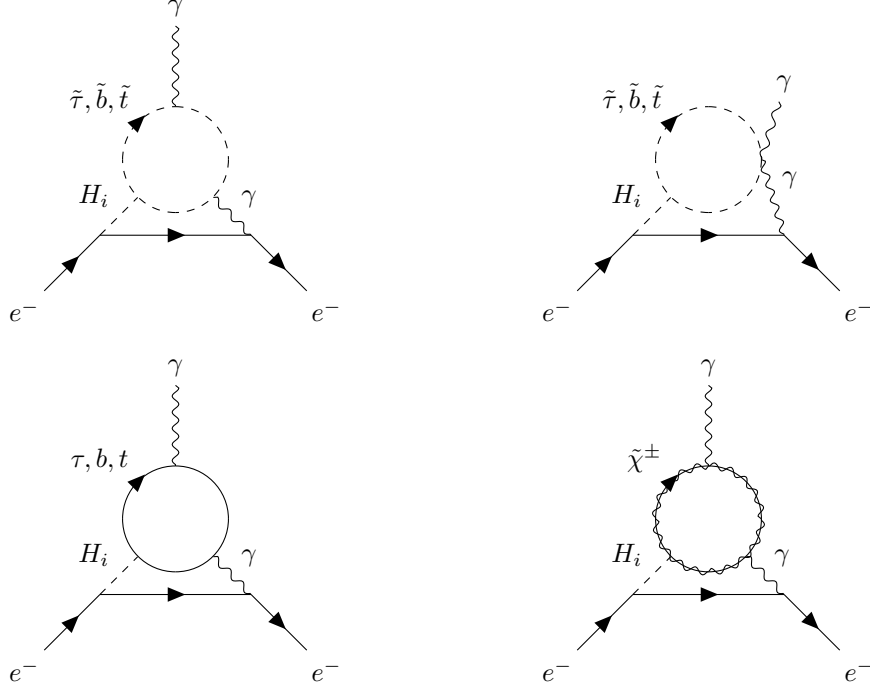
All coupling terms in equation 4.8 are expressed in Appendix A.2 and all loop functions (A and B) in Appendix A.3. \mathbf{V} and \mathbf{U} are the mixing matrices of the charginos. Further, the $m = 1, 2$ subscript for the selectron denotes the left or right-handed field and $i = 1, 2, 3, 4$ denotes the possible choices of neutralino eigenstate used as propagator, with $k = 1, 2$ denoting the chargino mass eigenstate.

The calculation software that will be used in this thesis calculates the contributions of the eEDM up to dominant 2-loop diagrams.⁴ Therefore the expression for these dominant 2-loop diagrams will also be given. Note that the 2-loop corrections might be of the same order of magnitude as the 1-loop corrections, as the SUSY parameters that determine these corrections can be different from those that determine the 1-loop corrections.

³This is done through the usage of projection operators. For more clarification/explanation see [17].

⁴For more details regarding the calculation software see C.

For 2-loop corrections we have to look at the following SUSY diagrams:



Within these diagrams H_i denotes all three neutral Higgs bosons. The four diagrams above are called the *Barr-Zee* diagrams [37].

Again, by using projection operators we can determine the exact expression for 2-loop contribution to the eEDM within the cpMSSM [17]. In most circumstances this is predominantly induced by the CP-violating phases of the charginos and the third generation fermions and sfermions [38]:

$$\begin{aligned}
\left(\frac{d_e}{e}\right)^{BZ} = & \sum_{q=t,b} \left\{ \frac{3\alpha_{\text{em}} Q_q^2 m_e}{32\pi^3} \sum_{i=1}^3 \frac{g_{H_i e^+ e^-}^P}{m_{H_i}^2} \sum_{j=1,2} g_{H_i \tilde{q}_j^* \tilde{q}_j} F(\tau_{\tilde{q}_j i}) \right. \\
& + \frac{3\alpha_{\text{em}} Q_q^2 m_e}{8\pi^2 s_W^2 m_W^2} \sum_{i=1}^3 \left[g_{H_i e^+ e^-}^P g_{H_i \tilde{q} q}^S f(\tau_{qi}) + g_{H_i e^+ e^-}^S g_{H_i \tilde{q} q}^P g(\tau_{qi}) \right] \Big\} \\
& + \frac{\alpha_{\text{em}} m_e}{32\pi^3} \sum_{i=1}^3 \frac{g_{H_i e^+ e^-}^P}{m_{H_i}^2} \sum_{j=1,2} g_{H_i \tilde{\tau}_j^* \tilde{\tau}_j} F(\tau_{\tilde{\tau}_j i}) \\
& + \frac{\alpha_{\text{em}}^2 m_e}{8\pi^2 s_W^2 m_W^2} \sum_{i=1}^3 \left[g_{H_i e^+ e^-}^P g_{H_i \tau^+ \tau^-}^S f(\tau_{\tau i}) + g_{H_i e^+ e^-}^S g_{H_i \tau^+ \tau^-}^P g(\tau_{\tau i}) \right] \\
& + \frac{\alpha_{\text{em}}^2 m_e}{4\sqrt{2}\pi^2 s_W^2 m_W} \sum_{i=1}^3 \sum_{j=1,2} \frac{1}{m_{\tilde{\chi}_j^\pm}} \left[g_{H_i e^+ e^-}^P g_{H_i \tilde{\chi}_j^+ \tilde{\chi}_j^-}^S f(\tau_{\tilde{\chi}_j^\pm i}) + g_{H_i e^+ e^-}^S g_{H_i \tilde{\chi}_j^+ \tilde{\chi}_j^-}^P g(\tau_{\tilde{\chi}_j^\pm i}) \right].
\end{aligned} \tag{4.9}$$

Again, all couplings and loop functions are given in Appendix A.2 and A.3. Furthermore, we use $\tau_{xi} = m_x^2/m_{H_i}^2$, $\alpha_{\text{em}} = \frac{e^2}{4\pi}$, $c_W = \cos(\theta_W) = m_W/m_Z$, $s_W = \sin(\theta_W) = \sqrt{1 - c_W^2}$ and Q_q as the charge of the quark q in units of e .

Currently, the most precise measurement of the eEDM is that of [39]. In this experiment the eEDM was determined to have an upper limit of:

$$d_e \leq 4.1 \cdot 10^{-30} \text{ e cm.} \tag{4.10}$$

However, this thesis is meant as an extension of (and a comparison with) a previous study [17]. This previous study was published around the same time as this new limit, obstructing it from actually using the new limit. Therefore, to make any comparison between this work and the important works that came before, we opted to use an older eEDM constraint. This upper limit is [40]:

$$d_e \leq 1.1 \cdot 10^{-29} \text{ e cm}, \quad (4.11)$$

where this limit has a 90 % confidence level. However, the newer limit should always be kept in mind for future research and/or the future outlook of this thesis.

4.2 Relic Density

This thesis will try to study the effects that CP-violating phases of the cpMSSM have on the relic density. How we will aim to do so, and what type of machine learning will be used is to be discussed within chapters 5 and 7. However, before we can do so we need to understand what the relic density is. This section aims to fill that gap.

The dark matter relic density is exactly as its name states: the relative amount of Dark Matter (DM) particles left in a stable state, i.e. a relic from previous times. In the early universe the temperature was high enough for the (pairwise) creation of DM particles or particles that could become DM. In this hot, early universe the number density n of DM particles follows the Boltzmann equation [41]

$$\frac{dn}{dt} = -3Hn - \langle \sigma_{\text{ann}} v \rangle (n^2 - n_{\text{eq}}^2), \quad (4.12)$$

where H is the Hubble parameter, expressing the time-dependent expansion rate of the universe, and $\langle \sigma_{\text{ann}} v \rangle$ is the velocity-weighted cross-section of the annihilation process of the DM candidate into SM particles in the early universe. Usually the Hubble parameter is expressed as $H = 100h \text{ km s}^{-1} \text{ Mpc}^{-1}$ [36].⁵ Thus, once the number density reaches an equilibrium (n_{eq}) the number density only goes down due to this expansion. After a certain amount of time the universe cools down due to this expansion, and the DM density has dropped to such a level that there will not be enough DM particles around anymore for annihilation or creation processes to occur at all. For annihilation the density of particles around has literally become too low. Moreover, for creation the temperature has become too low, resulting in the process becoming kinematically impossible. Thus, at that point, only decay would still be a possibility. However, our LSP DM candidate can neither decay into only SM particles due to R-parity,⁶ nor into SUSY particles since it is the lightest particle of that type. Thus, eventually, a stable number of DM particles is reached. The total mass density left is called the relic density and is thus determined by the number of DM particles left at the point that the universe is sufficiently cooled down. The above-described process is called thermal freeze-out.

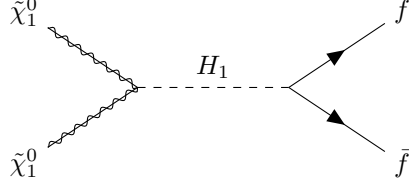
Currently, experimental observations of the Planck satellite put the present-time relic density, $\Omega_{\text{Planck}} h^2$, at 0.120 ± 0.001 [42]. For practical purposes it is okay to accept models that predict relic densities between 0.09 and 0.15. This range is deemed okay as on top of an experimental uncertainty there also is a larger theoretical uncertainty. Especially, the lower values are considered viable. The idea in that case is that the SUSY DM candidate could only be a part of the total dark matter. The relic density ‘leftover’ by SUSY could thus be explained by another type of DM.

The amount of DM left is influenced by the parameter configuration of the pMSSM or cpMSSM model. First of all, the parameters determine which particle is the lightest SUSY particle. For this particle to be a suitable DM particle, it needs to have no charge and no colour. Thus we need the lightest SUSY particle to be the lightest neutralino or sneutrino. However, the sneutrino as DM candidate is experimentally excluded [43]. If the LSP is a neutralino, the parameters still influence the value of the relic density in other manners

⁵Strictly speaking we have no evidence from this time. The cosmic microwave background is the earliest evidence we have, which originates after the end of the early universe.

⁶There are MSSM models that do not impose R-Parity, in which case the DM particle would be allowed to decay. R-parity violating models are not considered within this thesis.

too. This happens through $\langle\sigma_{\text{ann}}v\rangle$. In other words, the parameters influence how efficiently the DM particle annihilates within the early universe. The more efficient, the fewer DM particles left after freeze-out, the lower the relic density. A good example is that of annihilation using a scalar Higgs boson as s-channel propagator:



Of course, this process becomes more efficient if the numerator within the propagator becomes closer to zero. This resonance happens when: $m_{\tilde{\chi}_1^0} \approx m_{h^0}/2$. Note that we are assuming a low enough temperature of the universe for this non-relativistic resonance.⁷ As this resonance is determined by the mass of the LSP, the efficiency of the process is governed by the associated parameters, which are: M_1, M_2, μ and $\tan\beta$. Three of these parameters are free parameters of the model. However, it could also be that other parameters play a strong role. Examples would be parameters included in the trilinear soft SUSY breaking terms.

It is good to note that there is another option besides (self-)annihilation: co-annihilation. This means that another particle, or other particles, annihilate(s) with the DM particle into only SM particles: $\tilde{\chi}_1^0 + X \rightarrow SM + SM$. In that case we get, for co-annihilation partners i and j :

$$\frac{dn}{dt} = -3Hn - \langle\sigma_{\text{co-ann}}v\rangle(n^2 - n_{\text{eq}}^2), \quad (4.13)$$

$$\langle\sigma_{\text{co-ann}}v\rangle = \sum_{i,j=1}^N \langle\sigma_{ij}v_{ij}\rangle \frac{n_i^{\text{eq}}}{n^{\text{eq}}} \frac{n_j^{\text{eq}}}{n^{\text{eq}}}. \quad (4.14)$$

To clarify: N is the number of particles that participate in co-annihilation and i and j are labelling those particles. One of the N particles has to be the DM particle for which $n_{\text{DM}}^{\text{eq}} = n^{\text{eq}}$. Further v_{ij} and σ_{ij} are the relative velocity and co-annihilation cross-section respectively for particles i and j . However, co-annihilation is suppressed by the temperature within the early universe T and the mass of the non-DM particle:

$$\frac{n_j^{\text{eq}}}{n^{\text{eq}}} \propto \exp\left(-\frac{m_j - m_{\text{DM}}}{T}\right). \quad (4.15)$$

Therefore, for co-annihilation to provide a significant contribution to the value of the relic density we need the mass of the co-annihilation partner to be close to the mass of the DM candidate.

In this thesis we will categorize pMSSM points according to the following dominant processes for the relic density:

- H1/H2-funnel: Annihilation with a H_1/H_2 scalar boson featuring as propagator in the s-channel.
- Z-funnel: Annihilation with a Z boson featuring as propagator in the s-channel.
- Chargino Co-annihilation: Co-Annihilation with the lightest chargino.
- Neutralino Co-annihilation: Co-Annihilation with the second lightest neutralino.
- Sbottom Co-annihilation: Co-Annihilation with the lightest sbottom.
- Stau Co-annihilation: Co-Annihilation with the lightest stau.

⁷This process is dominant in the phase before freeze-out, where only DM DM \rightarrow SM SM is realistically possible due to the ever cooling down temperature of the universe.

- Slepton Co-annihilation: Co-Annihilation with the lightest slepton eigenstate of the first two generations.
- Stop Co-annihilation: Co-Annihilation with the lightest stop.
- Squark Co-annihilation: Co-annihilation with the lightest squark eigenstate of the first two generations.
- Gluino Co-annihilation: Co-annihilation with the gluino.
- Bulk: a (c)pMSSM model in which none of the above processes is dominant.

For most of these categories we will determine the effect of CP-violating phases on the dark matter relic density. Only for the categories of stop, squark and gluino co-annihilation the pMSSM points needed are not phenomenologically interesting, as these points would require TeV masses for the lightest neutralino. These types of points are not close to being probed by current experiments. Therefore, we will *not* study these categories in chapter 7.

Chapter 5

Machine Learning Methodology

One of the aims of this thesis is to create a new sampling method to get cpMSSM points from a given pMSSM point more efficiently and effectively. After formalising this goal, this chapter will introduce and explain the machine learning model that ultimately was used as sampler. In addition, the dataset creation, learning of the model and inference of the model are introduced in this chapter. This chapter does not include the performance of the model. How the performance is determined and the corresponding results will be presented in the next chapter.

5.1 Context

Research into the cpMSSM is currently limited by the amount of (correct) parameter configurations (points) that are easily available. The aim would be to replace the very ‘handcrafted’ Gaussian Particle Filters (GPF). GPFs work in essence through Gaussian sampling. Samples are generated using a Gaussian distribution centred around an already available (c)pMSSM point. This method has two main downsides: firstly, the need for an already available point. Through using such a point a bias could be introduced, as this seems to define a ‘starting point’ for exploration of the available parameter space. Such a ‘starting point’ cannot be motivated by physics. Physics-wise a point is correct or not correct according to experimentally found limits on observables. There is no natural predilection within that judgement, and thus no ‘starting point’. By then introducing an artificial point to start your exploration, the sampling might get stuck at points similar to the first, and might never be able to exhaustively explore the parameter space. In other words, it might be biased towards one region of the parameter space. Secondly, GPFs are very reliant on fine-tuning by the user. To combat the first downside, the user could set the Gaussian distribution to have extreme variances. However, that would make the sampling rather naive and most likely rather inaccurate. It is exactly this balance of accuracy versus broadness of exploration/sampling that makes the usage of GPFs very nonautomated.

A replacement sampler would therefore have to work automated: given a pMSSM point, it directly outputs a set of phases that would create the required amount of cpMSSM samples based on the original pMSSM point. Ideally, the sampler would be able to do this with a sufficient amount of accuracy, while also exhaustively sampling the explorable phase-space. For a model to have such capabilities it would need to understand the conditional distribution of those cpMSSM phases and be able to sample from it. Ideally, this means that the model seemingly understands the physics behind the distribution. However, as long as the performance is somewhat sufficient, this is not required: it just needs to work.

This thesis will aim to find this replacement sampler within the field of Machine Learning (ML). ML models naturally have the required inference procedure: give it an input and it outputs the desired output for that input if learned correctly. Furthermore, ML models are still very efficient during inference, improving overall efficiency as well. We formalize the goal of the machine learning model within the following ‘research question’:

Can we use a machine learning model to effectively and efficiently sample cpMSSM points conditioned on a pMSSM point?

The methodology used to answer this question is described in this chapter.

5.2 Normalizing Flow

5.2.1 Motivation

The first sub-question that comes to mind after posing this question is what type of ML model to use. Naturally, more than one answer is possible. However, the choice for a sampler becomes slightly easier if we take into account the background of the goal. Most sampling methods learn to sample via the replication of training data. Examples of these methods are: Variational AutoEncoders and Generative Adversarial Networks [44, 45]. In essence, this is contrary to our goal: if we already had a representative set of data, why need a new sampler? We need to, as best as possible, understand the distribution of points allowed. Such an understanding hopefully enables the model to sample new cpMSSM points as well, not just more of the same. There is currently only one conventional (conditional) sampler that had such a motivation at its core when it was introduced: Normalizing Flows [46].

In contrast to the other methods, this model learns via *directly* optimizing the likelihood of the training data given. Thus, instead of replicating the data it learns an underlying distribution (likelihood) that should fit the training data. This could lead to the model outputting samples that do not really resemble the points of the training data but do follow the same distribution. The idea is that this should correspond with correct samples according to the experimental limits used for the training data.

5.2.2 Explanation

A normalizing flow consists of two core elements:

- A base distribution that is both easy to sample and has an easily calculated likelihood
- A set of ‘bijectors’: these are bijective, parameterized transformations with a known Jacobian.

The Jacobian is defined as:

$$J_{i,j} = \det\left(\frac{\partial y^i}{\partial x^j}\right), \quad (5.1)$$

for $y(x)$ a general transformation, and i, j labelling the dimensions of the domain and range of that transformation. The idea behind these elements is that a complicated distribution can be sampled by sampling from the base distribution and transforming the sample through the bijectors. The parameters of the bijectors are then learned such that the ultimate distribution resembles that of the training data distribution. We denote the base distribution by p_0 and the distribution after i transformations/bijectors as p_i . Furthermore, the likelihood of point z_0 sampled from p_0 is denoted by: $p_0(z_0)$. Lastly, by indicating the bijectors by f we have:

$$z_1 = f(z_0; \theta) \quad \text{and} \quad z_0 = f^{-1}(z_1; \theta), \quad (5.2)$$

where θ denotes the learnable parameters of that specific bijector. Because the Jacobian of the bijector is known, according to the second requirement, we find for the (reversed) transformation of p_1 tot p_0 :

$$p_1(z_1; \theta) = p_0(z_0) \left| \det \frac{\partial z_0(\theta)}{\partial z_1} \right| \quad (5.3)$$

$$= p_0(z_0) \left| \det \left(\frac{\partial z_1}{\partial z_0(\theta)} \right)^{-1} \right| \quad (5.4)$$

$$= p_0(z_0) \left| \det \frac{\partial z_1}{\partial z_0(\theta)} \right|^{-1}, \quad (5.5)$$

where $z_0(\theta) = f^{-1}(z_1, \theta)$ and we are allowed to pull out the inverse, as the transformations, and thus their Jacobians, are injective. The equation can be rewritten as:

$$\log p_1(z_1; \theta) = \log p_0(z_0) - \log \left| \det \frac{\partial z_1}{\partial z_0(\theta)} \right|. \quad (5.6)$$

Equation 5.6 is then generalized for K bijectors to:¹

$$\log p_K(z_K; \theta) = \log p_0(z_0) - \sum_{i=1}^K \log \left| \det \frac{\partial z_i}{\partial z_{i-1}(\theta)} \right|. \quad (5.7)$$

Equation 5.7 shows the original motivation of normalizing flows. To be able to sample from the target distribution we need the parameters (θ) on the LHS to optimally represent the (underlying) distribution of the training data. However, we do not analytically understand the target distribution itself. But now we have an exact equality for that target distribution with understandable and easily calculable terms. This gives us three possibilities. Firstly, we can now directly optimise towards the target likelihood, by optimising the model through the RHS of equation 5.7 for the available training data. In practice, such an optimisation means that we use gradient descent. Gradient descent is a procedure in which the gradient of a function, with respect to the learnable parameters of that function, is calculated for the available data. This gradient is then used to update these parameters by taking small steps in the direction of that gradient. In theory, this should push the parameters towards the optimum of that function according to the training data. In the case of normalizing flows, we want to find the optimum of θ for the RHS of equation 5.7. Secondly, we can sample from the target distribution, by sampling from the base distribution and transforming that sample through the usage of the bijectors.² Lastly, we can calculate the likelihood of samples, simply by calculating equation 5.7 for a specific sample.

5.2.3 Rational Quadratic Spline

Bijectors have been proposed in a lot of variations, for this thesis the choice of bijectors fell on Rational Quadratic Splines (RQS) [47]. The transformation of this bijector can be summarised as follows, and a visualization of this concept is given in figure 5.1. First a part of the input of the transformation is split off and used as input for a small neural network.³ The output of this neural network is used for two things. A part is used as a bin value; at each of these values we need to set a gradient and function value for the ultimate transformation. The gradients and function values are provided by the other part of the output from the neural network. By setting the gradients of the transformation on each bin edge, the gradient itself is made to be a piecewise linear function by connecting the dots. This results in a transformation, calculated by piecewise integration, that is a piecewise quadratic function. Further, as we also set the value of the transformation itself we get some more freedom, enabling us to let the transformation be a ratio of two quadratic functions, which has double the expressive power. As the transformation is a combination of polynomial features everywhere, the Jacobian is calculable. In addition, the transformation values are restricted to be increasing over the bins, which makes it a bijective transformation. The second part of the original input is then transformed via the now specified transformation from the small neural network. By making this split of original input random over different RQs the whole base input is ultimately transformed at some point.

The concept behind RQs can be changed into a conditional setting. The vector that represents the condition is appended or prepended to the input of the small neural network within each bijector. In this way, the transformation becomes dependent on the condition given, and the model should also be able to learn conditional target distributions, as required for our problem setting.

¹Note that this equation in no way limits the type of bijectors used any further than the two posed requirements. As such, a lot of freedom to choose a type of bijector is still present and one could even use different ones together.

²The usage of bijectors means that we transform the samples as in equation 5.2

³The small neural network used here mostly is a Multi-Layer-Perceptron (MLP) [48]

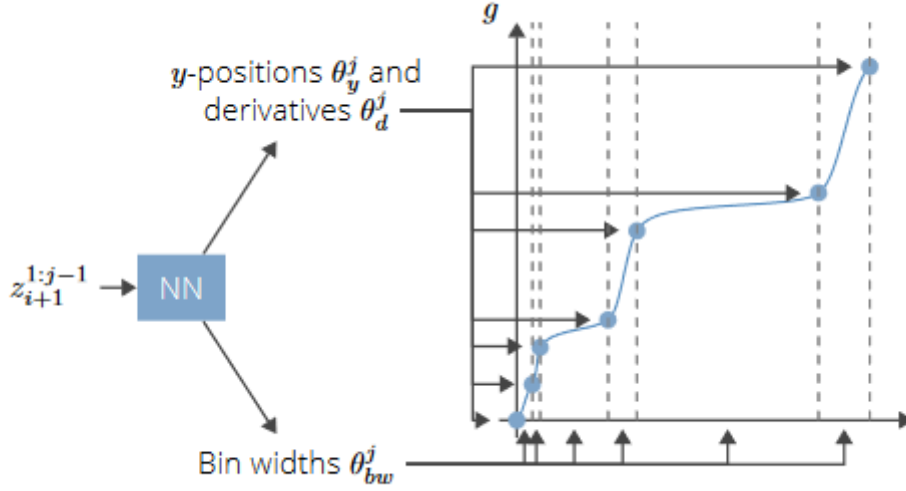


Figure 5.1: A visualization of the concept behind rational quadratic splines. The visualization is from the PhD thesis of Dr. Bob Stienen [49], which was also used as a guide for this section.

5.3 Dataset: The Creation Pipeline

This section introduces the pipeline/procedure for the creation of the necessary training and validation data. The full pipeline is depicted within figure 5.2. All steps are explained in detail in the subsections. The

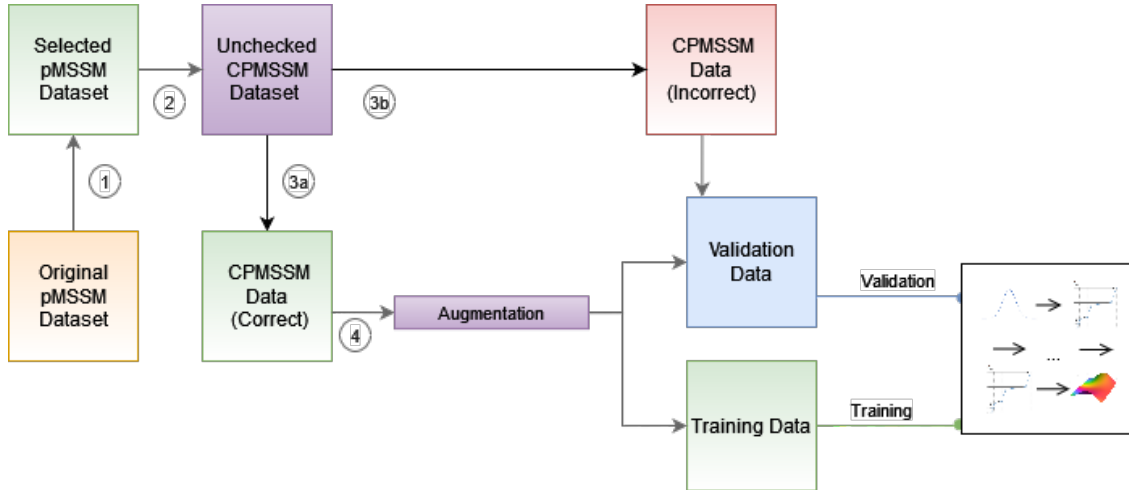


Figure 5.2: Visualization of the full pipeline for learning the normalizing flow.

Step 1: pMSSM selection (section 5.3.1), step 2: Naive sampling of phases (section 5.3.2), step 3: Calculating observables (section 5.3.3). Step 4: Augmentation of correct data points (section 5.3.4)

pipeline starts with an original dataset containing pMSSM data points. This dataset was readily available from previous research at the HEP department and consists of approximately 800.000 pMSSM points. Before the points could be used within this pipeline they needed to be checked on correctness according to multiple experimental limits.⁴ Of the original 800.000 points approximately 300.000 were within limits, and thus suitable for future training data.

⁴Which are listed in appendix C.3

The readily available dataset was influenced by the anomalous magnetic moment of the muon (4.1). The set of pMSSM points used in this thesis originates from a bigger dataset, which was created keeping in mind the anomalous magnetic moment value measurement [28, 29, 27]:

$$\Delta a_\mu = (a_\mu^{\text{exp}} - a_\mu^{\text{SM}}) \in [133 \cdot 10^{-11}, 369 \cdot 10^{-11}] \quad (5.8)$$

This bigger dataset was created by [50], and in that paper a subsequent full selection on the upper and lower limit of 5.8 is made, resulting in a reduced number of pMSSM points. For this thesis, we let go of the lower limit of 5.8, as there is discussion among the theoretical community whether the magnitude of a_μ should actually be lower (see section 4.1). Therefore, we used the bigger original dataset, but now only selected on using the upper limit of 5.8. This selection resulted in the aforementioned 800.000 non-checked pMSSM points, of which more than 300.000 remained after checking other experimental limits (C.3).

Important is that the ultimate dataset thus is not fully a_μ -independent, and even though removing the lower limits allows for larger masses, there will not be many points that have all sparticle masses in the multiple TeV range, as the original big dataset was still created with the a_μ lower range in mind.

5.3.1 pMSSM points

The first step of the pipeline aims to slim down the original dataset. We need to know the correctness of the to-be-created cpMSSM points. Therefore, these points will need to be put through the calculation software, as will be explained in section 5.3.3. To calculate, among others, the eEDM prediction of the cpMSSM point this software needs approximately five seconds. This time bottleneck makes it impossible to use 300.000 pMSSM points for this dataset, as for each pMSSM point we need a representative set of cpMSSM points checked, which we deemed to be about 1000 cpMSSM points per pMSSM point. Thus the 300.000 pMSSM points need to be slimmed down to about 50.000 to keep the calculation step within a practical time frame.

The selection of those pMSSM points can not be done naively: randomly selecting a number of points will not lead to the most representative set of points for the pMSSM parameter space, which could lead to detrimental performance of the ML model. There is no perfect metric to determine which set of points would be most representative, however, the sum of (euclidean) distances should be an indicator. The distance is calculated for the 6 parameters that receive phases within the cpMSSM as well as the a_μ prediction of the pMSSM point. This last parameter is included because it should partially represent the ranges of sparticle masses of the pMSSM points. Unfortunately, creating a subset of N points with the biggest sum of distances is not a trivial task. Therefore a greedy algorithm proposed by [51] is used. This algorithm consists of a random, initial set of points. From this set of points randomly one point is removed and replaced, storing which point is tested as replacement and removal. If the new group has a bigger sum of distances, keep the new configuration, otherwise the old. Repeat this procedure, with new replacements and removals each time, for at least $k \cdot N$ times, and afterwards stop if no improvement is found. The algorithm (with $k=2$) resulted in a 50 % increase of the sum of euclidean distances for a set of 47.500 points, compared with random selection.

The ultimate pMSSM dataset consists of 50.000 points: the above-mentioned 47.500 ‘representative’ correct points, and 2.500 randomly chosen incorrect pMSSM points. We choose to use those incorrect points for two reasons. Firstly, preliminary research showed that it is possible to use phases to get ‘out’ of experimental limits. Phases can have (small) effects on the masses or composition of mass eigenstates of sparticles. This will especially be shown for $\phi_{\mathbf{A}_t}$ in chapter 7 through its influence on the neutralino-composition parameter $|\mu|$. Through these small effects the cpMSSM point could just about adhere to experimental limits, especially if the pMSSM point was deemed incorrect by a small margin. In other words, the experimental limits become fuzzy due to the introduction of CP-violating phases. Secondly, it is also good to show the normalizing flow that incorrect pMSSM points exist, with the idea that the model will hopefully learn to handle these incorrect pMSSM points as well.

5.3.2 Naive Sampling

The second step in the creation pipeline is to create cpMSSM points for each of the 50.000 pMSSM points from the previous selection. Sampling is done through a naive, but fast, process. We know that larger phases result in larger eEDM contributions. Therefore, the phases are sampled with a logarithmic distribution in the interval $[-\frac{\pi}{2}, \frac{\pi}{2}]$ even around zero. Thus, in practice the phases are logarithmically sampled between 0 and $\frac{\pi}{2}$, and a random 50 % of the phases is given a minus sign. This procedure is done independently for each phase. This convention of phase interval works as long as the sign of the original pMSSM parameter is explicitly stored.

For each of the 50.000 pMSSM points, 1000 phase combinations are sampled. The full procedure is performed twice, thus resulting in 100 million data points. During the second round of sampling, the phases for M_2 and μ are limited to values up to 10^{-1} , as these phases are expected to be heavily contributing towards the cpMSSM prediction for the eEDM.

5.3.3 Calculation Software

The next step (3a/b) of the pipeline prior to training the model is determining the correct points within the 100 million cpMSSM points created. The (configuration of the) calculation software used is mentioned/explained in C. Afterwards the checked data is split into correct data points and incorrect data points. This split is made based on both the prediction of the eEDM for that parameter configuration, as well as other experimental limits on sparticle masses. Both the correct and the incorrect data points are saved to be used to train the ML model.

At this point some conventions in representation start to play a role. As mentioned in section 5.3.2 we sample phases for each parameter that acquires one in the cpMSSM. However, the calculation software needs the real and imaginary parts as input, and outputs the real and imaginary parts as well, whereas we want the ML model to learn to output phases based on the original, absolute pMSSM parameter. The transformations are made as follows, to keep in line with the interval of the phases:

$$\Re(P) = \text{Sign}(P) \cdot |P| \cdot \cos \phi_P, \quad (5.9)$$

$$\Im(P) = \text{Sign}(P) \cdot |P| \cdot \sin \phi_P, \quad (5.10)$$

$$P = \text{Sign}(\Re(P)) \sqrt{\Re(P)^2 + \Im(P)^2} (= \text{Sign}(P)|P|), \quad (5.11)$$

$$\phi_P = \arcsin\left(\frac{\Im(P)}{\text{Sign}(\Re(P)) \sqrt{\Re(P)^2 + \Im(P)^2}}\right), \quad (5.12)$$

where P denotes one of the parameters of the pMSSM that acquires a phase within the cpMSSM. With regards to the pipeline visualization of figure 5.2, in step 2 we transform P and ϕ_P to $\Re(P)$ and $\Im(P)$ and directly go back to P and ϕ_P in 3a/3b.

After the calculation software has determined the correct points, the correct data points will be used to learn the ML model. Together with 1 % of the correct phases, the incorrect phase vectors will be used to validate the ML model during and after learning. How the models are validated is described in chapter 6.

5.3.4 Augmentation Possibilities

The last step in the pipeline is the augmentation procedure on the correct cpMSSM points. Augmentation means changing data in such a way that it remains valid. In our case it turns out to be possible to flip all signs of the phases without changing the eEDM prediction. Therefore, we directly double the number of correct data points. This doubling of the dataset is very time-efficient, as we do not need the time-consuming calculation software and instantly double the number of available points.

We also tried to only flip the ‘one-loop parameters’: M_1, M_2 and μ . These are the phases that we know should contribute the most towards one-loop eEDM diagrams, and thus logically should be the most influential with regards to the eEDM. Flipping the sign of these phases resulted in 90% of the extra created points

remaining valid. This accuracy was deemed slightly too low, for now, to proceed with these extra points as well. However, for future research this possibility should be kept in mind. Especially as this augmentation multiplies the dataset by four, as we can use the original full augmentation on these points as well, without extra usage of the calculation software. Thus circumventing the time bottleneck of the calculation software. Results of the small study regarding these possible augmentation strategies can be found in table A.2. Due to this study, a precision problem of the calculation software was also brought to light.

5.3.5 The Result

After working through the full pipeline twice, as described in the above sections, a dataset as laid out in table 5.1 is created. Thus after the two creation phases, we have approximately *1.8 million* correct data

Table 5.1: Table showing relevant statistics of the dataset and its creation. From left to right: the size of the dataset after sampling, the number of correct points within the samples and the amount of time it took for the calculation software to check the points for correctness.

Creation Phase	Dataset Size	Correct Points	Time
1	50.000.000	719.567 (1.43%)	\pm 2.5 weeks
2	50.000.000	1.100.652 (2.20%)	\pm 3.5 weeks

points for the ML model to learn. The difference between the two creation phases lies in the restriction of the phases for M_2 and μ , as explained above. This resulted in a slightly higher acceptance percentage for that creation phase. Important to note is that, by using augmentation, practically we have *3.6 million* data points to work with.

5.4 Learning

The next step within the process of creating an ML model to sample cpMSSM points is to start learning the ML model. This section presents the used configuration of a normalizing flow, as well as the configuration of the learning process. For more details regarding how models are validated during and after learning, see chapter 6.

As mentioned we learn a normalizing flow model consisting of Rational Quadratic Splines as bijectors. To be more specific, the model consists of seven of those bijectors. In each of those blocks, we used a Multi-Layer-Perceptron (MLP) containing 2 layers and 512 intermediate features as the ‘small neural network’. The base distribution was a 7-dimensional Gaussian distribution, which makes the model also output 7 phases. The cpMSSM has 6 independent phases, as explained in 3.5. However, originally we opted to have the model output 7 phases, including a phase for M_3 . But due to an error in handling this phase in the calculation software, we opted to set this phase to zero afterwards. To be exact, Spheeno-CPV (see table C.1) set the gluino mass to be the real part of M_3 instead of the absolute value. Therefore, ϕ_{M_3} directly influenced the gluino mass, which should not be the case. This change should only have a negligible effect on the correctness of the model, as it is just a choice for the rotations mentioned in 3.5. While keeping the overall sum of phases lower should result in lower eEDM predictions, experience tells us. Lastly the condition prepended to the input of the small neural network is a vector representing the 19 free parameters of the pMSSM.

The learning configuration of the ML model consisted of the usage of an ADAM optimizer [52], which is a ‘fancy’ version of gradient descent. We set an initial learning rate, the step size towards the gradient of the target likelihood, of $5 \cdot 10^{-4}$. This value is relatively high for learning rates within ML. However, experts [53]⁵ and preliminary studies show a higher than usual learning rate to be beneficial. Further, we use a scheduler to drop this learning rate down over time in the learning process. The type of scheduler used was that of a plateau scheduler. This scheduler uses a metric, in our case the likelihood of the target distribution, to determine when to lower the learning rate. In our case, the scheduler checks if for 15 iterations over the data the likelihood has improved more than 0.001, if not the learning rate would be lowered by a factor of

⁵The code used to learn the model is also inspired by the code of Alex Kolmus for other types of normalizing flows.

0.1. The number of iterations over the data was set to 500.

The hardware used to learn the flow model consisted of one NVIDIA GeForce RTX 2080 Ti GPU and 12 Xeon 4214 CPUs provided by the Data Science department of the Radboud University.

5.4.1 The effect of the naive sampling method

As mentioned in section 5.3.2, the phases are sampled with a logarithmic prior. This bias within the dataset could potentially introduce a bias into the sampling distribution of the normalizing flow model, reducing its possible performance. This leaves us with two options. We first note that the introduced bias could have beneficial effects. As long as the model still outputs a substantial range of phases, having a biased dataset towards smaller phases might result in a higher percentage of accepted and relevant sampled points since smaller CP-violating phases will introduce a smaller CP-violating eEDM contribution. Therefore, one option is to just learn normally and ignore the bias. The second option is to try to counter the prior in the learning process. We know that smaller phases have an exponentially higher probability of being sampled. In other words, the biased prior could be described as for a general phase ϕ :

$$p(\phi) \propto e^{-\phi}. \quad (5.13)$$

If we want to counter this biased prior, we have to take this prior into account for the likelihood of the target distribution, i.e. the loss. As the loss is a likelihood, we can use the ratio of the unbiased and the biased prior, to ‘re-balance’ the logarithmic distribution to a more unbiased prior, where an unbiased prior is a uniform distribution. The same prior is, independently, present for each sampled phase. This results in the following factor that needs to be added to the target distribution likelihood while learning, taking into account that we used this prior for each phase:

$$\frac{p_{\text{unbiased}}(\phi_1, \phi_2, \dots, \phi_7)}{p_{\text{biased}}(\phi_1, \phi_2, \dots, \phi_7)} = \prod_{i=1}^7 \frac{p_{\text{unbiased}}(\phi_i)}{p_{\text{biased}}(\phi_i)} = \prod_{i=1}^7 \frac{1}{e^{-\phi_i}} = \prod_{i=1}^7 e^{\phi_i} = e^{\sum_{i=1}^7 \phi_i}. \quad (5.14)$$

Both options have been tested using the validation methods reported in chapter 6. The results indicated that it is beneficial to ignore this introduced bias within the dataset. However, it remains something to keep in mind during possible future research or optimisation of the ML model and is therefore explained in the methodology.

5.5 The Inference Pipeline

Now the full pipeline of creating the dataset and learning the flow model has been introduced it is good to have an overview of the target usage of the model after it has been learned.

The idea is that the model replaces the currently used Gaussian Particle Filters in a more automated and efficient manner. Thus the model receives as input correct pMSSM points, containing 19 parameters as a condition. For this conditional the model then outputs a specified amount of six-dimensional phase combinations. Combining these six-dimensional phase vectors with the conditional(s) gives the required amount of cpMSSM points. These cpMSSM points are then fed to the calculation software, which reports a lot of predictions for observables originating from the given cpMSSM point. The predictions can then be used to either exclude parameter configurations or explore possible parameter effects.

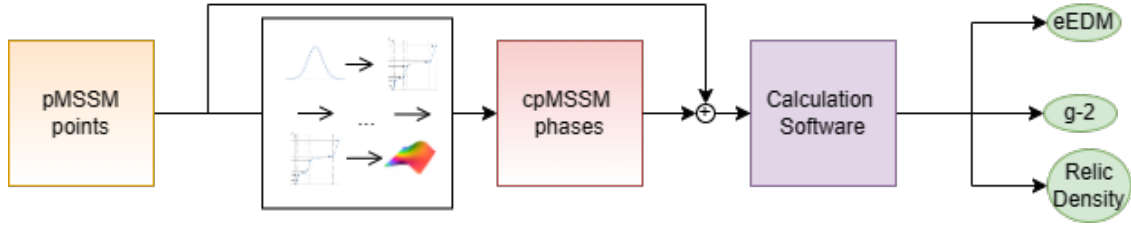


Figure 5.3: Visualization of the inference Pipeline using a learned conditional normalizing flow model.

Chapter 6

Model Validation

The previous chapter introduced the ML model that will be used to study the CP-violating effects of the dark matter relic density. In this chapter we will introduce and explain the methods used to validate the ML model, both during the learning phase and afterwards.

In a more conventional ML context the validation methods would consist of the validation loss and the validation accuracy. In other words, we would determine the value of the loss function and the accuracy on a separate part of the data not seen before by the model. However, in this case both of these metrics are not useful, as the loss function used in the case of a normalizing flow is the likelihood of the target distribution. This likelihood is not normalized, as a consequence we cannot compare the relative performance of different models using this metric. Furthermore, to determine the validation accuracy we require the calculation software, as this validation accuracy requires the eEDM prediction of the sampled cpMSSM points. The usage of the calculation software would be too time consuming. This section will discuss the used solutions to this problem.

6.1 Likelihood Ratio

First of all we have the most natural solution: the likelihood ratio (LR). As mentioned, the problem with the validation loss was that the used loss function is not normalized. However, this problem is solved by using a ratio of two likelihoods: a likelihood of the correct points over the likelihood of the incorrect points. These likelihoods share the same would-be normalization constant, the effect of which will drop out in the ratio. Explicitly, the used likelihood ratio is here defined as follows:

$$\text{LR} = \frac{\frac{1}{N_C} \sum_{i=1}^{N_C} \mathcal{L}_i}{\frac{1}{N_I} \sum_{i=1}^{N_I} \mathcal{L}_i}, \quad (6.1)$$

where N_C and N_I stand for the number of correct and incorrect data points respectively. Furthermore, \mathcal{L}_i denotes the likelihood (5.7) of a specific data point i . This likelihood can be determined by going backwards through the bijectors of the model, which is, in general terms, shown in 5.2.

Interpretation of this metric is not as straightforward as it seems. We cannot directly say that an LR of X means that the model is X times more likely to output eEDM adhering samples than not. However, we now can compare the found LR values over different models. Thus, models with a higher LR value can be considered better at all times during the learning process.

However, preliminary studies showed a hard-to-spot obstacle. Even though the LR values reported for preliminary models were extremely high (500+), when the samples were tested only 0.1% resulted in correct cpMSSM points. To understand why this happened two observations need to be made. The LR was calculated for a validation set consisting of 40.000 incorrect cpMSSM points and 50.000 correct ones, both

sampled randomly from the created dataset. Furthermore, we know that large phases, especially combinations of large phases, often result in a higher eEDM prediction, as the larger the non-absorbable phase(s), the bigger the CP violation. Thus, when plotting the correct phase vectors in a 2d scatter plot for two of the six phases, we would expect most of the correct samples to form a ‘cross’. In other words for most samples either one of the plotted phases is high, but not both at the same time. On the other hand, incorrect points can be much farther away from the axes in such a plot. Given that we randomly sample the incorrect points, we will get a lot of incorrect data points far away from the axes. Especially, since we only sample 40.000 incorrect points from a total of about 99 million. The preliminary models had learned that smaller phases were better, but seemed to have a preference for samples in a small circle around the origin within those 2d plots. The preliminary models most likely learned this because it is the easiest way to both optimise the target likelihood as well as get a high LR. The latter metric was used to select a learning configuration for these preliminary models, thus its value also (indirectly) influenced what the models learned. Because the large phases of the incorrect validation cpMSSM points are outside of this circle, while the correct validation points are in it, this does result in a high LR. However, if we then use this model for sampling, we still get a lot of points outside of the ‘cross’. Most of these samples are therefore still rejected by the calculation software. The situation described above is visualized in an aggravated and simplified manner in figure 6.1a.

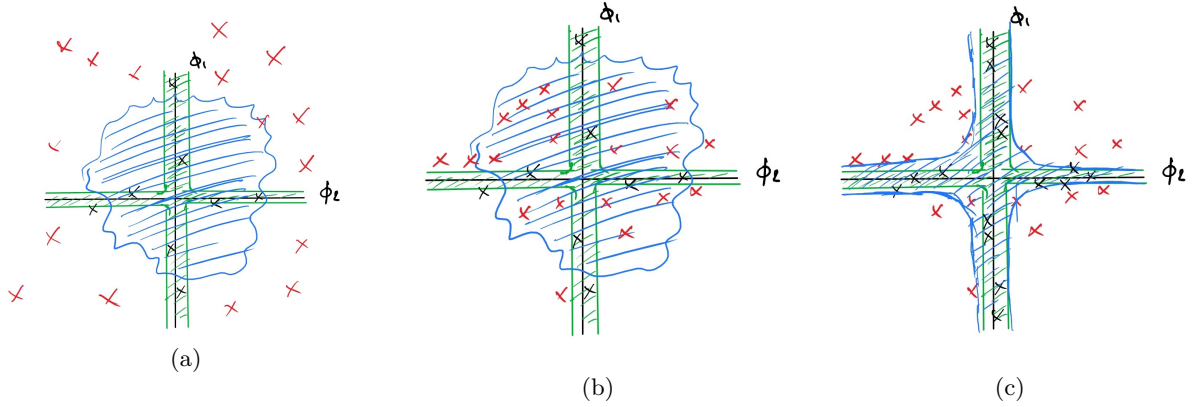


Figure 6.1: Simplified and aggravated visualizations of the LR obstacle encountered within preliminary studies. Red crosses represent incorrect phase combinations within the validation set, whereas black crosses represent the correct validation phase combinations. Note that the crosses are not the full validation set, in reality there might be incorrect points closer to the green area as well, this aggravation just shows the obstacle of the old LR better. Furthermore, the green area is the high-likelihood area of the target distribution, and the blue area is the high-likelihood area according to the ML model. (a): old LR calculation, preliminary model. (b): new LR calculation, preliminary model. (c): new LR calculation, final model.

This obstacle can be overcome by not using a random selection of incorrect cpMSSM points in the validation set. Instead of random sampling we opted to use a greedy algorithm aiming to select a set of incorrect points with the following condition:

$$\frac{1}{N_I} \sum_{i=1}^{N_I} \sum_{j=i}^6 |P_{i,j}| < 0.01, \quad (6.2)$$

where $j = 1, 2, \dots, 6$ and $P_i = (\phi_{M_1}, \phi_{M_2}, \phi_{A_t}, \phi_{A_b}, \phi_{A_\tau}, \phi_\mu)$ represents the phases of point i within the incorrect set of validation points. Further, the limit of 0.01 was found through trial and error by checking at which limit the preliminary, badly-sampling, models started to get a lower LR. Due to this different choice of incorrect validation points, we get a situation as visualized in figure 6.1b. In this situation a lot more of the incorrect validation points are close to the ‘cross’ of correct points, and therefore also within the high likelihood area of the preliminary model. Thus, the calculated LR in this scenario will be much lower, which better represents the fact that this model does not sample enough correct points.

For the model to start learning to also have a preference for this ‘cross’, and thus sample more correct points, the usage of augmentation (5.3.4) was beneficial. Through augmentation the black crosses in figure 6.1 are mirrored in both axes. Thus, the black crosses themselves in figure 6.1c show the ‘cross’ of the target distribution better. This leads to the learned model having a preference for the ‘cross’ as well for new samples. Also, as can be seen in figure 6.1c, this leads to a higher LR, as the correct points are in the blue area, where most of the incorrect points are not. Therefore, by using this new validation set a high LR better reflects what it was introduced for: a well-working model.

6.2 Other Methods: Model Characteristics

We now have a metric that implicitly tells us how well the model has learned, both during the learning process as well as afterwards. However, there are more characteristics of the model’s performance that we are interested in that are not covered by the LR. These characteristics come from the following remarks:

- To perform research on the cpMSSM we need a representative set of samples, i.e. we want unique samples following the target distribution, not copies.
- The MSSM itself does not present a preference for a certain parameter configuration; a point is either correct according to experimental observations/limits, or it is not.¹

6.2.1 Scatter Plots

To check how representative the samples are we make scatter plots of the sampled phases. For every combination of the six phases we make a 2d scatter plot of 500.000 samples for one, randomly chosen, pMSSM point. To complete the full figure for each individual phase a histogram is made.

Ideally, for the eEDM-dominant phases the crosses mentioned in the previous section would become visible. The eEDM-dominant phases are the phases that we assume contribute most to the one-loop eEDM diagrams: ϕ_{M_1} , ϕ_{M_2} and ϕ_μ . Furthermore, for all phases we can check if there are ‘islands of points’. This refers to samples being present in non-connecting patches. We want to make sure that this is not the case, as it can be assumed that this is not representative of the set of all correct phase combinations.

6.2.2 Volume Approximation

Scatter plots are nice to *see* how representative the set of samples of the model are. However, we would also like to quantify the representativeness. To do so we opted to go with an approximation of the volume sampled by the model. Naturally, the larger the volume that is sampled, the more representative that set of samples is assumed to be. It is good to remark that such an approximation does not take into account the possibility of ‘islands of points’. Therefore, it is good to combine this approximation with the scatter plots to both see and quantify the representativeness of the samples. In practice, the volume approximation and scatter plots thus also use the same 500.000 generated samples.

To approximate the volume of the samples we use a direct Monte Carlo method [54]. We create 25.000 6-dimensional probing spheres with a randomly chosen radius smaller than $\frac{\pi}{2}$. For these probing spheres the volume is easily calculated. Subsequently, we determine the ratio of samples inside and outside this probing sphere. We denote the probing volume V_p and the to-be-approximated volume of samples as V_s and use:

$$\frac{V_p}{V_s} = \frac{N_{\text{in}}}{N_{\text{out}} + N_{\text{in}}}, \quad (6.3)$$

to determine V_s according to that probing sphere. Here N_{in} and N_{out} are the number of samples inside and outside the probing sphere respectively. To stabilise the approximation we take the mean of the 25.000 approximations calculated.

¹Some physicists would argue that points with lower finetuning would be preferred. However, not all agree and this thesis steers clear of that discussion.

6.2.3 Uniformity Plots

As a last newly-defined validation method we want to check if the model has a preference for certain samples. Such a check is needed, because, as mentioned, physics does not have a preference for one correct parameter configuration over another correct one. Physics-wise, a point is either correct according to experimental limits/observables, or incorrect. There is no in-between gradient of correctness. To check if the model follows a same reasoning or does have a ‘preference of correctness’, we introduce uniformity plots. These plots again consist of 2d plots for all combinations of the six phases. Each of these 2d plots is then filled with a grid of points, which are colour-coded corresponding with the likelihood according to the normalizing flow. Of course, the model needs a six-dimensional point and not a two-dimensional one, therefore, the phase combination is completed by all zeros for the non-included phases of that plot. Furthermore, the colour represents a value that is normalized over all present values in the figure, to take into account that the likelihood itself is not normalized. If the model is perfect these plots would show evenly-coloured shapes, representing the correct phase-space areas according to the eEDM limit.

6.3 Acceptance Percentage

Of course, despite its time consumption, we still check the percentage of correct samples using the calculation software. This method is not feasible to be used for each data iteration during the learning process, however for a learned model this is not the case. Therefore, this validation accuracy metric will be used as the ultimate performance metric of the model, and can also be used to compare its effectiveness with previous methods like the Gaussian particle filter.

6.4 Results

This section presents the validation results of the ML model, both for a model corrected for the introduced bias (5.4.1) as well as a ‘conventionally’ learned model. The configuration of both models is given in 5.4. These results will show that the model has an acceptable level of performance and is a sufficient model for the study of CP-violating effects on the dark matter relic density in chapter 7.

6.4.1 Likelihood Ratio

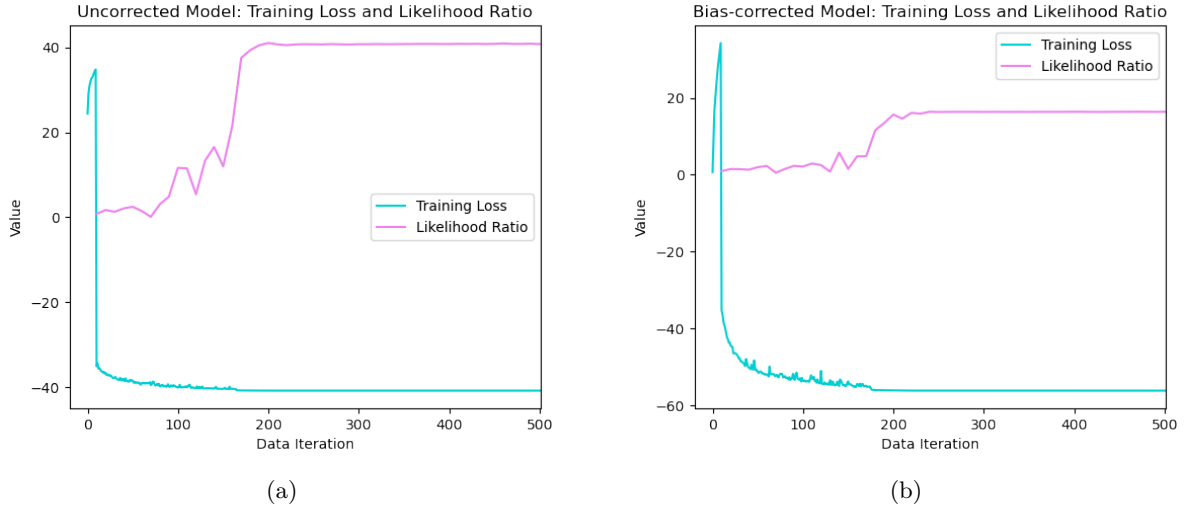


Figure 6.2: Plots of the (non-normalized) loss value and likelihood ratio of the uncorrected model (a) and the bias-corrected model (b) over the data iterations.

Figure 6.2b shows the (non-normalized) loss values during the learning process, as well as the likelihood ratio. The loss is determined on the training data, where the likelihood ratio is determined on a validation set as explained in section 6.1. First of all, we can notice that in general both models seem to have converged towards some optimum. Furthermore, both models seem to follow quite similar stages: first the model makes big but wrong decisions, as can be seen by the loss value climbing, where we want it to decline.² Afterwards both models improve quite radically in their loss value. However the likelihood ratio does not show corresponding behaviour. After about 40 iterations until about 200 the models seem to progress with more fine-grained improvements, as shown by the instability of the loss value. These improvements have a very big effect on the likelihood ratio. This seems to suggest that, after the initial big mistakes, the models first learn the limits of the phases due to the eEDM. These models would then report findings similar to those explained for the preliminary models in section 6.1, i.e. a circle of samples around the origin. It is after this stage that the models seem to learn the crosses, i.e. the complex relations between the phases present in the training data. Due to the way the LR is determined, only these improvements are reflected in the LR value, as desired. The last stage, after about 200 iterations, shows almost perfect convergence, i.e. the optimum reached at this point is no longer improved, at least according to these metrics.

If we compare the relative performance of the two models we see that the uncorrected model reaches both a lower value for the training loss and a higher likelihood ratio. Given that the loss value is non-normalized, it is more fair to compare the difference between the end and start values than the absolute values. However, the starting values (± 20) in this comparison are quite similar and thus this difference is also substantially higher for the uncorrected model. This preference of these metrics for the uncorrected model is not surprising: the uncorrected model does not get penalized for preferring smaller phases. We know that smaller phases result in smaller eEDM contributions, as the non-absorbable phases are what introduce CP violations and thus eEDM contributions. As such, the dataset will also contain a lot of smaller phase combinations. By making it easier to prefer smaller phases for the uncorrected model it is easier to get a smaller loss, as that does reflect the training data. The likelihood ratio has been modified to somewhat counter the possibility of only outputting very small phases, and not incorporating the relationships between the phases, i.e. to not learn the ‘crosses’. However, we had to set a limit on how selective we are for the validation set (6.2), thus if the model goes even smaller than the set limit, the LR will still go up without learning the complex relationships. Although the observed stages of learning mentioned above do not imply this to happen, it is always a possibility.

6.4.2 Scatter Plots

To determine whether any of the models have converged towards an optimum that reflects something of a relationship between the phases, we can have a look at our visual validations. In figure 6.3 the scatter plot of the uncorrected model is given. The scatter plots of the bias-corrected models are given in the appendix (figure B.1).

²Note that the loss function used is actually the negative of the likelihood of the target distribution. This is the case because we use a procedure called gradient descent, not ascent. Of course, this minimises, not maximises, a function.

2d Scatter plots of 500.000 samples: uncorrected normalizing flow
pMSSM point:

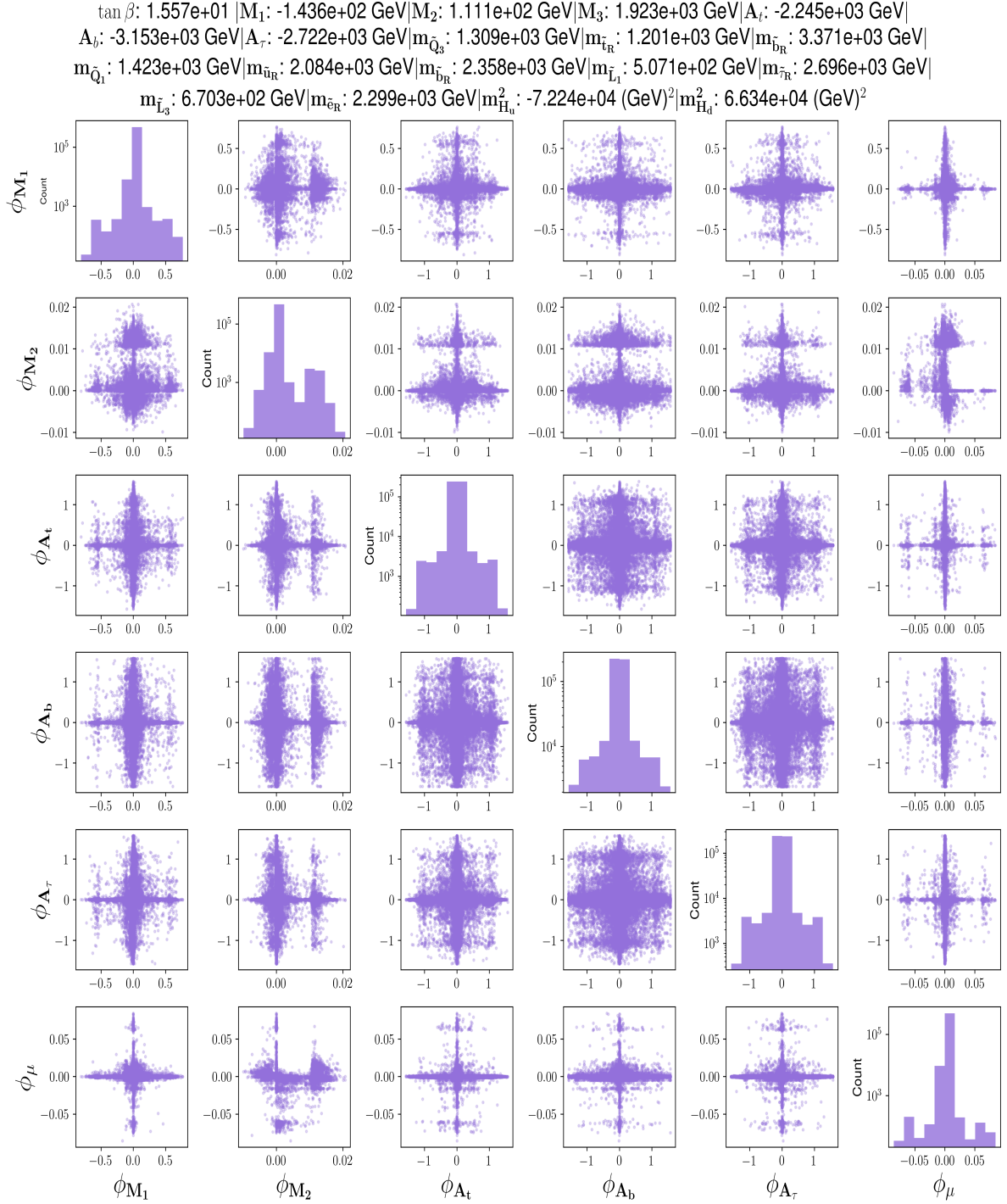


Figure 6.3: Scatter plots for each 2-dimensional combination of phases sampled by the uncorrected normalizing flow. On the ‘diagonal’ are logarithmically scaled histograms of the range of each phase. The model used for this figure was learned for 501 data iterations.

Firstly, in figure 6.3 it is clear that the model has learned to output more than only copies of cpMSSM points. Secondly, we do not see the emergence of ‘islands of points’, which were explained in section 6.2.1. There are no multiple, fully-disconnected, patches present within the scatter plots. The model does, of course, still have regions of preference. However, these regions do not seem ‘over-fitted’ towards some combination, as most phases are sampled all over within the allowed range and shapes. Further, we note the emergence of ‘crosses’ for some of the phase combinations, especially for those containing ϕ_μ . This seems to suggest that the rising LR values reported are actually because of learned relationships, and not just because of the model preferring smaller phases. In addition, we see that the model seems to have made a distinction, based on limiting the range of phases, for dominant and non-dominant phases. The 3×3 grid of the phases of the trilinear couplings are observed to reach much higher values than the phases of the gauginos mass terms and μ . This corresponds with the distinction between one-loop and two-loop contributing parameters in section 4.2. In figure 6.3 we can also see that the model does seem to have a preference for positive values of ϕ_{M_2} , we will get back to this in section 6.4.3.

Additionally, it should be noted that the model does not seem to generate very different samples for different conditions. This cannot be seen in this plot, but is seen in the comparison with figure B.3, which shows the scatter plots for the uncorrected model generated for a different correct pMSSM point. Of course, there are some small differences present, however in general the same structures are seen for the generated samples. These same structures are also seen for most other pMSSM points. This potentially shows that the model could be optimised more, to introduce a more conditionalized sampler.

Further, we note that the bias-corrected model (figure B.1) has a clearly larger range of sampled points. This is especially notable for ϕ_{M_1} where the possible range of phase values doubles compared to the uncorrected model. In addition, we see that the ‘ 3×3 ’ grid of the trilinear couplings becomes much more filled. All of this is not surprising, as the bias-corrected model is pushed to output larger phases, and this validation method thus shows this to happen as desired.

A small remark regarding the limits on the phases of the trilinear couplings needs to be made. A small number of phases sampled by the normalizing flow goes beyond the range of $|\frac{\pi}{2}|$. This is due to the implementation of the normalizing flow. The limits in a normalizing flow are set slightly non-rigid,³ meaning that due to small floating point errors, that accumulate over the seven bijectors, a small number of samples have values outside of the set limit. Of course, this practically only happens when the samples are not restricted in range by the data, as is the case for the non-trilinear phases, shown in figure 6.3. We opted to set these anomalous values to the limit of the range, being $\pm\frac{\pi}{2}$, as that is what the normalizing flow ‘wanted’ to output.

6.4.3 Uniformity Plots

The next thing to validate is whether the model seems to have a preference within the set of correct points. As explained in section 6.2.3, the cpMSSM itself does not have such a preference. Thus, if a model is learned to perfection, the model should also not have such a preference.

³i.e. smaller than needed to cover floating-point errors. However this is done to preserve the numeric differentiability on the limits.

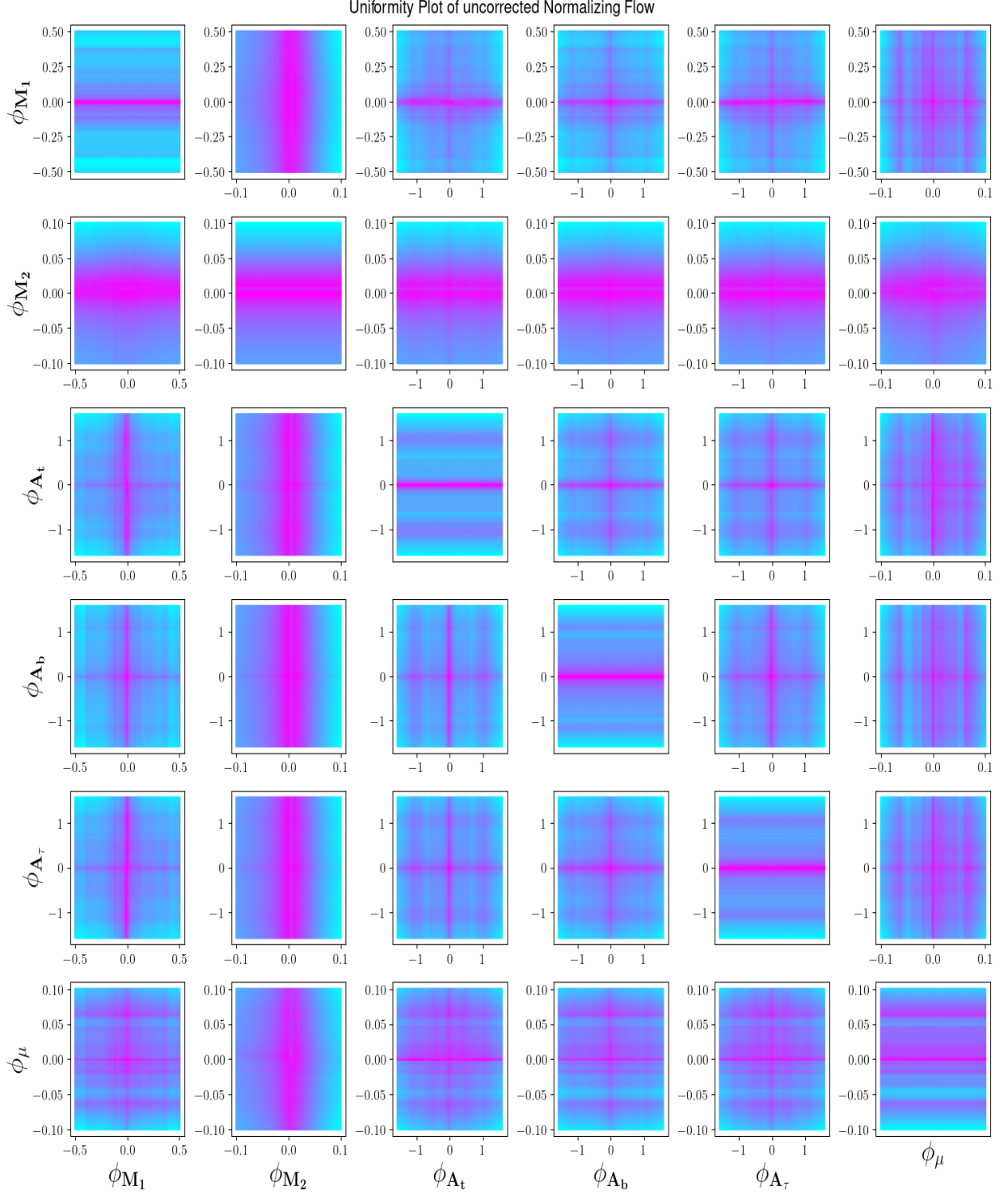


Figure 6.4: Uniformity plots for each 2-dimensional combination of phases, where the colour represents the relative likelihood (pink means higher, blue means lower) for each phase combination using the two non-zero values depicted within the grid. On the ‘diagonal’ there is only one non-zero value for the associated phase. The model used to determine the likelihood values was learned for 501 iterations over the data. The pMSSM point used to calculate these likelihoods is the same as the pMSSM point used for the scatter plots.

Figure 6.4 shows the uniformity plots for the uncorrected model. For the first remarks we ignore all combinations that include ϕ_{M_2} , as all combinations with that phase have clearly different behaviour. For all other combinations there seem to be three regions in terms of preference. Almost all combinations have the ‘cross’ as the highest preference region. Within this cross no significant preference is given to different points. Additionally, there is a background region, mostly forming a grid, therefore this region will be called the grid for clarity. This grid is less preferred compared to the ‘cross’, but also within the grid in general no internal preference is seen. This is, however, not the case for ϕ_μ , which does seem to have a higher preference for positive values compared to negative phase values. Why this is the case is not directly clear, but most likely it has something to do with the biases of the dataset. These biases could be the logarithmic bias introduced in the sampling procedure. However, it could also be a small mishap in the dataset creation that led to only positive μ parameters being present. For more on the latter, the reader is referred to the outlook of this thesis in chapter 8. The cause of the ϕ_μ preference being the μ bias in the dataset is supported by the results of the bias-corrected model. This model shows a bigger preference for positive ϕ_μ values compared to the uncorrected model, as seen in figure B.2. This could correspond with the implementation of the bias correction, which should urge the model to disregard the sampling bias, and thus also show other (accidental) biases more clearly. In addition, we note that the shape and brightness of the grid are quite different for different combinations. The last region seen in figure 6.4 is the region filling the inside of the grid, which we call the filling. Given the shading observed in the filling, some preference is present here. Outside of the regions everything seems to be low-likelihood.

Overall, this indicates that the model is not perfect. However, the model is not bad either as within the three regions the likelihood is quite stable. The relative preference difference between the three regions might also be due to the dataset presented to the model, which we cannot assume to be perfect as due to the usage of logarithmic sampling more lower-valued phases are present. Thus the model will learn that there is a higher likelihood for phases within the ‘cross’, resulting in this region becoming more bright in figure 6.4. In fact a point with higher values for the phases, as long as it is correct, should have the same likelihood. If we compare this to figure B.2, which shows these plots for the model that is corrected for this bias, we do indeed see that the brightness of the cross and the grid becomes more equal. This is especially the case for combinations of the phases of the trilinear couplings.

Why the grid itself emerges is somewhat of an open question. It might be due to how the plots are made. The model has learned to work with combinations of all phases, not with combinations of only two, thus the model might have learned that only certain specific ranges can work together. However, it could also be due to the representativeness of the dataset. Since fewer data points are present in the high-value phase regions it might be that there are actually more correct points in what we now call the filling, but these number of points are not present in the dataset. This results in the model assuming a low-likelihood for the filling, even if it should contain correct points according to physics. Lastly, however unlikely, the forming of a grid of points could also be true-to-nature.

For all plots that represent ϕ_{M_2} we see truly different behaviour. This points to any effect of ϕ_{M_2} being dominant over all other phase-effects. Apparently, if ϕ_{M_2} is considered the model has an extreme preference for points that have that phase as either zero, or points in a band around a small positive value. This last band is easier seen in figure 6.3, however it is also present in figure 6.4. There seems to be no preference for either the zero or positive band, as seen by the even colour of those bands. Outside of the bands the negative side has a slightly higher preference, with a quite smooth gradient. However, the relative colour of this region seems to indicate that not many, if any, points from this region are considered correct by the model. Why this different behaviour of ϕ_{M_2} emerges is again hard to explain, and most likely (again) stems from a possible bias in the dataset.

6.4.4 Volume Approximation

To try to quantify the representativeness of the generated samples we turn to the volume approximations of the samples, as introduced in 6.2.2.

Table 6.1: Table of volume approximations for the uncorrected model at different points within the learning process, for four different pMSSM points as given input of the normalizing flow. Note that these volumes are determined based on the original seven phases (including ϕ_{M_3}), thus we compare this volume with a total volume of around 111.5: a 7-dimensional sphere with radius $\frac{\pi}{2}$

Data Iteration	Point 1	Point 2	Point 3	Point 4
1	75.931	73.867	77.995	67.008
251	49.271	52.695	47.005	44.342
501	47.967	50.368	50.778	45.484

Table 6.2: Table of volume approximations for the bias-corrected model at different points within the learning process, for four different pMSSM points as given input of the normalizing flow. Note that these volumes are determined based on the original seven phases (including ϕ_{M_3}), thus we compare this volume with a total volume of around 111.5: a 7-dimensional sphere with radius $\frac{\pi}{2}$

Data Iteration	Point 1	Point 2	Point 3	Point 4
1	64.755	74.755	64.409	72.751
251	47.219	40.777	53.966	50.137
501	50.359	45.310	54.965	47.235

Table 6.1 and 6.2 show the volumes of the sample space for four pMSSM points that are not within the training data. The general pattern seems to be a starting volume around high 60 to high 70, and stabilizing around high 40 to low 50 after less than 250 data iterations. We have to compare these values with the total possible space of the samples. These approximations were made before we decided to rotate away ϕ_{M_3} (using the $U(1)_A$ and $U(1)_B$ rotations of section 3.5) due to mistakes in the not-to-be-touched, open domain SpHeno-CPV package in the calculation software (see C). Therefore we compare these values with the volume of a 7-dimensional sphere with radius $\frac{\pi}{2}$, which is approximately 111.5. Thus, these results show that a substantial part of the phase space is sampled. This is even more the case when considering the curse of dimensionality: most of the volume in higher dimensional spaces is in the edge of that volume. The phases in those edges would be the large phases, and we know that these mostly result in too high eEDM predictions. Thus, correct points are naturally located in a smaller volume, especially in a high-dimensional space. We cannot directly conclude that the sampled volume also consists of correct points, as for that the acceptance percentage would be needed. But it does at least suggest that points are sampled in quite a large and representative volume.

6.4.5 Acceptance Percentages

The last and best validation method is that of the acceptance percentage. During the learning process, the model is saved after one data iteration and every 250 iterations after. Further, the model that reports the highest likelihood ratio during the whole learning process is also saved. The percentages of correct points of 10.000 samples are tested for these models, and presented in table 6.3 for both the uncorrected and bias-corrected model.

Table 6.3: Percentage of correct cpMSSM samples, out of 10.000, at three points during the learning process: after 1, 251 and 501 data iterations for both the uncorrected and bias-corrected model. The acceptance percentage is also shown for the model that reported the highest likelihood ratio during the learning process. The samples were generated for correct pMSSM points not included within the training or the validation set.

Model	Acceptance Percentage (uncorrected)	Acceptance Percentage (bias-corrected)
1 iteration	0.2 %	0.9 %
251 iterations	55.5 %	28.6 %
501 iterations	67.2 %	39.4 %
Highest LR	50.3 %	38.9 %

The table shows that early on in the learning process the models unsurprisingly sample a large number of incorrect samples. After 250 data iterations both models have been able to learn to sample more correct samples. Between 250 and 500 iterations the training loss and likelihood ratios in figure 6.2 do not show progress. In contrast, the acceptance percentage does still rise substantially. This seems to point to the fact that the ultimate acceptance of samples is very sensitive to small perturbations in the samples. Perturbations that do not really manifest themselves within the metrics of training loss and likelihood ratio. We further note that for both models the model reporting the highest likelihood ratio does not have the highest percentage of accepted samples. Together with the discrepancy between progress in the 250-500 iterations regime, this points to the fact that the likelihood ratio is not a perfect validation method.

When we compare the uncorrected and bias-corrected models we see that the uncorrected model performs substantially better. Again, given that the bias-corrected model is penalized for small phases, this is not surprising. Figure 6.5 shows a plot of the acceptance percentage at different eEDM limits of both the uncorrected and the bias-corrected models.

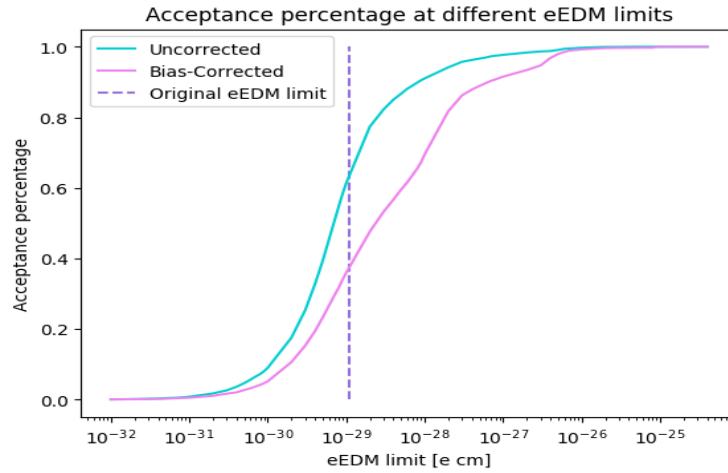


Figure 6.5: Acceptance percentage (y-axis) if a different eEDM limit was set (x-axis) for both the uncorrected and bias-corrected model. The vertical dashed line represents the eEDM upper limit (4.11) as used for the training data in this thesis.

Firstly, figure 6.5 shows that the uncorrected model also has a lot of generated samples near the current eEDM limit. In other words, this again confirms that the uncorrected model is not outputting only small phases. This supports a choice to go with the uncorrected model for the study of chapter 7, as the bias within the training data does not seem to manifest itself in the model's samples in an undesired manner. Furthermore, this figure shows that the models should have the capability to also work for the more strict, current eEDM limit (4.10). Especially if the training data of the model were to be made with the new eEDM limit in mind.

In general, the acceptance percentages presented in this section are deemed sufficient to use the new sampler in the next chapter. Note that a perfect performance was never required, as the generated samples still need to go through the calculation software to determine the associated predictions (see section 5.5). Therefore, we still have the option to filter out the incorrect samples. By having >50% correct samples from an automatic process, the usage of the calculation software has become extremely more efficient and effective already. Given the better performance and the fact that the bias is not fully represented in the model's samples according to the defined validation methods, for chapter 7 the choice is made to use the uncorrected model.

Chapter 7

Study: CP violation effects on the Relic Density

This chapter presents a study into the effects of the CP-violating phases of the cpMSSM on the dark matter relic density. The study will be performed for multiple categories, where the categories are determined by the dominant process during the freeze-out process. For more background regarding the relic density, the reader is referred to section 4.2. The categories are presented in section 4.2 as well.

Before going into the categories, we explain the general procedure used to study the CP-violating effects on the dark matter relic density. On the original, checked, pMSSM dataset we use both quantifiable methods and visual methods to determine into which categories pMSSM points fall. The quantifiable methods are a result of the calculation software (see Appendix C). The visual methods rely on plotting output parameter values in specific ways to recognize the category if possible. Then, for each category five pMSSM points are randomly sampled,¹ if possible in the desired range of relic density values, which is given in section 4.2 as:

$$0.09 < \Omega h^2 < 0.15. \quad (7.1)$$

For these five pMSSM points the normalizing flow model is then used to generate 20.000 cpMSSM samples. These samples are then fed to the calculation software to determine their relic density prediction. By using scatter plots, the effects of the phases are then checked for all five points. If a general effect is found, we try to explain this effect using the relevant (cp)MSSM couplings of that category, or, if necessary, other relevant theory of the cpMSSM. Furthermore, we also look at what the restriction of the eEDM implies for these effects.

7.1 H_1 -funnel

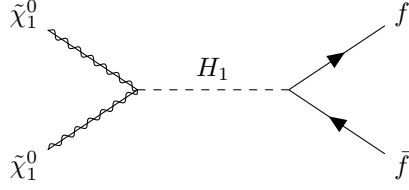
The first category of points to look at is that of the so-called Higgs funnel. Due to the existence of two Higgs doublets, this funnel (mainly) comes in two forms: either a near-resonant H_1 features as the s-channel propagator, or a near-resonant H_2 does.² This section will look at the first option. We further note that we describe this funnel using the CP-violating mass eigenstate H_1 , as we are discussing cpMSSM points within this study, even though the category is selected for pMSSM points, which uses h^0 . Given that most pMSSM points used are within the decoupled regime, the lightest eigenstate will act very similar to the SM Higgs boson, as would have also been the case for h^0 .

The pMSSM points considered in this section should have the following process as the dominant annihilation

¹If five pMSSM points are present.

²Technically, there could be a third funnel with H_3 . However, this requires phenomenologically, uninterestingly high sparticle masses and is thus ignored in this thesis.

lation process during freeze-out:



where f denotes an arbitrary fermion.

To select the correct pMSSM points we have two tools at our disposal. Firstly we look at the resonance point of this diagram: $m_{\tilde{\chi}_1^0} = \frac{m_{H_1}}{2} \pm 5\text{GeV}$. The bandwidth is taken because if the resonance is too perfect, the relic density might become too low, as the process becomes too efficient leaving too few DM particles. However, figure 7.1 shows that this selection is not sufficient. In this figure the relic density of pMSSM points is plotted against the ratio of the mass of the LSP and the mass of the SM-like Higgs boson.

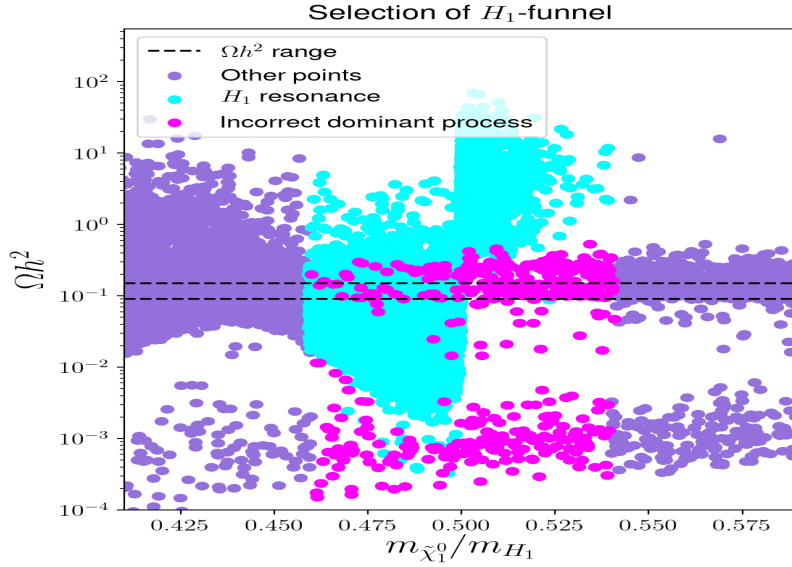


Figure 7.1: Scatter plot of pMSSM points that are of interest for the selection of H_1 -funnel points.

The calculation software provides us with the ordered set of three most dominant processes for the relic density. Figure 7.1 shows us that if we only select on the mass we would also select points that actually have another most dominant DM (co)-annihilation process.³ On the other hand, if we were to only select on the process, this would also contain points quite far away from the resonance, possibly limiting any effect that CP-violating phases could have on the relic density. Therefore the points selected as being in the H_1 -funnel are points both within the specified bandwidth of resonance, and reporting the desired dominant DM annihilation process through the calculation software.

The next step is to use the ML sampler to study the effects of the CP-violating phases on the relic density. The main effect observed is not truly related to the funnel these points are in: *the selection on $eEDM$ removes most CP-violating phase-induced effects.*

³In this case most likely a co-annihilation with the lightest chargino.

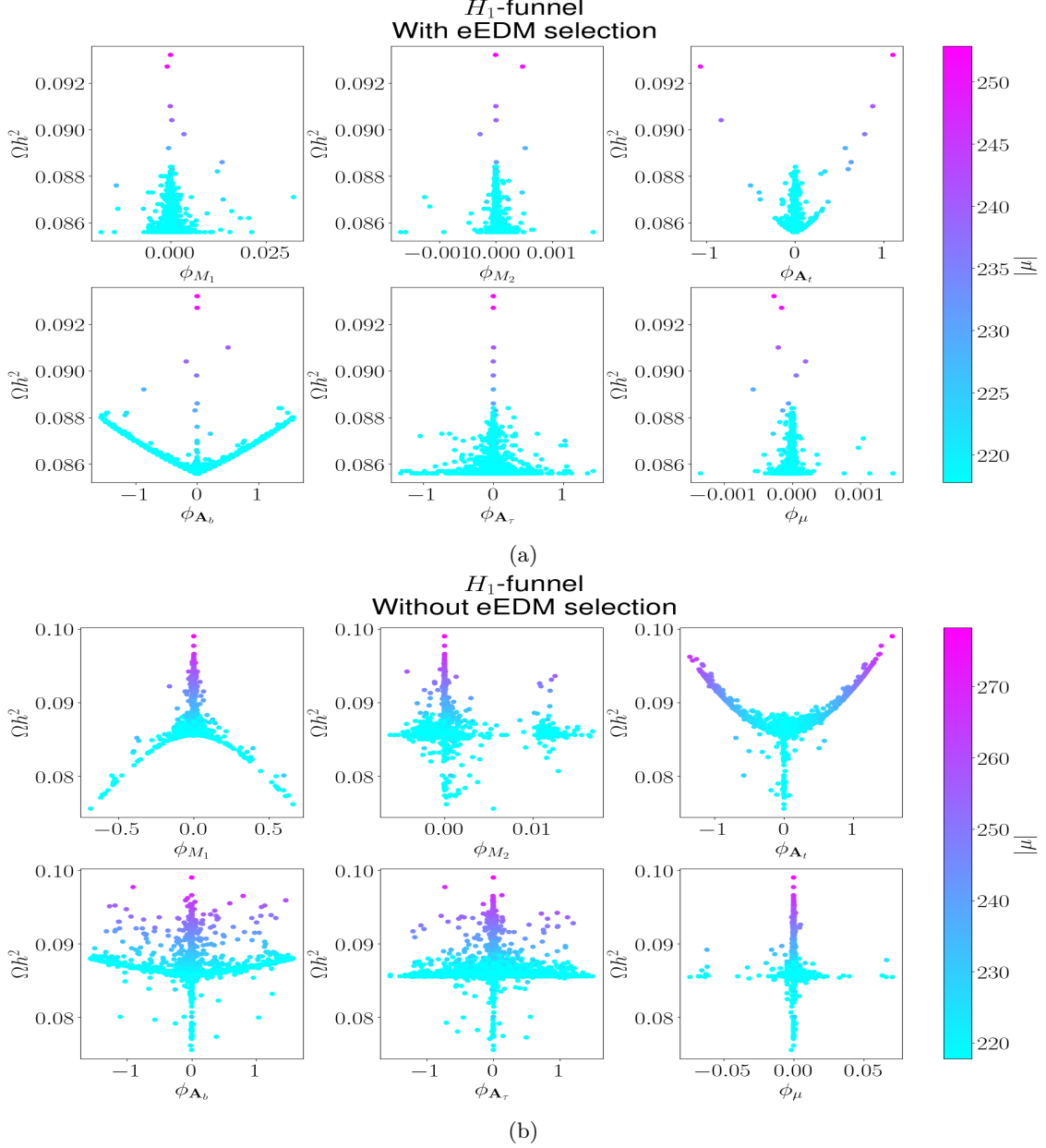


Figure 7.2: Scatter plots of phase values versus the dark matter relic density of cpMSSM points. The phase values were sampled for a pMSSM point originating in the H_1 -funnel. The colour represents $|\mu|$, which is not a free parameter of the software but is calculated via the tadpole equations (3.56). (a): with selection on the eEDM limit. (b): without selection on the eEDM limit.

Figure 7.2 shows (one of) the made scatter plots for the H_1 -funnel, both with and without imposing the eEDM limit. In general for all five pMSSM points, effects are seen for the phases of M_1 , \mathbf{A}_t and \mathbf{A}_b . For ϕ_{M_1} the effect is fully removed when imposing the eEDM limit. The effect of $\phi_{\mathbf{A}_t}$ is mostly removed by the eEDM limit, however the remaining presence of some points at larger $\phi_{\mathbf{A}_t}$ indicates that if enough samples are generated this effect could remain. For now, effects that only emerge for very large amounts of samples are disregarded, as they only present themselves for very specific combinations of phases, and we are more interested in ‘general’ effects. Lastly, the effect of $\phi_{\mathbf{A}_b}$ remains after imposing the eEDM limit, however this is also the smallest effect to begin with.

The *effect of ϕ_{M_1}* can be explained by the influence of M_1 on the LSP, as M_1 changes the composition of the LSP. Given that the interactions, and their loop corrections, are determined by the gauge eigenstates and not the mass eigenstates, this composition has a strong effect on the efficiency of the funnel process. Moreover, the effect of ϕ_{M_1} is seen in the coupling of the neutralino with the SM-like Higgs, which is given in equation A.16. We note that this coupling is for the CP-conserving state, and because we are discussing cpMSSM points we should be looking at the CP-violating mass states. However, that coupling would become unnecessarily complex, while the importance of the coupling can also be seen in the CP-conserving version, since we can see the coupling directly depends on (complex conjugates) of the entries of the neutralino mixing matrix. Because these expressions do not merely involve absolute values, the phase of M_1 has a direct influence on this coupling, even at tree level. Further, we know that changing from CP conserving to CP violating states does not introduce extra entries of the neutralino mixing matrix, as these are not present in the required \mathcal{O} matrix for this change. Thus, the entries of the neutralino mixing matrix present in the coupling, will also *not* emerge as absolute values in the CP-violating coupling. Therefore, ϕ_{M_1} has a direct effect on the relic density, as it influences the coupling of the most dominant process.

The *effect of ϕ_{A_t}* seen in figure 7.2 is one of the more important relic density effects seen in this thesis. It can be seen that higher values of this phase correspond to higher values of $|\mu|$, and we know $|\mu|$ has a direct effect on the coupling of the Higgs boson to the LSP through the LSP composition, and thus on the efficiency of the DM annihilation process. Thus a change in ϕ_{A_t} affects that efficiency as well. We argue that ϕ_{A_t} influences $|\mu|$ via the tadpole equations (3.56), with this phase coming into play in the explicitly mentioned loop corrections of those equations. These loop corrections are determined by the higher order corrections of Higgs interactions with the top quark and the stop squark. The latter coupling is influenced by A_t , as shown in A.4, which leads to the influence of ϕ_{A_t} . One could now question why ϕ_μ does not have a similar influence on $|\mu|$ through loop corrections. However, this phase is not directly present in the tadpole equations. Additionally, and more importantly, this phase gets introduced in propagator terms regarding the Higgs doublets, which are less dominant in the loop corrections as the top and stop quark couplings. This effect of ϕ_{A_t} on $|\mu|$ comes back in most categories and is one of the main CP-violating effects seen on the relic density.

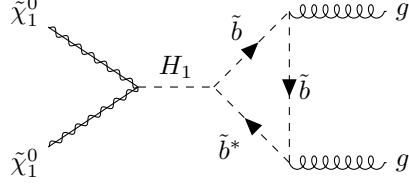
The question remains as to why the effect of ϕ_{A_t} is that large, given that it enters through loop corrections. Usually, loop corrections, and thus their associated effects, are suppressed. We argue that the larger effect in the case of ϕ_{A_t} possibly might be due to the order of magnitudes in the tadpole equations. Our calculation software uses the following relation, which represents the tadpole equations, to set $|\mu|$:

$$\frac{M_Z}{2} = \frac{m_{H_d}^2 + \Sigma_d^d - (m_{H_u}^2 + \Sigma_u^u) \tan^2 \beta}{\tan^2 \beta - 1} - |\mu|^2. \quad (7.2)$$

In this equation Σ_d^d and Σ_u^u represent the loop corrections of up- and down-type respectively. The latter of those is where ϕ_{A_t} plays a role. The idea is that we know M_z is of the order of magnitude of 100 GeV as is $\tan^2 \beta$. Where $m_{H_d}^2$ and $m_{H_u}^2$ are mostly of a much higher order of magnitudes. The calculation software sets $|\mu|$ such that the RHS of equation 7.2 becomes equal to the known value of the LHS. Given that $|\mu|$ is, usually, also of a lower order of magnitude than $m_{H_d}^2$ and $m_{H_u}^2$, we need the loop corrections (Σ_d^d and Σ_u^u) to predominantly cancel $m_{H_d}^2$ and $m_{H_u}^2$. In other words, the loop corrections need to be of the same (high) order of magnitude as $m_{H_d}^2$ and $m_{H_u}^2$. Then, even if ϕ_{A_t} only manages to realise a relatively small change of the loop correction, this will lead to the much smaller $|\mu|$ having to change substantially more, relative to its original value, to cancel that change. The exact difference needed for $|\mu|$ is of course dependent on the specifics of (the parameters of) the pMSSM point. Therefore the change needed of $|\mu|$ can differ over different pMSSM points, as will be seen in the scatter plots of this chapter. Further, this thesis has not performed much exploration to confirm this idea. Therefore, we encourage future research to better look into the size of the effect of ϕ_{A_t} .

The last effect of the H_1 -funnel is that of ϕ_{A_b} . We argue that this effect might come from loop corrections at the ‘SM-end’ of the dominant process. Most of the cpMSSM points in this category have a most dominant DM annihilation process with two gluons as end product. This is not surprising as the indirect coupling of the SM-like Higgs boson with two gluons is strong, shown by the fact that exactly this process

was the backbone of the first Higgs observation [2]. The following diagram contributes to that most dominant DM annihilation process.



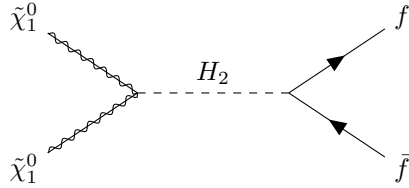
This diagram is enhanced by the coupling of $H_1 - \tilde{b} - \tilde{b}^*$, as given in A.4.⁴ This enhancement relates to the $\frac{1}{\cos \beta}$ in $y_b = \frac{gm_b}{\sqrt{2}M_W \cos \beta}$ present in this coupling, where $\frac{1}{\cos \beta}$ is large for our pMSSM points. Most pMSSM points are in the decoupling limit, in other words $\tan \beta$ is large.⁵ In this coupling also A_b is present, thus leading to the observed effects from ϕ_{A_b} , which is not as big as the other two effects as it emerges in a loop correction of the most dominant DM annihilation process.

This explanation does require a further explanation as to why we do not contribute a similar effect to ϕ_{A_t} , as one could question why a similar diagram using a stop loop is not discussed. First of all, the $H_1 - \tilde{t} - \tilde{t}^*$ does *not* involve A_t terms. Therefore, such a diagram does not introduce ϕ_{A_t} effects. However, that coupling does depend on μ , but any effects on μ are suppressed by two characteristics of the pMSSM point. Firstly, we have the $\frac{1}{\sin \beta}$ in $y_t = \frac{gm_t}{\sqrt{2}M_W \sin \beta}$ that is present in this coupling. Secondly, μ itself is much smaller than A_t or A_b . These characteristics combined with this being a one-loop order diagram to begin with, suppresses any ϕ_μ effect.

Even though the effect of ϕ_{A_b} is the smallest of three phase effects, it is the only effect to really survive the eEDM limit. Most likely ϕ_{A_b} is allowed to have higher values because the up and down squarks feature in the Barr-Zee diagrams through a coupling with (all) the Higgs bosons. As mentioned, these couplings are determined strongly by Yukawa terms, and are the highest for the third generation up-type (s)quarks, resulting in a smaller eEDM contribution from the (phases of the) down-type squarks. Thus, although the effect of ϕ_{A_b} is the smallest, it is the only effect present in the most ‘true-to-experiment’ situation.

7.2 H_2 -funnel

The next category of points to look at is very similar to the previous one, only in this case the near-resonant Higgs particle featuring in an s-channel propagator is the second heaviest neutral Higgs boson H_2 . Thus, we have the following, very similar process:



where again f denotes an arbitrary fermion.

The problem for this category is that we do not have any pMSSM points within the original dataset that have this process as the most dominant DM annihilation process, or fall within the mass range of $M_{\tilde{\chi}_1^0} = \frac{m_{H_2}}{2} \pm 5$ GeV. Therefore, instead of selecting these pMSSM points, we created them. For this we first select pMSSM points with $M_1 \ll M_2 \ll \mu$, in this way we select points with a very bino-like LSP (see table 3.3). The mass of the LSP for these points is mostly determined by the M_1 parameter. If we then

⁴Where, for simplicity we associate the matrix with ϕ_1 as mostly contributing to H_1 etc..

⁵All points have a $\tan \beta$ higher than 10.

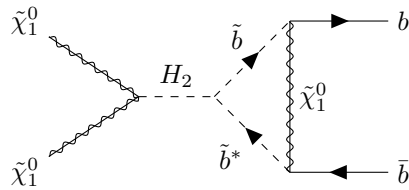
also filter these points such that $\mu \gg m_{H_2}$ this gives us the possibility to set M_1 around $\frac{m_{H_2}}{2}$, while keeping intact the hierarchy of parameters, such that phenomenologically the pMSSM point does not change too much with regards to neutralino/chargino composition. In other words, we create points that should be close to the required resonance. In addition, by only creating higher mass points we should not get closer to experimental limits for the sparticles, as these are mostly lower limits (C.3). We succeeded in creating 47 points that both had a correct relic density range, as well as had the H_2 -funnel process as their dominant process. However, these points had LSP masses in the range of $\frac{m_{H_2}}{2} \pm 20$ GeV.

Figure 7.3 shows the most clear general effects seen within this category. First of all we again see the restrictive effects of the eEDM selection. However, in this case the effect of ϕ_{A_b} is the strongest, thus the strongest effect remains after eEDM selection. This differs from the H_1 -funnel, where the strongest effects were from ϕ_{A_t} and thus were removed by imposing the eEDM limit.

The second thing to note is that all effects present in the H_1 -funnel are also present in the H_2 -funnel. Given their similarity, this is not surprising. However, there is a clear difference in the strength of these effects. Therefore, for the effects of ϕ_{M_1} and ϕ_{A_t} we only give the argued reasons for the strength-difference but not for the existence of the effect, as these are assumed to be same as for the H_1 -funnel.

Firstly we note that the effects of ϕ_{A_t} and ϕ_{M_1} are much weaker. The reason for these weaker effects most likely lies within the pMSSM points used. As mentioned, the masses of the LSP are in a much broader range around the perfect resonance point of $\frac{m_{H_2}}{2}$ than they were within the H_1 -funnel: around 20 GeV compared to 5 GeV. If we then look at figure 7.1, we see that the closer to this resonance point one gets the lower the Ωh^2 value. In other words, the DM annihilation process happens more during freeze-out. The more such a process happens, the bigger the effect of the phases, as these phases now determine the efficiency of a more-occurring process. Therefore the pMSSM points created for the H_2 -funnel, with a broader bandwidth around the resonance, result in the weakening of the observed phase effects. The creation of $H - 2$ -funnel pMSSM points was forced to use this bigger bandwidth because points closer to the resonance resulted in too low Ωh^2 predictions. Thus, irrespective of this creation process, due to selection on a correct relic density prediction, we would always be left with these weakened effects of ϕ_{A_t} and ϕ_{M_1} .

In contrast, the relative effect of ϕ_{A_b} has become much stronger. Again, we attribute this effect to loop-corrections on the ‘SM-end’ of the most dominant process. In this case, the most dominant process had two bottoms as end product. The bottoms as end product stems from the coupling of the cpMSSM Higgs bosons to quarks, and especially the distinction in this coupling between up- and down-type quarks (table A.1) In this table we see that the coupling of the H_2 -boson to down-type quarks is enhanced by $\frac{1}{\cos \beta}$, which is large for our decoupled pMSSM points. For this dominant DM annihilation process, the following diagram is one of the loop corrections.



This loop correction is most likely one of the more dominant contributions of the loop corrections. This fact originates in the $H_2 - \tilde{b} - \tilde{b}^*$ coupling, which is given in A.4.⁶ First of all this coupling will have the highest efficiency for two bottoms as end product, as otherwise generational mixing would have been needed to get two bottoms as the end product. Furthermore, this coupling is again enhanced by the $\frac{1}{\cos \beta}$ in $y_b = \frac{gm_b}{\sqrt{2}M_W \cos \beta}$. However, this coupling is not dependent on A_b , thus does not explain the observed ϕ_{A_b} effect. To explain the ϕ_{A_b} effect of this diagram we turn to the $\tilde{\chi}_1^0 - \tilde{b} - b$ coupling, which is given in A.18. This coupling is dependent on the sfermion mixing matrices, which for a sbottom-bottom coupling depend

⁶Again for simplicity we associate the ϕ_2 matrix as mostly contributing to H_2 etc.. .

on \mathbf{A}_b . Therefore, the $\tilde{\chi}_1^0 - \tilde{b} - b$ coupling introduces the observed $\phi_{\mathbf{A}_b}$ effect.

We do, however, note that the observed $\phi_{\mathbf{A}_b}$ effect also really depends on the value of \mathbf{A}_b itself. The pMSSM point used for figure 7.3 has >8000 GeV as \mathbf{A}_b value, and thus a large $\phi_{\mathbf{A}_b}$ effect. In contrast, almost no effect of $\phi_{\mathbf{A}_b}$ is seen for another H_2 -funnel point with \mathbf{A}_b around 260 GeV. The other points have an \mathbf{A}_b in between these two extremes, and thus also show a ‘medium’ $\phi_{\mathbf{A}_b}$ effect.

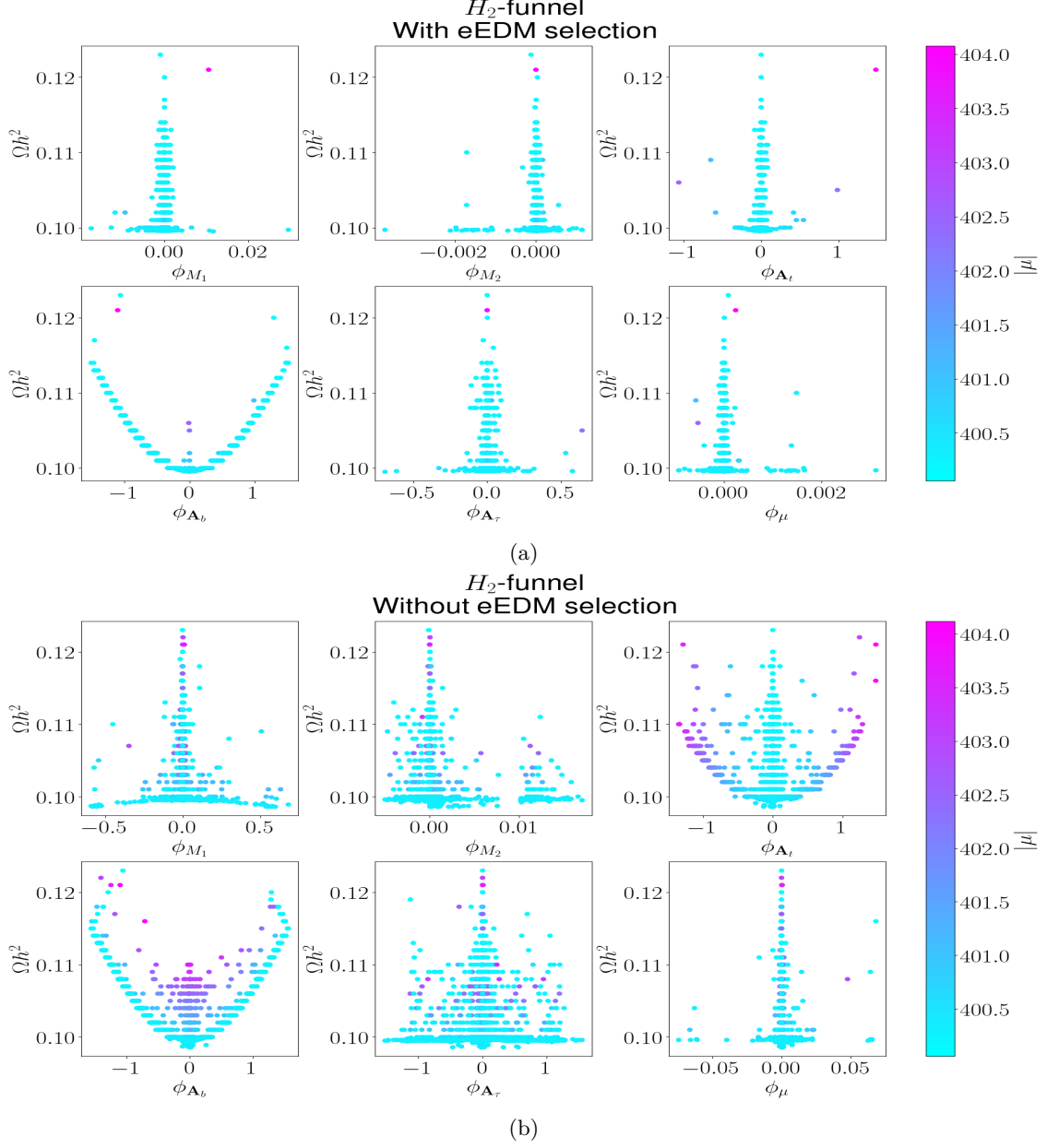
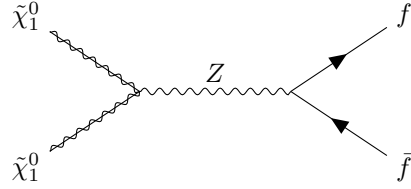


Figure 7.3: Scatter plots of phase values versus the dark matter relic density of cpMSSM points. The phase values were sampled for a pMSSM point in the H_2 -funnel. The colour represents $|\mu|$, which is not a free parameter of the software but is calculated via the tadpole equations (3.56). (a): with selection on the eEDM limit. (b): without selection on the eEDM limit.

7.3 Z-funnel

The last funnel category to look at is the funnel that uses a Z boson featuring in a s-channel propagator. This funnel is categorized by the pMSSM points for which the following process is dominant during freeze-out.



where f denotes an arbitrary fermion.

To select points for this funnel we can once again look at a mass resonance, as well as at the dominant process from the calculation. In this case the mass resonance is given by: $m_{\tilde{\chi}_1^0} = \frac{M_Z}{2} \pm 5$ GeV. Figure 7.4 again shows the need for both these selection requirements, as within both the relic density range (7.1) and the mass resonance range there exist points with a non Z -funnel dominant DM annihilation process.

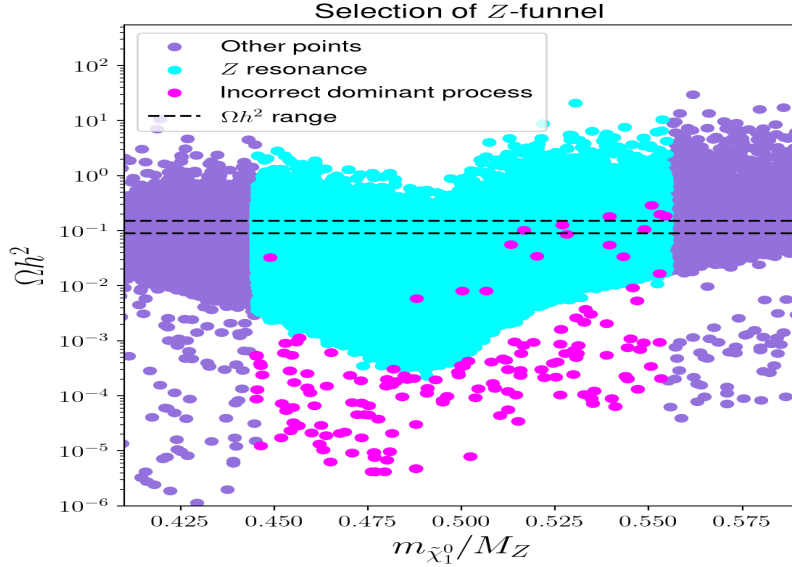


Figure 7.4: Scatter plot of pMSSM points that are of interest for the selection of Z -funnel points.

Figure 7.5 shows the scatter plots of the Z -funnel study. These plots again show the general phase effects also seen in the plots of the other pMSSM Z -funnel points in the best manner.

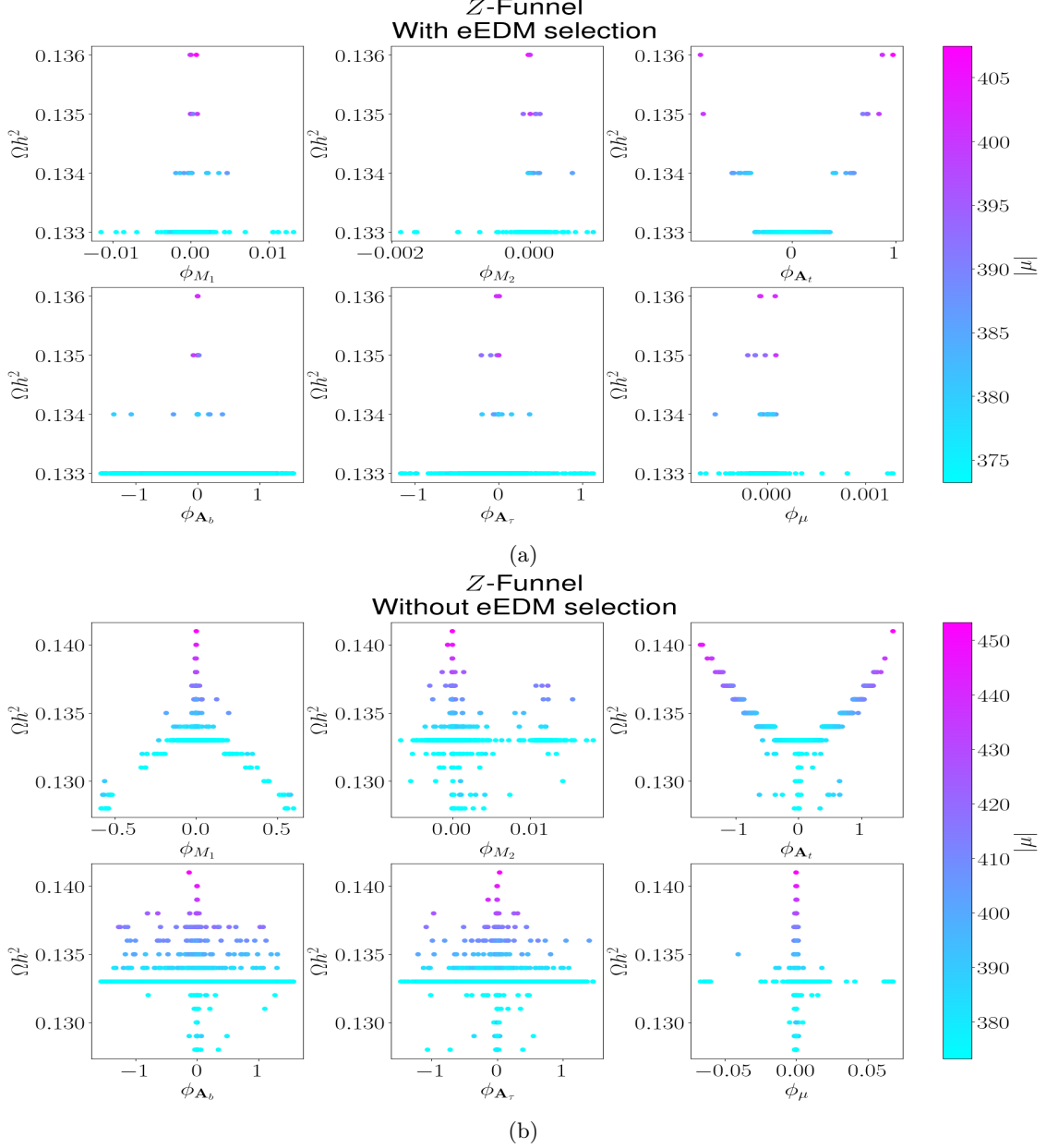


Figure 7.5: Scatter plots of phase values versus the dark matter relic density of cpMSSM points. The phase values were sampled for a pMSSM point in the Z-funnel. The colour represents $|\mu|$. (a): with selection on the eEDM limit. (b): without selection on the eEDM limit.

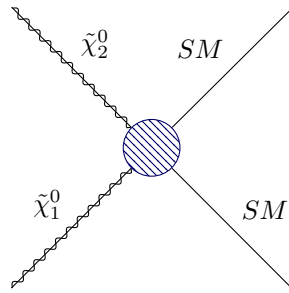
The first thing to note is the clear restriction that the eEDM limit has on the possible phase effects. In this case the restrictive effect is even more present than in the other funnels. However, this can also be due to the phase effects in the Z-funnel being weaker to begin with, since looking at figure 7.5, we observe, by the smaller range on the y-axes of the plots, that the effects are substantially less pronounced to begin with.

This absence of strong effects most likely has multiple reasons. First of all, $|\mu|$ is a much less influential parameter in this category. In general this is because we are no longer considering Higgs bosons, for which μ naturally is the main parameter as it is the parameter of the Higgs term within the superpotential. Therefore, ϕ_{A_t} , which influences $|\mu|$ through the tadpole equations, will have a much smaller effect on the Z-funnel process. Additionally, the tree-level coupling is no longer directly dependent on the phases of pa-

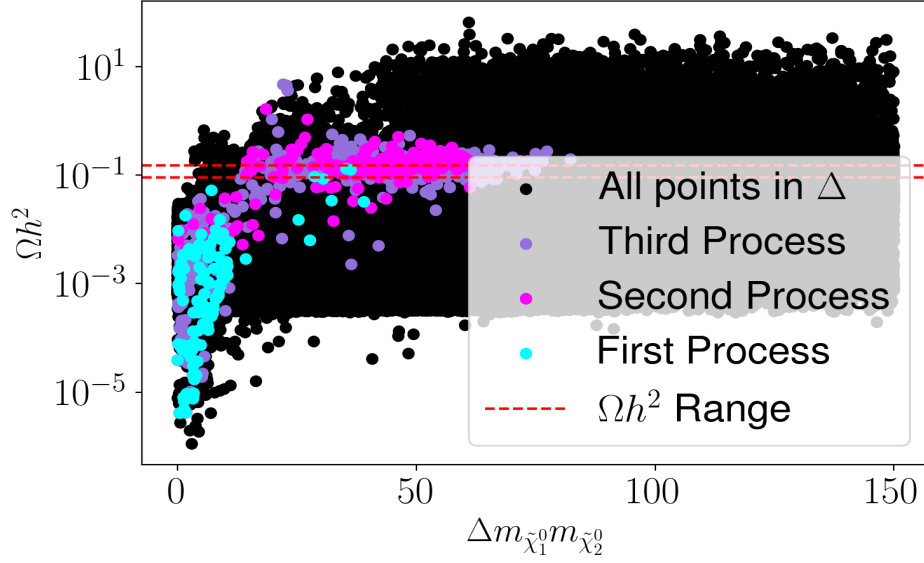
parameters that govern the neutralino composition, as was the case for the Higgs funnels. The absence of a direct dependence can be seen by the presence of only absolute values for the neutralino mixing matrix in equation A.17. Therefore, the phase effects of the parameters associated with \mathbf{N} will only come into play through higher-order loop corrections. These types of effects are typically much weaker than the tree-level effects seen in the Higgs funnels.

7.4 Neutralino Co-Annihilation

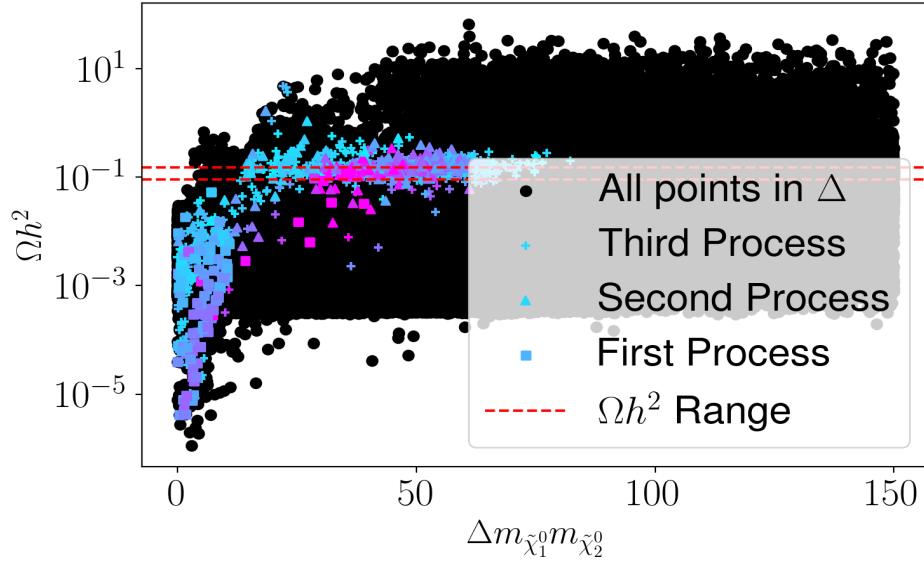
The previous sections all discussed dominant annihilation processes for the relic density. However there is also another possibility, that of co-annihilation. In other words, the LSP does not annihilate with itself, but uses another sparticle, to turn into at least two SM particles. In this section we look at co-annihilation of the LSP with the second-lightest neutralino. Co-annihilation concerns, in general, more possible forms of dominant processes, with the same start and end product, than annihilation would. Therefore, to be explicit: we are interested in pMSSM points with dominant processes during freeze-out that would ‘fall’ under this general process.



As mentioned in section 4.2, the efficiency of these kinds of processes is governed by the mass difference between the two co-annihilation partners. Therefore to select pMSSM points within this category we first take a look at pMSSM points that have $\Delta m_{\tilde{\chi}_1^0 \tilde{\chi}_2^0} \equiv m_{\tilde{\chi}_2^0} - m_{\tilde{\chi}_1^0} < 100$ GeV.



(a)



(b)

Figure 7.6: Two scatter plots of pMSSM points within $\Delta m_{\tilde{\chi}_1^0 m_{\tilde{\chi}_2^0}}$ of 100 GeV. (a): the colouring depends on the first neutralino-co-annihilation dominant process/channel and which rank it has in the order of dominant processes, as computed by the calculation software. (b): the form of the marker replaces the colouring of (a). The colouring is now given by the relative contribution of that most dominant neutralino co-annihilation process.

However, figure 7.6 clearly shows that selecting on the mass difference is not enough to find the correct points. By looking at figure 7.6a we see that only a small amount of pMSSM points that have as the most dominant process a neutralino-co-annihilation process remain in the correct relic density range. Therefore, we also present figure 7.6b, which shows the points with the most dominant DM (co)annihilation processes as the second or third most dominant DM (co)annihilation process. These processes do contribute quite substantially to the relic density prediction. Thus, to check the effects that will be seen in the three pMSSM points with neutralino-co-annihilation contributions as most dominant process, we will also select some of the aforementioned points, where we limit ourselves to the points in which the most dominant neutralino

co-annihilation process contributes no less than half the contribution of the overall most dominant process.

Figure 7.7 presents the scatter plots associated with cpMSSM samples for a pMSSM point that had a neutralino-co-annihilation process as the most dominant process during freeze-out. It turned out that the effects seen for ‘first process’ neutralino co-annihilation points were very similar to those for points that had the first neutralino co-annihilation process as either the second or third most dominant process.

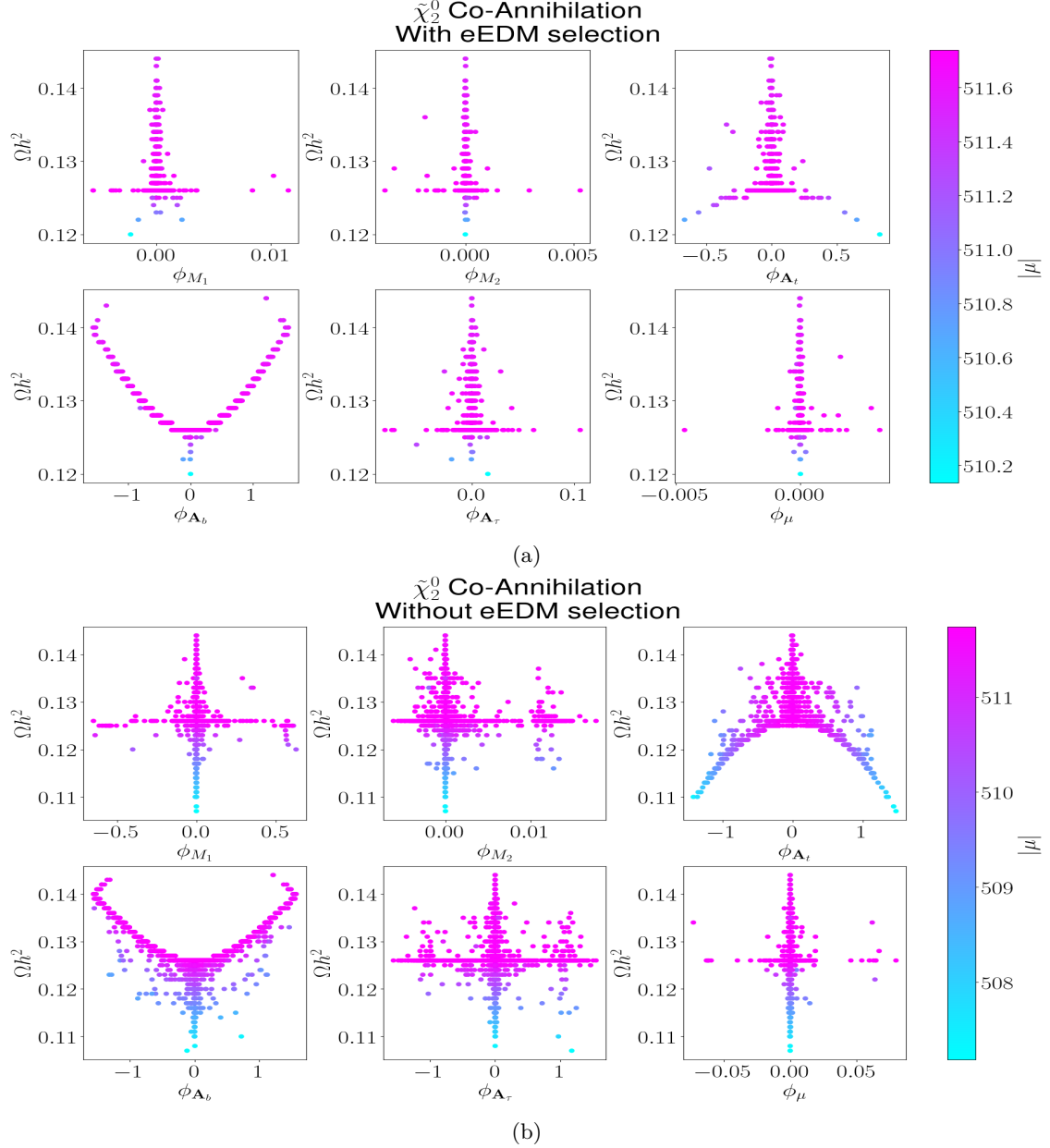
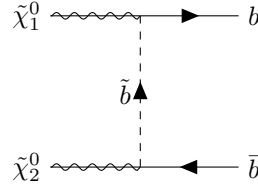


Figure 7.7: Scatter plots of phase values versus the dark matter relic density of cpMSSM points. The phase values were sampled for a pMSSM point with a neutralino co-annihilation as most dominant DM (co-)annihilation process. The colour represents $|\mu|$. (a): with selection on the eEDM limit. (b): without selection on the eEDM limit.

We again see that the eEDM does have a restrictive effect on the possible relic density consequences of the phases. However, compared to the previous funnels the restriction is weaker. The effect of $\phi_{\mathbf{A}_b}$ mostly survives imposing the eEDM limit. Moreover, values of $\phi_{\mathbf{A}_t}$ are allowed to become large enough to observe the start of the ‘full effect’ seen when not imposing the eEDM limit.

The effect of $\phi_{\mathbf{A}_t}$ is explained similarly as before through the loop corrections of the tadpole equations (3.56). In this case this reasoning might even be slightly more extreme due to the presence of two neutralinos, as such $|\mu|$ could have double the influence on the efficiency of the dominant process.⁷ This is reflected by the fact that even though $|\mu|$ varies less compared to the funnels, the effect it has is stronger, or at least as strong.

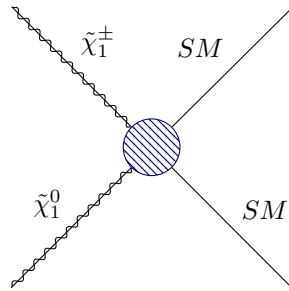
For the quite strong effect of $\phi_{\mathbf{A}_b}$ we take a look at one of the contributing tree-level diagrams for neutralino co-annihilation.



The coupling of neutralino-bottom-sbottom is given in A.18. First of all this coupling is dependent on the mixing matrix of the down squarks. These entries are influenced by the trilinear terms. Thus for the sbottom propagator, $\phi_{\mathbf{A}_b}$ influences the efficiency of this process. However, this diagram can also be made with top final states and a stop propagator. This stop diagram is less dominant because we are using pMSSM points with relatively high $\tan\beta$ values. As can be seen in A.20 this ensures that the coupling for down-type quarks/squarks becomes stronger compared to the coupling of up-type quarks/squarks.⁸ Therefore, although a similar effect for $\phi_{\mathbf{A}_t}$ might be present, it will be smaller than the effect for $\phi_{\mathbf{A}_b}$. Thus, the effect of $\phi_{\mathbf{A}_t}$ will most likely be dominated by the effects through the tadpole equations of $\phi_{\mathbf{A}_t}$.

7.5 Chargino Co-Annihilation

The next co-annihilation possibility we consider is that of chargino co-annihilation. In other terms, we are looking at pMSSM points that have dominant contributions towards the relic density of processes described by



The selection of these points is much more straightforward than that of neutralino co-annihilation. This can be seen if we make a replica of figure 7.6a for chargino co-annihilation. This plot is presented in figure 7.8. In contrast to neutralino co-annihilation, we see a good number of points that both fall in the correct relic density range and have a chargino co-annihilation process as the most dominant process.

⁷However, as will be seen in chargino co-annihilation, two particles’ composition possibly governed by the same parameters might also lead to a negative extreme of the effect.

⁸This effect does depend on the composition of the two neutralinos.

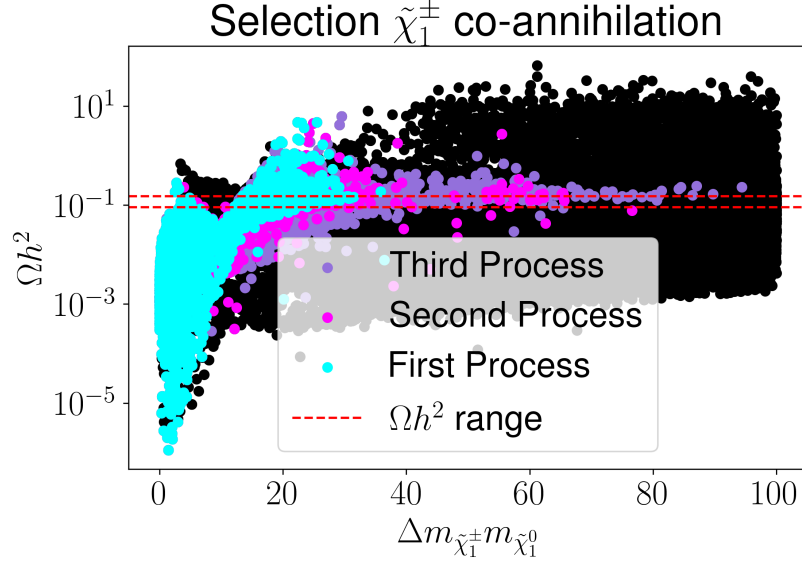


Figure 7.8: Scatter plot of pMSSM points within $\Delta m_{\tilde{\chi}_1^0 m_{\tilde{\chi}_1^\pm}} \equiv m_{\tilde{\chi}_1^\pm} - m_{\tilde{\chi}_1^0}$ of 100 GeV. The colouring depends on the first chargino co-annihilation dominant process/channel and which rank it has in the order of dominant processes, as reported by the calculation software.

Figure 7.9 shows the studied scatter plots for chargino co-annihilation. The main thing seen in these plots is that there seems to be (almost) *no effect* from any of the phases. This absence of effects is also present when not imposing the eEDM limit. We argue this to be because the composition of the co-annihilating chargino and neutralino is governed by the same parameter: M_2 or μ . If this is the case, the relative composition between the two particles does not change, even though the value of the governing parameter itself does. Therefore, the efficiency of a process that contains both these particles is not changed by the introduction of phases. To understand why the composition of these sparticles is governed by the same parameter, we look at the mass matrices of charginos and neutralinos defined in section 3.3.4. These matrices consist of the same parameters, apart from M_1 . However, for the chargino and neutralino to be close to each other in mass, the typical case is that M_1 is not lighter than M_2 and μ , as then the LSP would be lighter than the lightest chargino. Of course, accidentally it could happen that through combinations of the parameters the chargino and neutralino reach a similar mass, but this is a quite rare scenario. In such a rare scenario a lot of mixing of gauge eigenstates would occur, which enhances the possibility that experimental limits are not satisfied one way or another. Therefore, in most scenarios the chargino and neutralino are of similar composition, resulting in (close) to no CP-violating effects on the relic density.

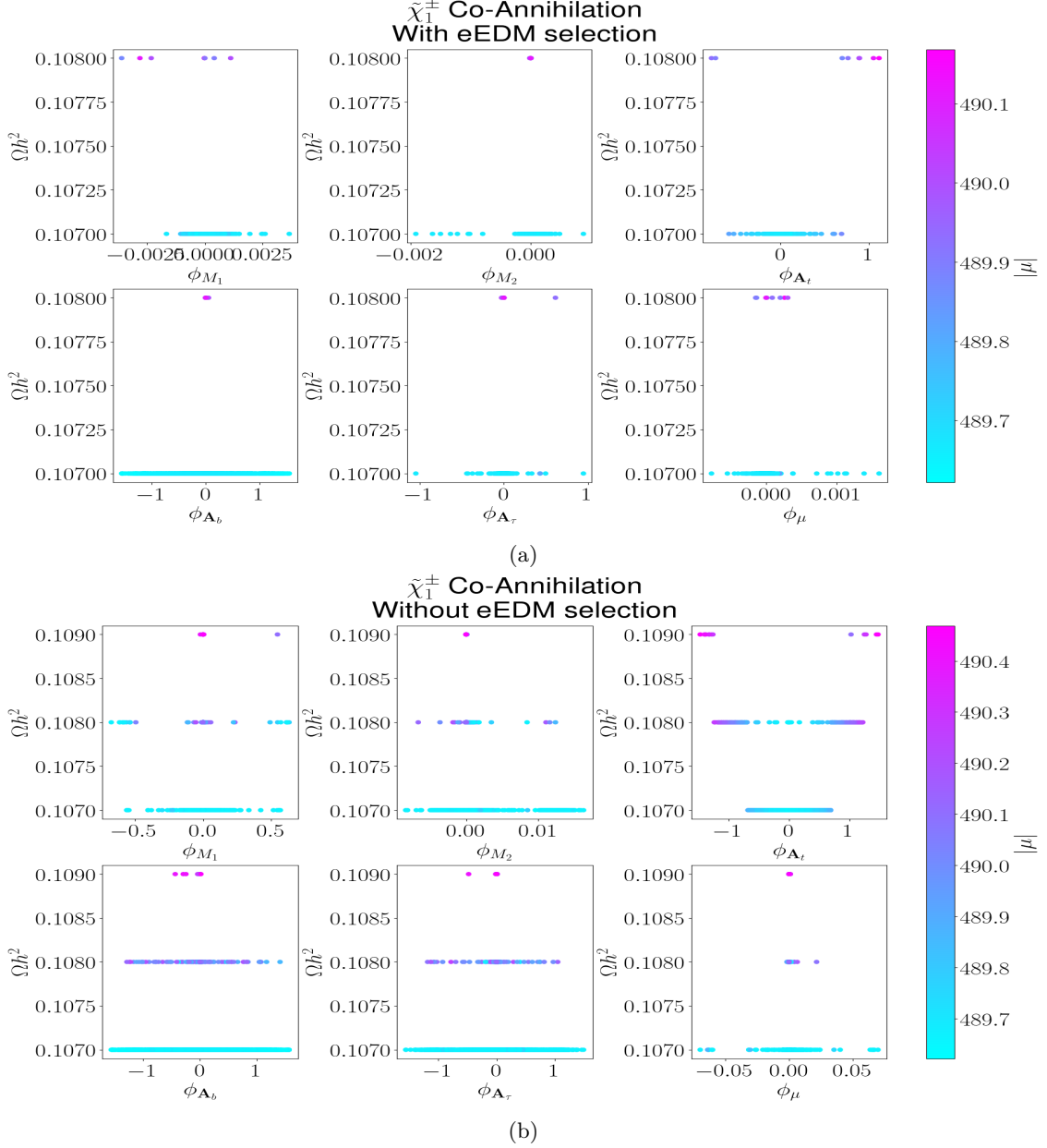
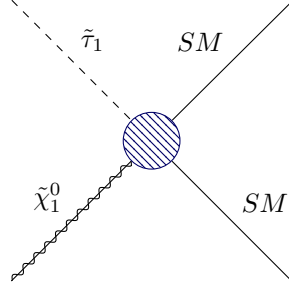


Figure 7.9: Scatter plots of phase values versus the dark matter relic density of cpMSSM points. The phase values sampled originate from a pMSSM point with a chargino co-annihilation as most dominant DM (co-)annihilation process. The colour represents $|\mu|$. (a): with selection on the eEDM limit. (b): without selection on the eEDM limit.

7.6 Stau Co-Annihilation

The next co-annihilation category to look at is that of co-annihilation between the stau and LSP. The general process that we are looking for as being dominant during freeze-out is now given by:



Note the 1 subscript for the stau, this subscript indicates that among the stau mass eigenstates we only consider the lightest eigenstate for a co-annihilation process. This is because co-annihilation is most dominant for sparticles that are close together in mass with the LSP. By definition of mass-ordering and the LSP, the lowest mass eigenstate of the third-generation sfermion will be closest to the mass of the LSP. Therefore, the co-annihilation is always most dominant for this lowest-mass eigenstate.

To select pMSSM points in which a stau co-annihilation process is the dominant process for the relic density, we use the same procedure as in the previous co-annihilation sections. By looking at figure 7.10, we see that there is a good number of points with the correct dominant process and correct relic density prediction available. However, we can also see that the effect of stau co-annihilation seems much weaker compared to the co-annihilation with a chargino or neutralino.

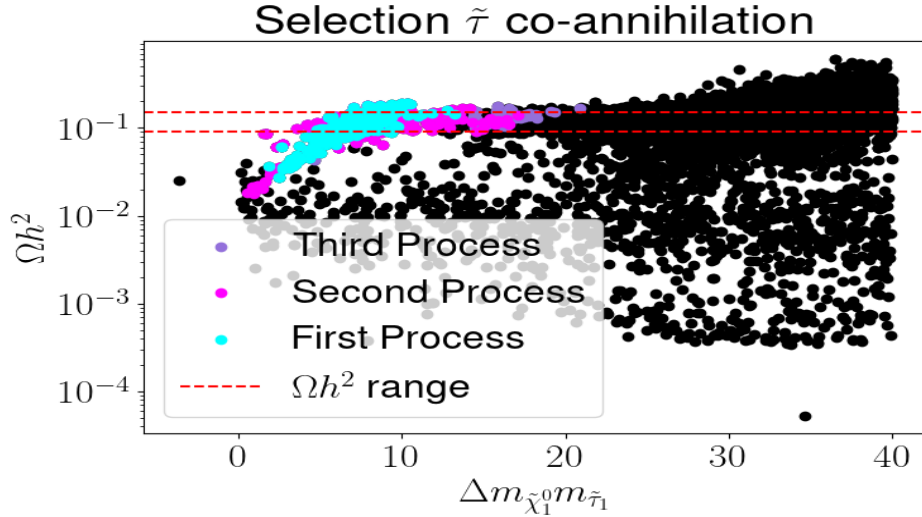


Figure 7.10: Scatter plot of pMSSM points within $\Delta m_{\tilde{\chi}_1^0} m_{\tilde{\tau}_1} \equiv m_{\tilde{\tau}_1} - m_{\tilde{\chi}_1^0}$ of 40 GeV, where $\tilde{\tau}_1$ denotes the lightest mass eigenstate of the stau. The colouring depends on the first stau co-annihilation dominant process/channel and which rank it has in the order of dominant processes, as reported by the calculation software.

Figure 7.11 shows the scatter plots that best show the CP-violating effects seen for stau co-annihilation on the prediction of the relic density.

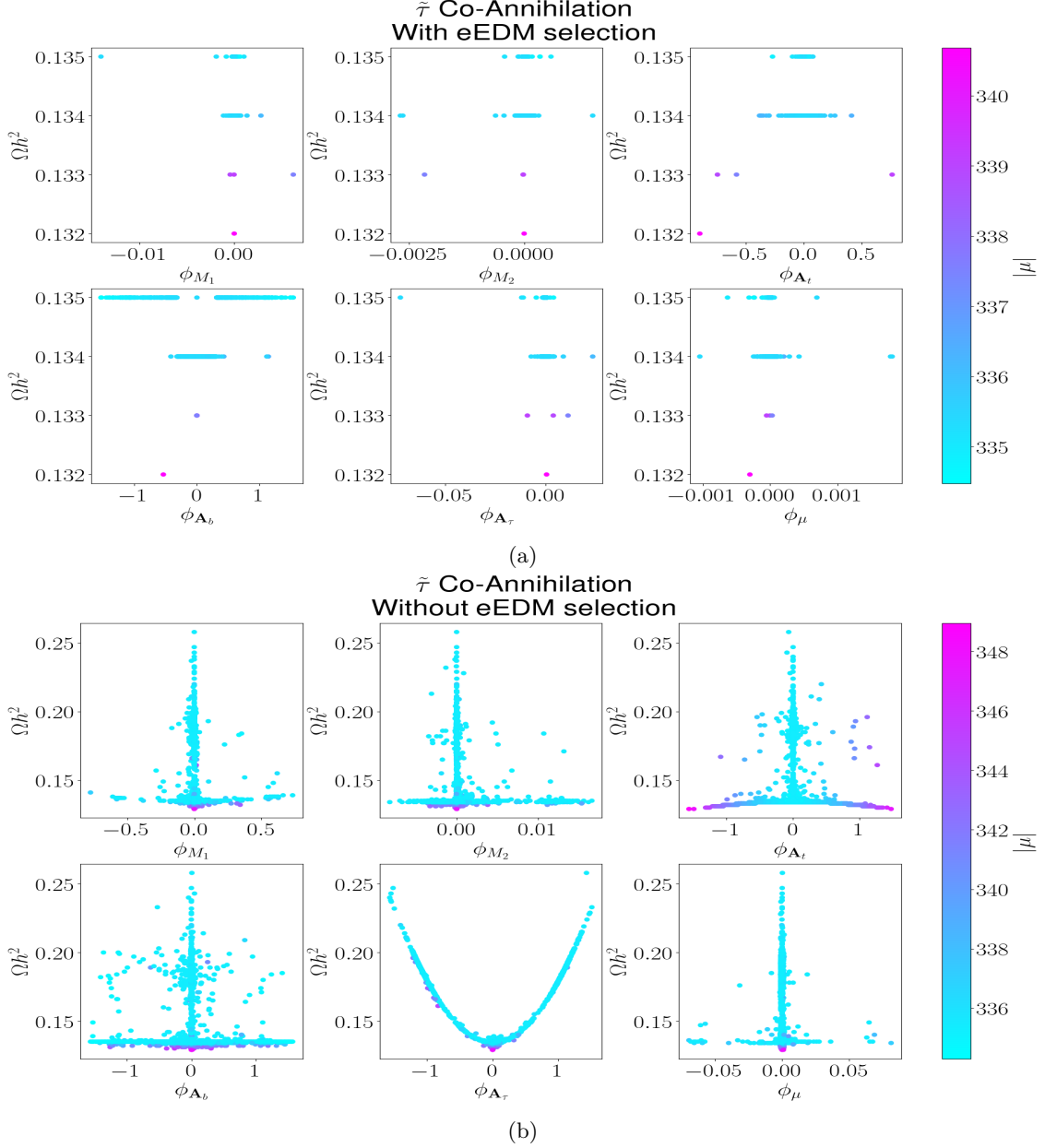


Figure 7.11: Scatter plots of phase values versus the dark matter relic density of cpMSSM points. The phase values sampled originate from a pMSSM point with a stau co-annihilation dominant process. The colour represents $|\mu|$. (a): with selection on the eEDM limit. (b): without selection on the eEDM limit.

Naturally, there is a very strong ϕ_{A_τ} effect showing up. This effect stems from the coupling between the LSP and the stau, into a tau propagator, in which the trilinear coupling A_τ is present. To be exact, A_τ is present in the mixing between the left- and right-handed states [15]. However, the main problem with this effect is that it gets fully removed by imposing the eEDM limit. This happens because, as mentioned before, for stau co-annihilation to be dominant, we need the masses of the stau and the LSP to be close together. If we then look at the two-loop diagrams of the eEDM (Barr-Zee) diagrams in section 4.2, we see diagrams that couple via the Higgs bosons to a stau loop. The smaller the mass of the stau, the higher the contribution of such a diagram. Thus, if we introduce CP-violating phases for stau co-annihilation pMSSM points, this easily leads to large eEDM predictions for the generated cpMSSM point. In conclusion, due to the needed phenomenology of stau co-annihilation pMSSM points, we practically cannot introduce ϕ_{A_τ} .

values. However, this phase is the only one to introduce effects on the relic density. Thus, in practice, no CP-violating effects survive imposing the eEDM limit for stau co-annihilation points after imposing the eEDM limit.

7.7 Slepton co-annihilation

Another category of co-annihilation is that of LSP co-annihilation with the lightest slepton of the first two generations, which we denote by \tilde{e}_1 in this section. Of course, note that technically we are also considering smuon-like sleptons. They are just mass-degenerate in the (c)pMSSM. Possible pMSSM points for this category are slightly more limited by experimental limits (see C.3). To be exact, the limit on $\Delta m_{\tilde{\chi}_1^0 \tilde{e}_1} \equiv m_{\tilde{e}_1} - m_{\tilde{\chi}_1^0}$, the fact that the lightest slepton should be heavier than $\tilde{\chi}_2^0$ and $\tilde{\chi}_1^\pm$, and the limit of $m_{\tilde{e}_1} > 240$ GeV. However, as can be seen in figure 7.12 there are some interesting pMSSM points with just the correct relic density prediction.

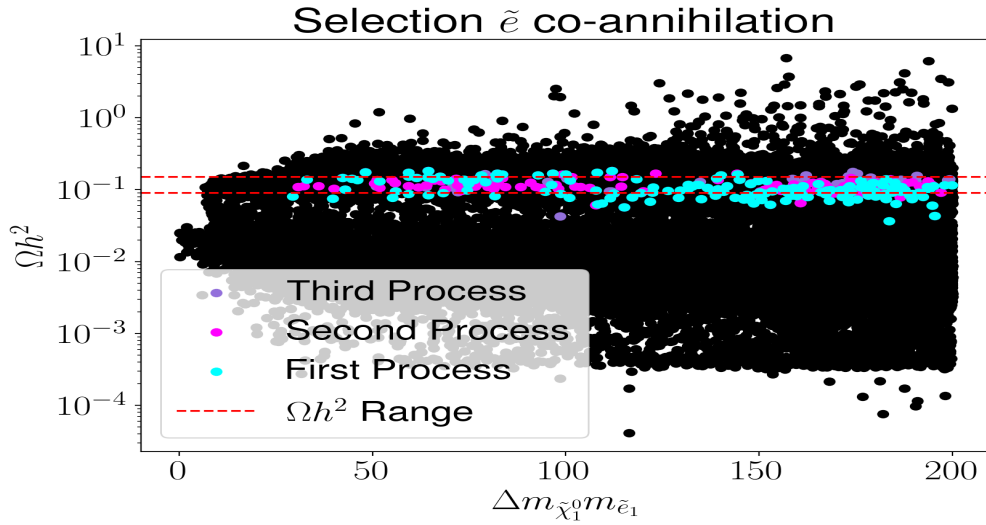


Figure 7.12: Scatter plot of pMSSM points with a mass difference between \tilde{e}_1 and $\tilde{\chi}_1^0$ of less than 200 GeV, where \tilde{e}_1 denotes the lightest mass eigenstate of the first two generations sleptons. The colouring depends on the first slepton co-annihilation dominant process/channel and which rank it has in the order of dominant processes, as reported by the calculation software.

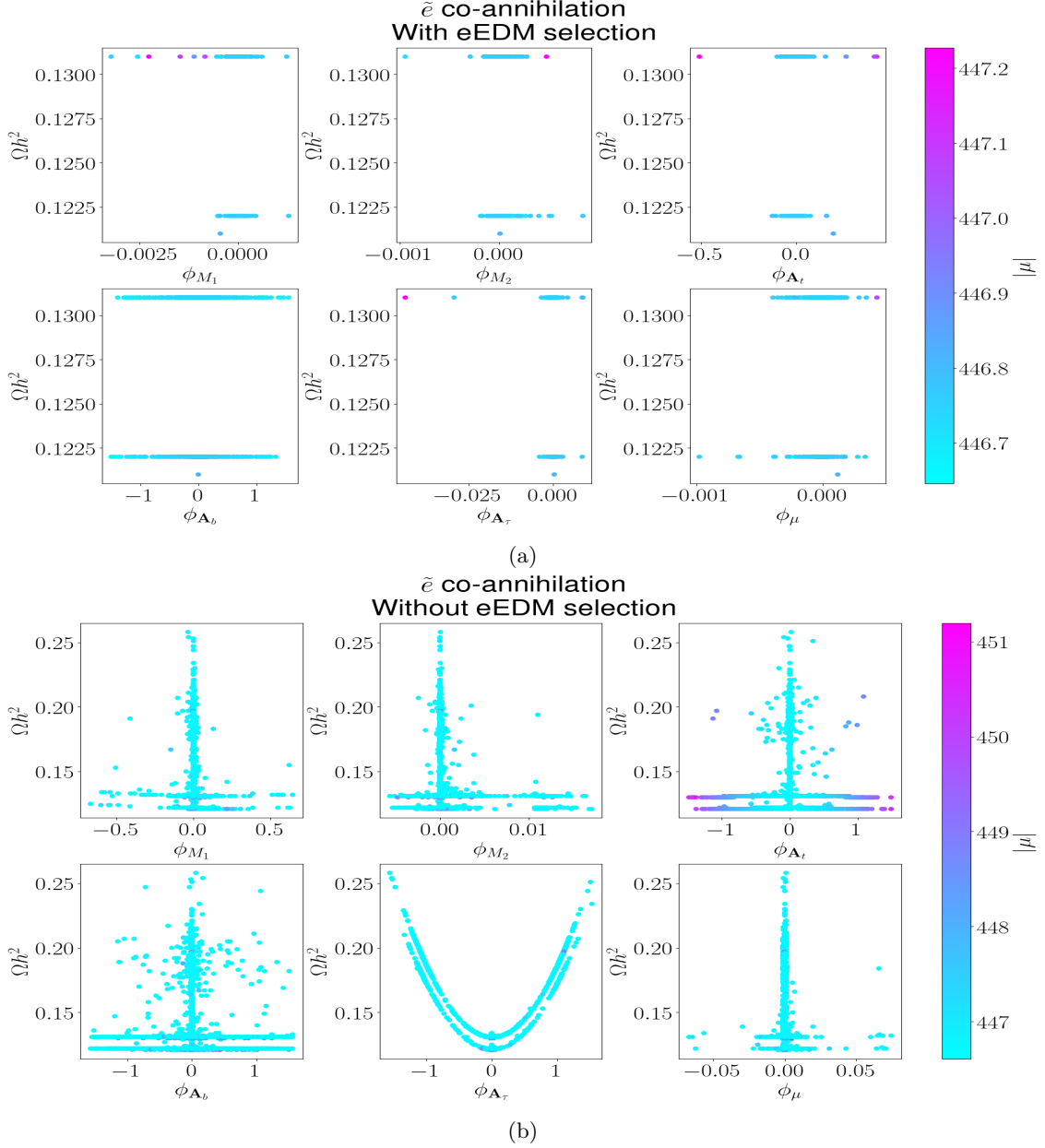


Figure 7.13: Scatter plots of phase values versus the dark matter relic density of cpMSSM points. The phase values sampled originate from a pMSSM point with a slepton co-annihilation dominant process. The colour represents $|\mu|$. (a): with selection on the eEDM limit. (b): without selection on the eEDM limit.

Figure 7.13 shows the scatter plots for one of the selected pMSSM points with a most dominant slepton co-annihilation process. We first of all notice the severe restriction of imposing the eEDM limit. This is most likely because all of the pMSSM points with a dominant slepton co-annihilation process, also have a very low stau mass. Thus, the phase effects seen are exactly the same for this category as for stau co-annihilation, including the restriction that the eEDM provides and the only effect being that of ϕ_{A_τ} .

In contrast to stau co-annihilation, we do see two bands within these plots. This again stems from the fact that all of these points have a low stau mass. As a consequence, there are not one but two co-annihilation processes happening for these points: stau and slepton co-annihilation. Small differences in parameters, in this case most likely caused by phases, then result in one of the two being slightly more dominant than the

other. The ultimate relic density prediction is dependent on which of the two is the most dominant, where there is a slight difference between either case. This results in two bands being present, ‘visualising’ which process is more dominant during what time of freeze-out.

7.8 Sbottom Co-Annihilation

The next category looks at pMSSM points for which the dominant relic density process is that of sbottom co-annihilation. As a reminder, we are looking at processes similar to that visualized for stau co-annihilation, only the $\tilde{\tau}_1$ is replaced by \tilde{b}_1 .

Sbottom co-annihilation points did not exist enough in the original pMSSM dataset.⁹ Therefore we opted to make these points ourselves. This procedure consisted of finding bino-like LSP points with $\Delta m_{\tilde{\chi}_1^0 m_{\tilde{b}_1}} \equiv m_{\tilde{b}_1} - m_{\tilde{\chi}_1^0} < 200$ GeV. For these points we set M_1 close to $m_{\tilde{b}}$, which should result in $\tilde{\chi}_1^0$ particles with a mass close to $m_{\tilde{b}}$ as well. Similar to the points created for the H_2 -funnel, we do this only for very bino-like LSP points with $\mu \gg m_{\tilde{b}_1}$, as that gives us the possibility to leave the parameter hierarchy intact otherwise. By making a large number of similar points, only differing in the ‘mass difference’ set between M_1 and $m_{\tilde{b}}$, we created some relevant pMSSM points. However, these were still not clear-cut sbottom co-annihilation. Apparently, sbottom co-annihilation is very dependent on the number of sbottom particles present in the early universe. For a large number of these points, a process in which sbottom sparticles themselves annihilated away became the most dominant, as that process heavily influences the number of sbottoms present during freeze-out. This number influences the sbottom co-annihilation both by efficiency: the more sbottoms, the more co-annihilation, as well as by decay of sbottom particles into DM once co-annihilation is no longer possible. To be pure within this study we would like to use points that do not have this process as the most dominant. Luckily, we did create three pMSSM points with a sbottom co-annihilation as the most dominant process. Although the prediction of relic density for these points was slightly too high, these pMSSM points were still used. Figure 7.14 shows the scatter plots for one of these points.

⁹There existed only two pMSSM points that had a sbottom co-annihilation process as *third* most dominant process.

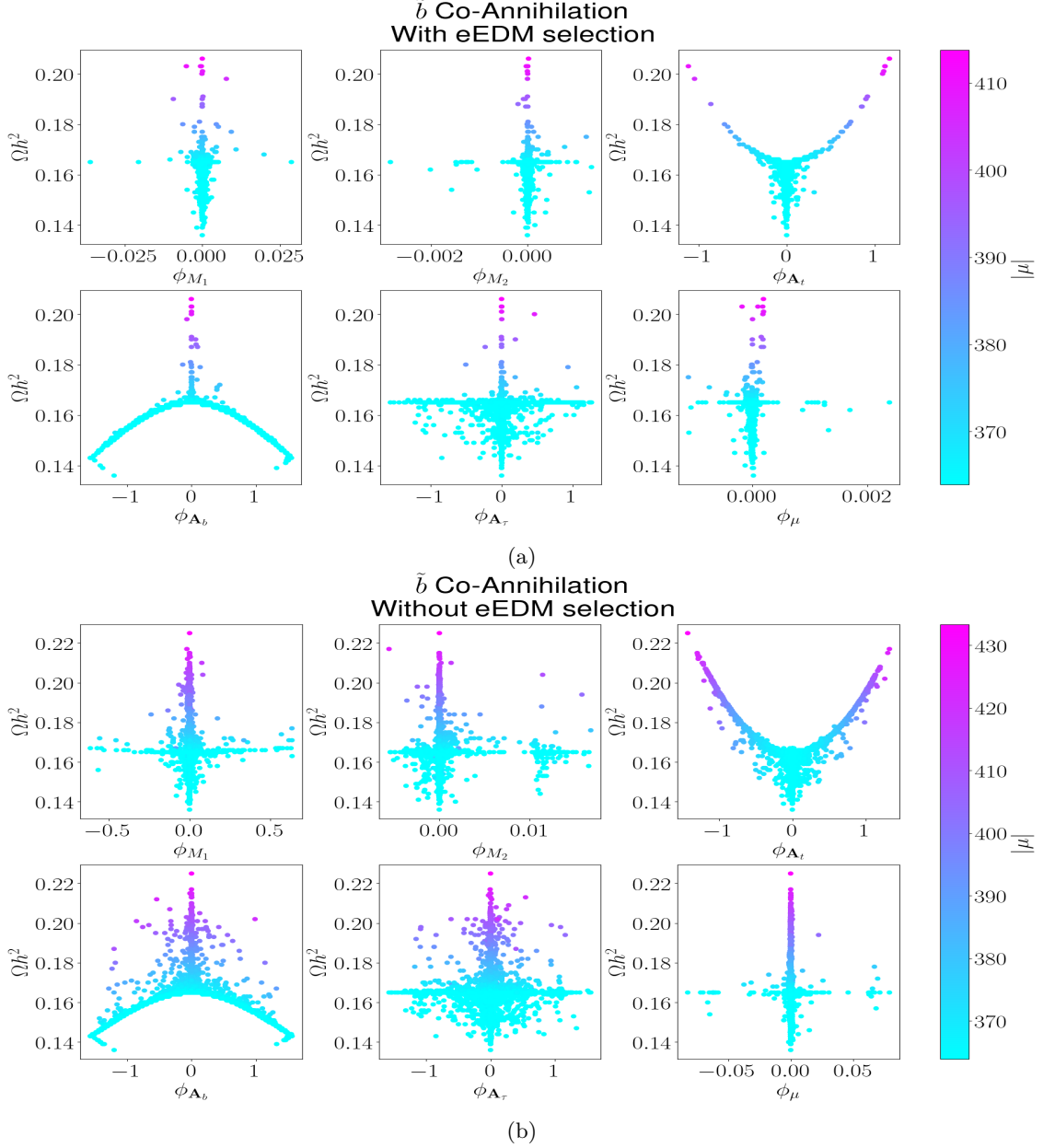


Figure 7.14: Scatter plots of phase values versus the dark matter relic density of cpMSSM points. The phase values sampled originate from a pMSSM point with a sbottom co-annihilation dominant process. The colour represents $|\mu|$. (a): with selection on the eEDM limit. (b): without selection on the eEDM limit.

The first thing to notice is that most effects in this category survive imposing the eEDM limit, even though in this case we have a sbottom mass close to the LSP mass, as was also the case for the stau. Why in this case that does not lead to very restricted phase values for $\phi_{\mathbf{A}_b}$ seems to be connected with the mixing of the left and right-handed sfermions into mass eigenstates. As can be seen for the Higgs-sfermion-sfermion couplings (as present in the Barr-Zee diagrams) shown in A.4, these couplings depend on the trilinear couplings through exactly the mixing of left- and right-handed states. Thus, the closer the masses of the two sfermions are, the higher the influence of the corresponding trilinear coupling on eEDM important diagrams, as similar mass eigenstates lead to more mixing in left- and right-handed eigenstates. It turns out that the masses of the two staus are consistently closer together for our stau co-annihilation points than the masses of the sbottoms for our sbottom co-annihilation points. To be specific, the average mass difference between

$m_{\tilde{b}_1}$ and $m_{\tilde{b}_2}$ is 4196.99 GeV for our sbottom co-annihilation points, whereas the average mass difference between $m_{\tilde{\tau}_1}$ and $m_{\tilde{\tau}_2}$ is 170.12 GeV for our stau co-annihilation points.¹⁰ Thus any phase contribution to the eEDM of the corresponding trilinear coupling is much weaker for the sbottom co-annihilation than it was for stau co-annihilation.

The most expected effect is that of $\phi_{\mathbf{A}_b}$, as the trilinear \mathbf{A}_b term is present in the left- and right-handed mixing of sbottom states [15]. Furthermore, we also see an effect of $\phi_{\mathbf{A}_t}$, and again this can be attributed to its relationship with μ through the tadpole equations. If we again look at the neutralino-bottom-sbottom expression in A.18, we see non-absolute value entries of the neutralino mixing matrix. Therefore, μ , and thus $\phi_{\mathbf{A}_t}$, has a strong influence on the strength of a sbottom co-annihilation process.

7.9 Bulk

The last category to look at is the bulk category. In other words, all pMSSM points that do not fall into any co-annihilation or funnel category. The selection of these points is less interesting, therefore we directly present figure 7.15 with the most general scatter plots for this category.

Firstly, we notice the strong restrictions on phase values by the eEDM limit in 7.15. This can be explained by the fact that most bulk points need larger amounts of higgsino or wino contribution to the LSP than other categories, as otherwise the dark matter relic density does not reach (the lower) desired values. Higgsinos or winos generally couple stronger than the bino, which results in high contributions to the one-loop eEDM diagrams. Thus even small CP-violating phase values will contribute strongly to higher eEDM predictions.

However, even if we ignore the strong eEDM restriction, we only see an effect on the relic density concerning $\phi_{\mathbf{A}_t}$. This is again its effect on the neutralino composition through the loop corrections of the tadpole equations, which surely is one of the main CP-violating effects on the dark matter relic density shown in this thesis.

¹⁰For completeness sake, the mass difference for the stau mass eigenstates did not exceed 300 GeV.

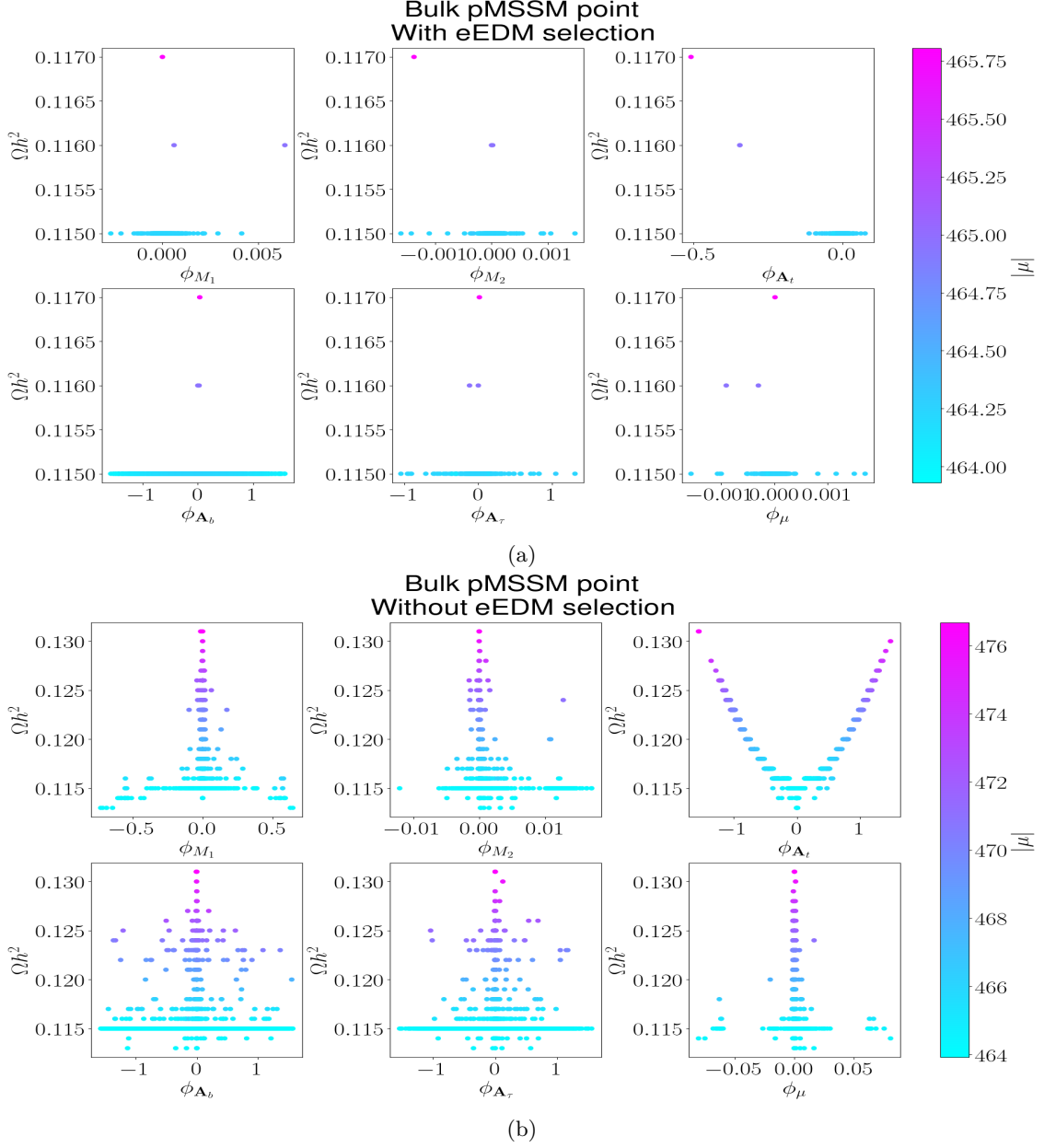


Figure 7.15: Scatter plots of phase values versus the dark matter relic density of cpMSSM points originating from a pMSSM point in the bulk category. The colour represents $|\mu|$. (a): with selection on the eEDM limit. (b): without selection on the eEDM limit.

Chapter 8

Conclusion and Outlook

The study of CP-violating effects on the dark matter relic density using a self-made ML cpMSSM sampler wraps up the thesis. Firstly, it has been shown that it is possible to sufficiently learn a normalizing flow model to sample cpMSSM points based on a given pMSSM point. Through the usage of non-conventional validation methods, like the likelihood ratio, visual validations and volume approximation, we were able to determine that our model does not sample the cpMSSM phase space in unwanted manners. The introduced sampler does not only generate copies and does seem to sample a substantial amount of the available phase space in a reasonably uniform manner. These validation methods, although not extremely complex, were influential in solving this complex, non-conventional task. The sampler generated >50% correct samples for a given pMSSM point, where correctness is determined by the limit on the eEDM contribution introduced by the CP-violating phases.

Although this means that the new sampler was not perfect, it is most definitely a step forward for research into the cpMSSM. In contrast to previously used samplers, the normalizing flow can be used in a fully automatic process. This enables a more automatic study of cpMSSM points, to determine interesting observable predictions in this SUSY model. Moreover, because the model generates >50% correct samples, the calculation software also gets used effectively in this automatic process. Lastly, the new sampler is very efficient and can generate millions of interesting samples within realistic time frames.

In this thesis the usefulness of the new sampler has been shown through a study into the effects of CP-violating phases on the dark matter relic density. Two main effects were found in this study. Firstly, the fact that imposing the eEDM limit is a severe restriction on the possible effects of the introduced phases. Examples are the ϕ_{A_τ} effect in stau co-annihilation, and the removal of any ϕ_{M_1} effect for all annihilation categories. Secondly, a strong effect was found for ϕ_{A_t} in most categories, which is caused by its influence on $|\mu|$. This influence enters through the Yukawa terms in the loop corrections of the tadpole equations (3.56) of the MSSM. As far as we know, this is a novel and possibly unexpected effect. Of course, other (co-)annihilation category-specific effects were found. For example the general weakening of CP-violating effects for the Z -funnel, compared with the H_1 and H_2 funnels, due to the presence of absolute values in the dominant couplings. Other examples are the ϕ_{A_b} effects that enter through loop corrections of the H-funnel and the absence of any effects for chargino co-annihilation points. However, the two main effects mentioned at the beginning of this paragraph were seen in general over multiple categories.

8.1 Outlook

Naturally, there are also possibilities to extend this work in the future and explore other opportunities. For the ML sampler there always will be the possibility to expand the dataset that was used, as more data usually leads to a better model. In this case there might actually be more arguments for new data as well, not necessarily more. The current dataset does not fully sample the available parameter space of μ . In our calculation software μ is not given, as it is calculated via the tadpole equations. However, these equations do not determine the sign of μ . In the used dataset all points were accidentally given a positive μ sign. By

also using points with a negative μ , the model’s performance might improve.

Besides that specific expansion of the dataset, it would be interesting to see if more data might lead the model to become more dependent on the given pMSSM point. The general features found by the model are, as shown by the reached acceptance percentage, not incorrect and very interesting. However we would expect to see more difference between different pMSSM points. That the current model does not show this could point to three things. Firstly, it could be that the data is not representative enough, either we need more samples per pMSSM point, or we need more different pMSSM points. Both are possibilities for future research. Secondly, we could also look at further optimising the ML model to reach a more conditionalized sampler. Possibilities for this could be a longer learning process, or altering the loss function and reward taking into account the condition more strictly. Lastly, it could point to the fact that we might better learn the model on a six-dimensional phase vector to begin with. As explained, through a bug in the Spheno-CPV software we were forced to switch from including ϕ_{M_3} to removing it, made possible by the present $U(1)$ symmetries of the cpMSSM. By removing ϕ_{M_3} the model might learn more freely, as it is now no longer bounded by the dependence of one of the dimensions. However, the internal dependence could also be used as a cross-check, as we can explicitly reward the model for outputting samples that do have a correct dependence on (for example) ϕ_{M_3} . But to do so we would first need to be sure that the model is actually capable of learning this ‘hyperplane’. However, we should also keep in mind the possibility that the unconditionality of the sampler is actually correct from a physics standpoint.

A last possibility for the ML sampler could be to tune the bias correction in the model. This bias emerges in the dataset due to the naive sampling of phases for the dataset using a logarithmic distribution. Currently, we decided to either fully correct for this bias or fully ignore it (section 5.4.1). However, it would be interesting to see what happens if we tune this bias using a (hyper)parameter of the model. Especially as figure B.1 and B.2 do show that incorporating this correction does have the intended effect of sampling larger phases.

Another possible avenue for future research lies at the edge of ML and physics. As explained, there is no theoretical consensus on a_μ and the validity of its discrepancy with the SM (4.1). This led us to not implement the lower limit of a_μ . As this allows higher masses, it also could allow for higher phase values, which we hoped to see within the generated samples by the model. However, the current model has not learned such a relationship, at least not in a significant manner. It would be interesting to see what would happen if we, for example, fine-tune a learned model on a dataset consisting of only correct or only incorrect points according to the theoretical limits of a_μ .

For the DM relic density study we could always have a more precise look at some of the observed effects. It would be very interesting to further explore the loop corrections of the tadpole equations, to confirm and further explain the effect of ϕ_{A_t} on $|\mu|$. Due to the time constraints of this internship, no further exploration is presented here. However, given that this effect was quite surprising as well as influential, further research is definitely encouraged. Naturally, other observed phase effects on the dark matter relic density given in this thesis also warrant further exploration.

Finally, future research should test the limits of the introduced ML sampler by testing it for other phenomenological observables. It is this scenario where the true potential of our sampler lies. Through our creation of an automatic process for sampling cpMSSM points, it should become more feasible to study the cpMSSM for any type of experimental limit or theoretical prediction, given enough interesting pMSSM points, which are more readily available or more easily made. This should help to practically exclude the (cp)MSSM as BSM model, or to better understand it for future endeavours within SUSY, in our quest to find the solution to the flaws of the SM.

Bibliography

- [1] B. Odom, D. Hanneke, B. D’Urso, and G. Gabrielse. New measurement of the electron magnetic moment using a one-electron quantum cyclotron. *Phys. Rev. Lett.*, 97:030801, Jul 2006.
- [2] ATLAS collaboration. Observation of a new particle in the search for the standard model higgs boson with the atlas detector at the lhc. *Physics Letters B*, 716(1):1–29, 2012.
- [3] S. Abachi et al. (D0 Collaboration). Observation of the top quark. *Phys. Rev. Lett.*, 74:2632–2637, Apr 1995.
- [4] Adrian Signer. Abc of susy. *Journal of Physics G*, 36:073002, 2009.
- [5] Howard Baer and Xerxes Tata. *The Minimal Supersymmetric Standard Model*, page 127–189. Cambridge University Press, 2006.
- [6] A. Djouadi et al. The Minimal supersymmetric standard model: Group summary report. In *GDR (Groupement De Recherche) - Supersymetrie*, 12 1998.
- [7] Andrei D Sakharov. Violation of cp invariance, c asymmetry, and baryon asymmetry of the universe. *Soviet Physics Uspekhi*, 34(5):392, may 1991.
- [8] J.H. Kotecha and P.M. Djuric. Gaussian particle filtering. *IEEE Transactions on Signal Processing*, 51(10):2592–2601, 2003.
- [9] Virginia Trimble. Existence and nature of dark matter in the universe. *Annual Review of Astronomy and Astrophysics*, 25(1):425–472, 1987.
- [10] G. Bélanger, F. Boudjema, S. Kraml, A. Pukhov, and A. Semenov. Relic density of neutralino dark matter in the mssm with cp violation. *Phys. Rev. D*, 73:115007, Jun 2006.
- [11] Stephen P. Martin. A Supersymmetry Primer. In *Perspectives on Supersymmetry. Edited by KANE GORDON L. Published by World Scientific Publishing Co. Pte. Ltd*, pages 1–98. World Scientific, 1998.
- [12] Wikipedia contributors. Standard model — Wikipedia, the free encyclopedia, 2023. [Online; accessed 3-October-2023].
- [13] Michael Edward Peskin and Daniel V. Schroeder. *An Introduction to Quantum Field Theory*. Westview Press, 1995. Reading, USA: Addison-Wesley (1995) 842 p.
- [14] J. Wess and B. Zumino. Supergauge transformations in four dimensions. *Nuclear Physics B*, 70(1):39–50, 1974.
- [15] M. Drees, P. Roy, and R. Godbole. *Theory and Phenomenology of Sparticles: An Account of Four-dimensional $N=1$ Supersymmetry in High Energy Physics*. World Scientific, 2004.
- [16] Sidney Coleman and Jeffrey Mandula. All possible symmetries of the s matrix. *Phys. Rev.*, 159:1251–1256, Jul 1967.
- [17] Marrit Schutten. *Low-energy observables and fine-tuning in the MSSM: one convention to rule them all*. PhD thesis, University of Groningen, 2023.

- [18] L. Girardello and M.T. Grisaru. Soft breaking of supersymmetry. *Nuclear Physics B*, 194(1):65–76, 1982.
- [19] Stefan Alte, Matthias König, and Matthias Neubert. Exclusive weak radiative higgs decays in the standard model and beyond. *Journal of High Energy Physics*, 2016(12), dec 2016.
- [20] R. L. Workman and Others. Review of Particle Physics. *PTEP*, 2022:083C01, 2022.
- [21] B. C. Allanach et al. SUSY Les Houches Accord 2. *Comput. Phys. Commun.*, 180:8–25, 2009.
- [22] Patrick Draper and Heidi Rzehak. A review of higgs mass calculations in supersymmetric models. *Physics Reports*, 619:1–24, mar 2016.
- [23] F. Gabbiani, E. Gabrielli, A. Masiero, and L. Silvestrini. A complete analysis of fcnc and cp constraints in general susy extensions of the standard model. *Nuclear Physics B*, 477(2):321–352, 1996.
- [24] R. D. Peccei and Helen R. Quinn. CP Conservation in the Presence of Instantons. *Phys. Rev. Lett.*, 38:1440–1443, 1977.
- [25] R. D. Peccei and Helen R. Quinn. Constraints Imposed by CP Conservation in the Presence of Instantons. *Phys. Rev. D*, 16:1791–1797, 1977.
- [26] Savas Dimopoulos and Scott Thomas. Dynamical relaxation of the supersymmetric cp violating phases. *Nuclear Physics B*, 465(1):23–33, 1996.
- [27] G. W. Bennett and others. Final report of the e821 muon anomalous magnetic moment measurement at bnl. *Phys. Rev. D*, 73:072003, Apr 2006.
- [28] G. W. Bennett et al. Measurement of the positive muon anomalous magnetic moment to 0.7 ppm. *Phys. Rev. Lett.*, 89:101804, Aug 2002.
- [29] G. W. Bennett et al. Measurement of the negative muon anomalous magnetic moment to 0.7 ppm. *Phys. Rev. Lett.*, 92:161802, Apr 2004.
- [30] G. W. Bennett et al. Final report of the e821 muon anomalous magnetic moment measurement at bnl. *Phys. Rev. D*, 73:072003, Apr 2006.
- [31] G. Colangelo, A.X. El-Khadra, M. Hoferichter, A. Keshavarzi, C. Lehner, P. Stoffer, and T. Teubner. Data-driven evaluations of euclidean windows to scrutinize hadronic vacuum polarization. *Physics Letters B*, 833:137313, oct 2022.
- [32] M. Cè, A. Gérardin, G. von Hippel, R. J. Hudspith, S. Kuberski, H. B. Meyer, K. Miura, D. Mohler, K. Ottnad, S. Paul, A. Risch, T. San José, and H. Wittig. Window observable for the hadronic vacuum polarization contribution to the muon from lattice QCD. *Physical Review D*, 106(11), dec 2022.
- [33] Sz. Borsanyi et al. Leading hadronic contribution to the muon magnetic moment from lattice QCD. *Nature*, 593(7857):51–55, apr 2021.
- [34] M. E. Pospelov and I. B. Khriplovich. Electric dipole moment of the W boson and the electron in the Kobayashi-Maskawa model. *Sov. J. Nucl. Phys.*, 53:638–640, 1991.
- [35] Maxim Pospelov and Adam Ritz. Electric dipole moments as probes of new physics. *Annals of Physics*, 318(1):119–169, jul 2005.
- [36] M. Tanabashi and others. Review of particle physics. *Phys. Rev. D*, 98:030001, Aug 2018.
- [37] Dominik Stöckinger. The muon magnetic moment and supersymmetry. *Journal of Physics G: Nuclear and Particle Physics*, 34(2):R45–R91, dec 2006.
- [38] John Ellis, Jae Sik Lee, and Apostolos Pilaftsis. Electric dipole moments in the MSSM reloaded. *Journal of High Energy Physics*, 2008(10):049–049, oct 2008.

- [39] Tanya S. Roussy, Luke Caldwell, Trevor Wright, William B. Cairncross, Yuval Shagam, Kia Boon Ng, Noah Schlossberger, Sun Yool Park, Anzhou Wang, Jun Ye, and Eric A. Cornell. An improved bound on the electron’s electric dipole moment. *Science*, 381(6653):46–50, jul 2023.
- [40] The ACME Collaboration. Improved limit on the electric dipole moment of the electron. *Nature*, 562(7727):355–360, October 2018.
- [41] Paolo Gondolo and Graciela Gelmini. Cosmic abundances of stable particles: Improved analysis. *Nuclear Physics B*, 360(1):145–179, 1991.
- [42] N. Aghanim and other. Planck 2018 results. vi. cosmological parameters. *Astron. Astrophysics*, 641:A6, sep 2020.
- [43] Toby Falk, Keith A. Olive, and Mark Srednicki. Heavy sneutrinos as dark matter. *Physics Letters B*, 339(3):248–251, nov 1994.
- [44] Ian Goodfellow, Jean Pouget-Abadie, Mehdi Mirza, Bing Xu, David Warde-Farley, Sherjil Ozair, Aaron Courville, and Yoshua Bengio. Generative adversarial nets. In Z Ghahramani, M Welling, C Cortes, N Lawrence, and K Q Weinberger, editors, *Advances in Neural Information Processing Systems*, volume 27. Curran Associates, Inc., 2014.
- [45] Diederik P. Kingma and Max Welling. Auto-encoding variational bayes. In Yoshua Bengio and Yann LeCun, editors, *ICLR*, 2014.
- [46] Danilo Jimenez Rezende and Shakir Mohamed. Variational inference with normalizing flows. In *Proceedings of the 32nd International Conference on International Conference on Machine Learning - Volume 37*, ICML’15, page 1530–1538. JMLR.org, 2015.
- [47] Conor Durkan, Artur Bekasov, Iain Murray, and George Papamakarios. Neural spline flows. *Advances in neural information processing systems*, 32, 2019.
- [48] George V. Cybenko. Approximation by superpositions of a sigmoidal function. *Mathematics of Control, Signals and Systems*, 2:303–314, 1989.
- [49] Bob Stienen. *Working in high-dimensional parameter spaces: Applications of machine learning in particle physics phenomenology*. PhD thesis, Radboud University, 2021.
- [50] Melissa van Beekveld, Wim Beenakker, Marrit Schutten, and Jeremy De Wit. Dark matter, fine-tuning and $(g - 2)_\mu$ in the pMSSM. *SciPost Phys.*, 11:049, 2021.
- [51] Daniel Cosmin Porumbel, Jin Kao Hao, and Fred Glover. A simple and effective algorithm for the maxmin diversity problem. *Annals of Operations Research*, 186:275–293, 6 2011.
- [52] Diederik P. Kingma and Jimmy Ba. Adam: A method for stochastic optimization. *CoRR*, abs/1412.6980, 2014.
- [53] Alex Kolmus. personal communication.
- [54] Sheng Liu, Jian Zhang, and Binhai Zhu. Volume computation using a direct monte carlo method. *Lecture Notes in Computer Science (including subseries Lecture Notes in Artificial Intelligence and Lecture Notes in Bioinformatics)*, 4598 LNCS:198–209, 2007.
- [55] W. Porod and F. Staub. SPheno 3.1: extensions including flavour, CP-phases and models beyond the MSSM. *Computer Physics Communications*, 183(11):2458–2469, nov 2012.
- [56] S. Heinemeyer, W. Hollik, and G. Weiglein. FeynHiggs: a program for the calculation of the masses of the neutral -even higgs bosons in the MSSM. *Computer Physics Communications*, 124(1):76–89, jan 2000.

- [57] G. Belanger, F. Boudjema, and A. Pukhov. micrOMEGAs : a code for the calculation of Dark Matter properties in generic models of particle interaction. In *Theoretical Advanced Study Institute in Elementary Particle Physics: The Dark Secrets of the Terascale*, pages 739–790, 2013.
- [58] Bing Li, Carlos E., and M. Wagner. Cp-odd component of the lightest neutral higgs boson in the mssm. *Physical Review D*, 91(9), may 2015.
- [59] G. Aad et al. Searches for electroweak production of supersymmetric particles with compressed mass spectra in $\sqrt{s}=13$ tev p collisions with the atlas detector. *Physical Review D*, 101(5), mar 2020.
- [60] Martin Bauer, Ulrich Haisch, and Felix Kahlhoefer. Simplified dark matter models with two higgs doublets: I. pseudoscalar mediators. *Journal of High Energy Physics*, 2017(5), 2017.
- [61] M. Maggi. Review of searches for supersymmetric particles at LEP. In *33rd Rencontres de Moriond: Electroweak Interactions and Unified Theories*, pages 117–128, Paris, 1998. Edition Frontieres.
- [62] Federico Ambrogio, Juhi Dutta, Jan Heisig, Sabine Kraml, Suchita Kulkarni, Ursula Laa, Andre Lessa, Philipp Neuhauser, Humberto Reyes-González, Wolfgang Waltenberger, and Matthias Wolf. SModelS v1.2: Long-lived particles, combination of signal regions, and other novelties. *Computer Physics Communications*, 251:106848, jun 2020.
- [63] Jan Heisig, Sabine Kraml, and Andre Lessa. Constraining new physics with searches for long-lived particles: Implementation into SModelS. *Physics Letters B*, 788:87–95, jan 2019.
- [64] Juhi Dutta, Sabine Kraml, Andre Lessa, and Wolfgang Waltenberger. Smodels extension with the cms supersymmetry search results from run 2. *LHEP*, 1, 03 2018.
- [65] Federico Ambrogio, Sabine Kraml, Suchita Kulkarni, Ursula Laa, Andre Lessa, Veronika Magerl, Jory Sonneveld, Michael Traub, and Wolfgang Waltenberger. Smodels v1.1 user manual: Improving simplified model constraints with efficiency maps. *Computer Physics Communications*, 227:72–98, 2018.
- [66] Sabine Kraml, Suchita Kulkarni, Ursula Laa, Andre Lessa, Wolfgang Magerl, Doris Proschofsky-Spindler, and Wolfgang Waltenberger. SModelS: a tool for interpreting simplified-model results from the LHC and its application to supersymmetry. *The European Physical Journal C*, 74(5), may 2014.

Appendix A

Extra Material

A.1 All Generic Interactions within Supersymmetry

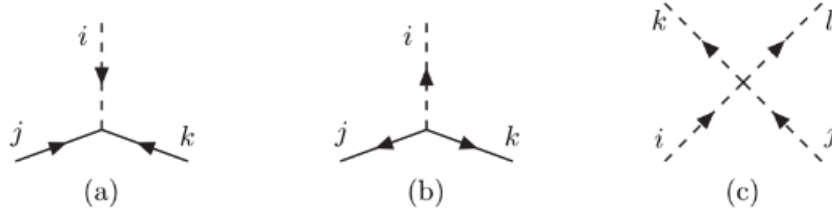


Figure A.1: The non-gauge interactions with a dimensionless coupling in supersymmetric theories: (a) scalar-fermion-fermion Yukawa y^{ijk} (b) the complex conjugate of (a): y_{ijk}^* , (c) quartic scalar interaction: $y^{ijn}y_{kln}^*$ [11].

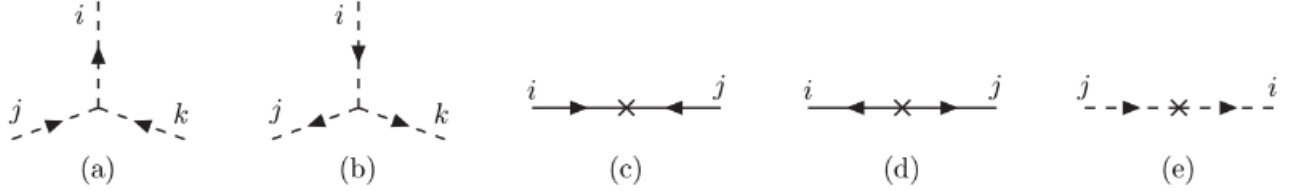


Figure A.2: The non-gauge interactions with a dimensionful coupling in supersymmetric theories: (a) $(\text{scalar})^3$ interaction vertex $M_{in}^*y^{jkn}$ (b) the complex conjugate of (a) (c) fermion mass term M^{ij} (d) conjugate fermion mass term M_{ij}^* (e) scalar squared mass term $M_{ik}^*M^{kj}$ [11].

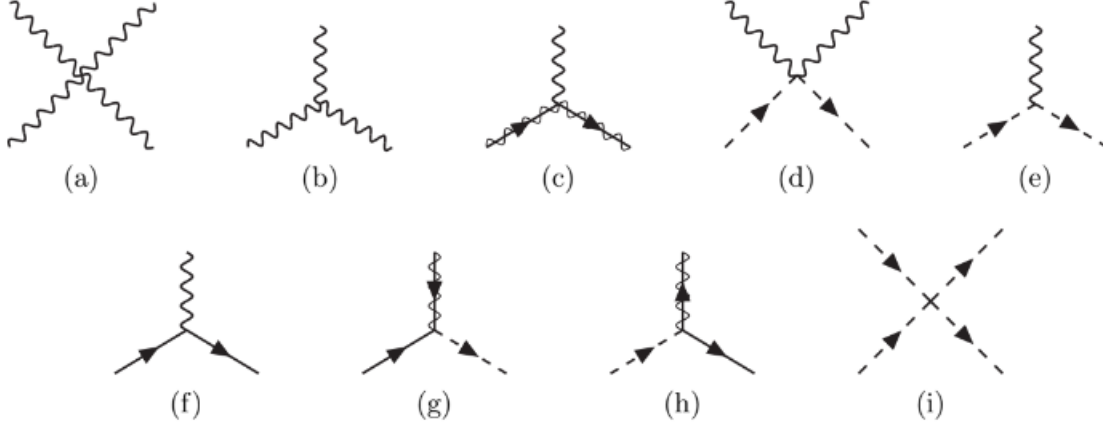
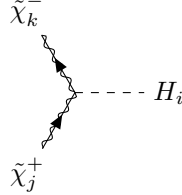


Figure A.3: The gauge interactions of a supersymmetric theory [11]

A.2 Couplings

Higgs-chargino interactions

This interaction is given by the following diagram:



The couplings for this diagram are given by a pseudoscalar (P) and a scalar (S) part of the Higgs boson.

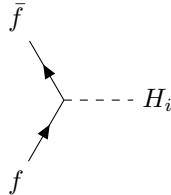
$$g_{H_i \tilde{\chi}_j^+ \tilde{\chi}_k^-}^S = \frac{1}{2} \left\{ [V_{j1}^* U_{k2}^* G_i^{\phi_1} + e^{-i\eta} V_{j2}^* U_{k1}^* G_i^{\phi_2}] + [j \leftrightarrow k]^* \right\}, \quad (\text{A.1})$$

$$g_{H_i \tilde{\chi}_j^+ \tilde{\chi}_k^-}^P = \frac{i}{2} \left\{ [V_{j1}^* U_{k2}^* G_i^{\phi_1} + e^{-i\eta} V_{j2}^* U_{k1}^* G_i^{\phi_2}] + [j \leftrightarrow k]^* \right\}, \quad (\text{A.2})$$

where $G_i^{\phi_1} = (\mathcal{O}_{i\phi_1} - i \sin \beta \mathcal{O}_{ia})$ and $G_i^{\phi_2} = (\mathcal{O}_{i\phi_2} - i \cos \beta \mathcal{O}_{ia})$. Here \mathcal{O} denotes the mixing matrix with CP violation as defined in section 3.3.1 and ϕ_1, ϕ_2 and a denote the three possible intermediate states, without the Goldstone boson, that \mathcal{O} transforms the mass eigenstates into. Furthermore, as defined in section 3.3.1 U and V denote the mixing matrices of the charginos.

Higgs-fermion interactions.

The scalar and pseudoscalar couplings between Higgs bosons and fermions is given by the following feynmann diagram:

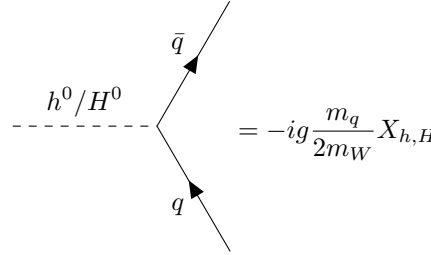


The corresponding pseudoscalar (P) and scalar (S) terms are given in table A.1 at tree level. For the expressions at higher order, including the re-summation of $\tan \beta$ the reader is referred to [17].

	$f = u$	$f = d, l$
$G_{H_i f f}^S$	$\mathcal{O}_{i\phi_2} / \sin \beta$	$\mathcal{O}_{i\phi_1} / \cos \beta$
$G_{H_i f \bar{f}}^P$	$-\mathcal{O}_{ia} \cot \beta$	$-\mathcal{O}_{ia} \tan \beta$

Table A.1: Couplings between Higgs bosons and fermions. \mathcal{O} denotes the mixing matrix with CP violation as defined in section 3.3.1 and ϕ_1, ϕ_2 and a denote the three (without the Goldstone boson) possible intermediate states that \mathcal{O} transforms the mass eigenstates into.

For intuition, to show the $\tan \beta$ dependence more clearly and to better see what happens in the decoupling limit with this coupling, we also present the couplings for H^0 and h^0 coupling with quarks:



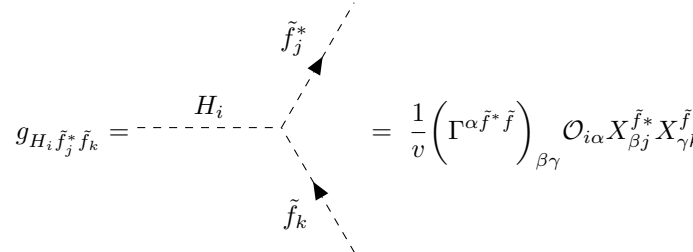
$$= -ig \frac{m_q}{2m_W} X_{h,H} \quad (\text{A.3})$$

where q denotes the quark and $X_{h,H}$ is given by the below table.

	u	d
X_h	$\frac{\cos \alpha}{\sin \beta}$	$-\frac{\sin \alpha}{\cos \beta}$
X_H	$\frac{\sin \alpha}{\sin \beta}$	$\frac{\cos \alpha}{\cos \beta}$

Higgs-sfermion interactions

In general we have:



$$= \frac{1}{v} \left(\Gamma^{\alpha \tilde{f}^* \tilde{f}} \right)_{\beta \gamma} \mathcal{O}_{i\alpha} X_{\beta j}^{\tilde{f}^*} X_{\gamma k}^{\tilde{f}} \quad (\text{A.4})$$

The latter two matrices (X) are matrices denoting the sfermion mixing matrices (for explicit expressions, see [17]) and \mathcal{O} is again the CP violating Higgs rotation matrix with v the vacuum expectation value. Lastly:

$\alpha = \phi_1, \phi_2, a$ and β and γ are spinoral indices. The effective couplings present within this thesis are:

$$\Gamma^{a\tilde{b}^*\tilde{b}} = \frac{1}{\sqrt{2}} \begin{pmatrix} 0 & iy_b^*(A_b^* \sin \beta + e^{i\eta} \mu \cos \beta) \\ -iy_b(A_b \sin \beta + e^{-i\eta} \mu^* \cos \beta) & 0 \end{pmatrix}, \quad (\text{A.5})$$

$$\Gamma^{\phi_1 \tilde{b}^* \tilde{b}} = \begin{pmatrix} -|y_b|^2 v \cos \beta + \frac{1}{4}(g^2 + \frac{1}{3}g'^2)v \cos \beta & -\frac{1}{\sqrt{2}}y_b^* A_b^* \\ -\frac{1}{\sqrt{2}}y_b A_b & -|y_b|^2 v \cos \beta + \frac{1}{6}g'^2 v \cos \beta \end{pmatrix}, \quad (\text{A.6})$$

$$\Gamma^{\phi_2 \tilde{b}^* \tilde{b}} = \begin{pmatrix} -\frac{1}{4}(g^2 + \frac{1}{3}g'^2)v \sin \beta & \frac{1}{\sqrt{2}}y_b^* \mu e^{i\eta} \\ \frac{1}{\sqrt{2}}y_b \mu^* e^{-i\eta} & -\frac{1}{6}g'^2 v \sin \beta \end{pmatrix}, \quad (\text{A.7})$$

$$\Gamma^{a\tilde{t}^*\tilde{t}} = \frac{1}{\sqrt{2}} \begin{pmatrix} 0 & iy_t^*(e^{-i\eta} A_t^* \cos \beta + \mu \sin \beta) \\ -iy_t(e^{i\eta} A_t \cos \beta + \mu^* \sin \beta) & 0 \end{pmatrix}, \quad (\text{A.8})$$

$$\Gamma^{\phi_1 \tilde{t}^* \tilde{t}} = \begin{pmatrix} -\frac{1}{4}(g^2 - \frac{1}{3}g'^2)v \cos \beta & \frac{1}{\sqrt{2}}y_t^* \mu \\ \frac{1}{\sqrt{2}}y_t \mu^* & -\frac{1}{3}g'^2 v \cos \beta \end{pmatrix}, \quad (\text{A.9})$$

$$\Gamma^{\phi_2 \tilde{t}^* \tilde{t}} = \begin{pmatrix} -|y_t|^2 v \sin \beta + \frac{1}{4}(g^2 - \frac{1}{3}g'^2)v \sin \beta & -\frac{1}{\sqrt{2}}y_t^* A_t^* e^{-i\eta} \\ -\frac{1}{\sqrt{2}}y_t A_t e^{i\eta} & -|y_t|^2 v \sin \beta + \frac{1}{3}g'^2 v \sin \beta \end{pmatrix}, \quad (\text{A.10})$$

$$\Gamma^{a\tilde{\tau}^*\tilde{\tau}} = \frac{1}{\sqrt{2}} \begin{pmatrix} 0 & iy_\tau^*(A_\tau^* \sin \beta + e^{i\eta} \mu \cos \beta) \\ -iy_\tau(A_\tau \sin \beta + e^{-i\eta} \mu^* \cos \beta) & 0 \end{pmatrix}, \quad (\text{A.11})$$

$$\Gamma^{\phi_1 \tilde{\tau}^* \tilde{\tau}} = \begin{pmatrix} -|y_\tau|^2 v \cos \beta + \frac{1}{4}(g^2 - g'^2)v \cos \beta & -\frac{1}{\sqrt{2}}y_\tau^* A_\tau^* \\ -\frac{1}{\sqrt{2}}y_\tau A_\tau & -|y_\tau|^2 v \cos \beta + \frac{1}{2}g'^2 v \cos \beta \end{pmatrix}, \quad (\text{A.12})$$

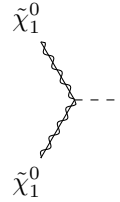
$$\Gamma^{\phi_2 \tilde{\tau}^* \tilde{\tau}} = \begin{pmatrix} -\frac{1}{4}(g^2 - g'^2)v \sin \beta & \frac{1}{\sqrt{2}}y_\tau^* \mu e^{i\eta} \\ \frac{1}{\sqrt{2}}y_\tau \mu^* e^{-i\eta} & -\frac{1}{2}g'^2 v \sin \beta \end{pmatrix}, \quad (\text{A.13})$$

$$\Gamma^{a\tilde{\nu}_\tau^* \tilde{\nu}_\tau} = 0, \quad \Gamma^{\phi_1 \tilde{\nu}_\tau^* \tilde{\nu}_\tau} = -\frac{1}{4}(g^2 + g'^2)v \cos \beta, \quad \Gamma^{\phi_2 \tilde{\nu}_\tau^* \tilde{\nu}_\tau} = \frac{1}{4}(g^2 + g'^2)v \sin \beta. \quad (\text{A.14})$$

All¹ couplings are given as matrices in the basis $(\tilde{f}_L, \tilde{f}_R)$ of the associated sfermion.

All expressions above this point are taken from [17], and changed where needed. All expressions below this point originate from [15].

h^0 - $\tilde{\chi}_1^0$ - $\tilde{\chi}_1^0$ coupling



$$-ig(-\mathcal{Q}_{11}^* \sin \alpha - S_{11}^* \cos \alpha), \quad (\text{A.15})$$

where \mathcal{Q}_{11} and S_{11} are:


$$\begin{aligned} \mathcal{Q}_{11} &= \frac{1}{2} \left(N_{13}(N_{12} - \tan(\theta_W)N_{11}) + N_{13}(N_{12} - \tan(\theta_W)N_{11}) \right), \\ S_{11} &= \frac{1}{2} \left(N_{14}(N_{12} - \tan(\theta_W)N_{11}) + N_{14}(N_{12} - \tan(\theta_W)N_{11}) \right). \end{aligned} \quad (\text{A.16})$$

The CP violating version of this coupling (with H_1) is not given, as that would become a very complex and messy coupling. The essence of the coupling that is important for this thesis is also present in the CP

¹With the exception of those corresponding with tau sneutrinos as those do not have a right-handed version within the MSSM.


conserving case.

Z - $\tilde{\chi}_1^0$ - $\tilde{\chi}_1^0$ coupling




$$Z = i \frac{g}{2c_W} \gamma_\mu \gamma^5 \left(|N_{13}|^2 - |N_{14}|^2 \right) \quad (\text{A.17})$$

$\tilde{\chi}_1^0$ - quark - squark coupling



$$\tilde{\chi}_1^0 = i \left((G_{is}^{qR})^* \left(\frac{1 - \gamma^5}{2} \right) + (G_{is}^{qL})^* \left(\frac{1 + \gamma^5}{2} \right) \right) \quad (\text{A.18})$$

and



$$\tilde{\chi}_1^0 = i \left((G_{is}^{qR}) \left(\frac{1 + \gamma^5}{2} \right) + (G_{is}^{qL}) \left(\frac{1 - \gamma^5}{2} \right) \right) \quad (\text{A.19})$$

$q = u, d$; $i = 1, 2, 3$; $s = 1, 2, 3, 4, 5, 6$. Here we define G_{is}^{qL} and G_{is}^{qR} by:

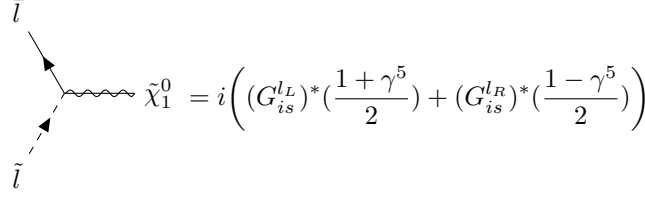
$$\begin{aligned} G_{is}^{uL} &= -\sqrt{2}g \left(\frac{1}{2}N_{12}^* + \frac{1}{6}\tan\theta_W N_{11}^* \right) \sum_{j=1}^3 W_{js}^{\tilde{u}*} X_{ji}^{uL} - \frac{g}{\sqrt{2}m_W \sin\beta} m_{u_i} N_{14}^* \sum_{j=1}^3 W_{(j+3)s}^{\tilde{u}*} X_{ji}^{uR}, \\ G_{is}^{uR} &= \frac{2\sqrt{2}}{3}g \tan\theta_W N_{11} \sum_{j=1}^3 W_{(j+3)s}^{\tilde{u}*} X_{ji}^{uR} - \frac{g}{\sqrt{2}m_W \sin\beta} m_{u_i} N_{14} \sum_{j=1}^3 W_{js}^{\tilde{u}*} X_{ji}^{uL}, \\ G_{is}^{dL} &= \sqrt{2}g \left(\frac{1}{2}N_{12}^* + \frac{1}{6}\tan\theta_W N_{11}^* \right) \sum_{j=1}^3 W_{js}^{\tilde{d}*} X_{ji}^{dL} - \frac{g}{\sqrt{2}m_W \cos\beta} m_{d_i} N_{13}^* \sum_{j=1}^3 W_{(j+3)s}^{\tilde{d}*} X_{ji}^{dR}, \\ G_{is}^{dR} &= -\frac{\sqrt{2}}{3}g \tan\theta_W N_{11} \sum_{j=1}^3 W_{(j+3)s}^{\tilde{d}*} X_{ji}^{dR} - \frac{g}{\sqrt{2}m_W \cos\beta} m_{d_i} N_{13} \sum_{j=1}^3 W_{js}^{\tilde{d}*} X_{ji}^{dL}. \end{aligned} \quad (\text{A.20})$$

In these terms W and X denote the sfermion and fermion mixing matrices respectively (for expressions see [15]). Further, W combines left and right handed mixing, whereas X explicitly is used for either one.

$\tilde{\chi}_1^0$ - lepton - slepton coupling

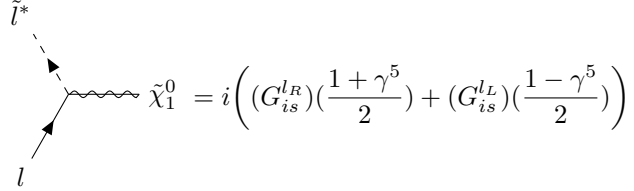
The below given expression is only for electron and selectron-like (s)particles, as that is the variant of this

vertex that is the most interesting for this thesis.



$$\tilde{\chi}_1^0 = i \left((G_{is}^{l_L})^* \left(\frac{1+\gamma^5}{2} \right) + (G_{is}^{l_R})^* \left(\frac{1-\gamma^5}{2} \right) \right) \quad (\text{A.21})$$

and



$$\tilde{\chi}_1^0 = i \left((G_{is}^{l_R}) \left(\frac{1+\gamma^5}{2} \right) + (G_{is}^{l_L}) \left(\frac{1-\gamma^5}{2} \right) \right) \quad (\text{A.22})$$

$l = e, \mu, \tau$; $i = 1, 2, 3$; $s = 1, 2, 3, 4, 5, 6$. Here we define $G_{is}^{l_L}$ and $G_{is}^{l_R}$ by:

$$\begin{aligned} G_{is}^{l_L} &= \frac{1}{\sqrt{2}} g \left(N_{12}^* + \tan \theta_W N_{11}^* \right) W_{is}^{\tilde{l}^*} - \frac{g}{\sqrt{2} m_W \cos \beta} m_{l_i} N_{13}^* W_{(i+3)s}^{\tilde{l}^*}, \\ G_{is}^{l_R} &= -\sqrt{2} g \tan \theta_W N_{11} W_{(i+3)s}^{\tilde{l}^*} - \frac{g}{\sqrt{2} m_W \cos \beta} m_{l_i} N_{13} W_{is}^{\tilde{l}^*}. \end{aligned} \quad (\text{A.23})$$

A.3 Loop Functions

This section provides the expressions for the loop functions used within section 4.1.

$$A(x) = -\frac{1}{2(1-x)^3} \left[-3 + 4x - x^2 - 2 \log(x) \right], \quad (\text{A.24})$$

$$B(x) = \frac{1}{2(1-x)^3} \left[1 - x^2 + 2x \log(x) \right], \quad (\text{A.25})$$

$$F(\tau) = \int_0^1 dx \frac{x(1-x)}{\tau - x(1-x)} \log \left[\frac{x(1-x)}{\tau} \right], \quad (\text{A.26})$$

$$f(\tau) = \frac{\tau}{2} \int_0^1 dx \frac{1-2x(1-x)}{x(1-x)-\tau} \log \left[\frac{x(1-x)}{\tau} \right], \quad (\text{A.27})$$

$$g(\tau) = \frac{\tau}{2} \int_0^1 dx \frac{1}{x(1-x)-\tau} \log \left[\frac{x(1-x)}{\tau} \right]. \quad (\text{A.28})$$

A.4 Augmentation Study

This section presents the numbers regarding the augmentation possibilities, as explained in section 5.3.4. The numbers are shown in table A.2. Further, it presents a small discussion and explanation with regards to a found mistake in the open source part of the calculation software.

The clear discussion point of table A.2 is the fact that 414 of the originally correct cpMSSM points, if fed through the calculation software again, led to incorrect cpMSSM points. We meticulously went through the pipeline of the calculation software, as visualized in figure C.1, and also the full pipeline as explained in 5.3.

Table A.2: Number of cpMSSM points that were calculated to have a low enough eEDM value before and after augmentation. For clarification: we started this test with 1000 correct cpMSSM points. After inputting these through the calculation software again, we were left with 586 points. The other columns represent the number of correct points after the calculation software was presented with the 1000 augmented points.

Correct Points	Re-Run	Full Flip	Dominant Flip	Non-Dominant Flip
1000	586	586	526	526

Ultimately, no mistake in the pipeline itself was found. However, we did find that the change in the correctness of some points originated from a difference in the output and input precision of the calculation software. The input precision of Spheno-CPV is 16 digits.² The output was subsequently given in 10 digits. Given that a lot of cpMSSM points are very close to the eEDM limit, such a rounding could make the difference between a correct or incorrect eEDM prediction. It turns out that this difference causes the prediction to become incorrect in about 50% of the cases.

Two small discussion points emerge from this precision difference. Firstly, this no longer makes the acceptance percentage a perfect validation method, as the model could have performed better in this regard if the output precision was set equal to the input precision. However, this mostly means that any acceptance percentage should be seen as a conservative approximation of the model’s capabilities, since logically the acceptance percentage will only go up if the output precision, and thus the model’s data, would have been of higher precision Secondly, this makes replication of the dataset harder, which could be seen as problematic in a scientific sense. However, we note that replication in science mostly is used to determine if very unusual results are true. By improving the dataset using a better output precision, our results should only become better, and thus more unusual in that sense. Thus, we can reasonably ignore this problem for this thesis, but we do however keep it in mind for future research.

²Note: not decimals, digits.

Appendix B

Additional Figures

B.1 Validation Figures Bias-Corrected Model

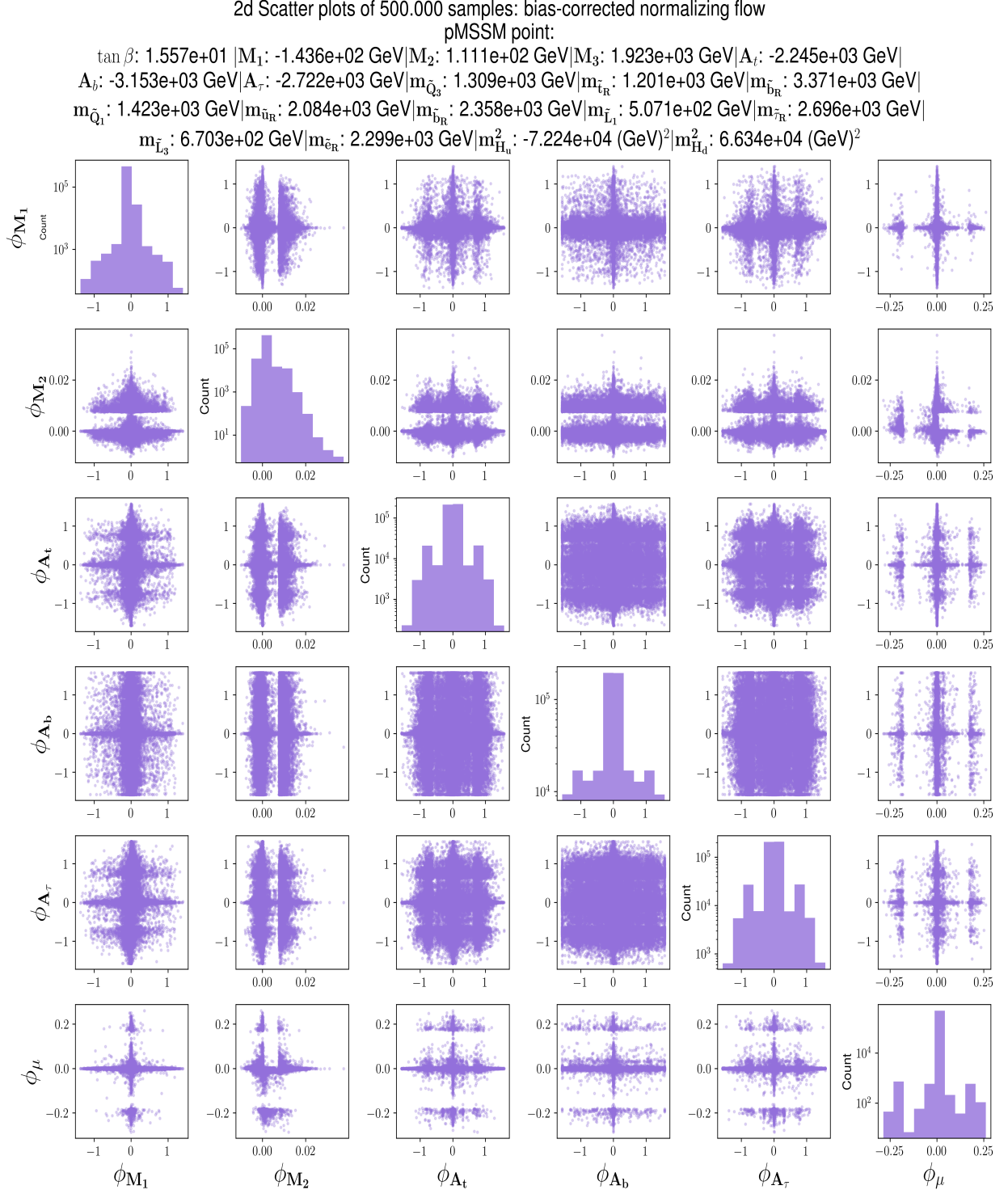


Figure B.1: Scatter plots for each 2-dimensional combination of phases sampled by the bias-corrected normalizing flow. On the ‘diagonal’ are logarithmically scaled histograms of the range of each phase.

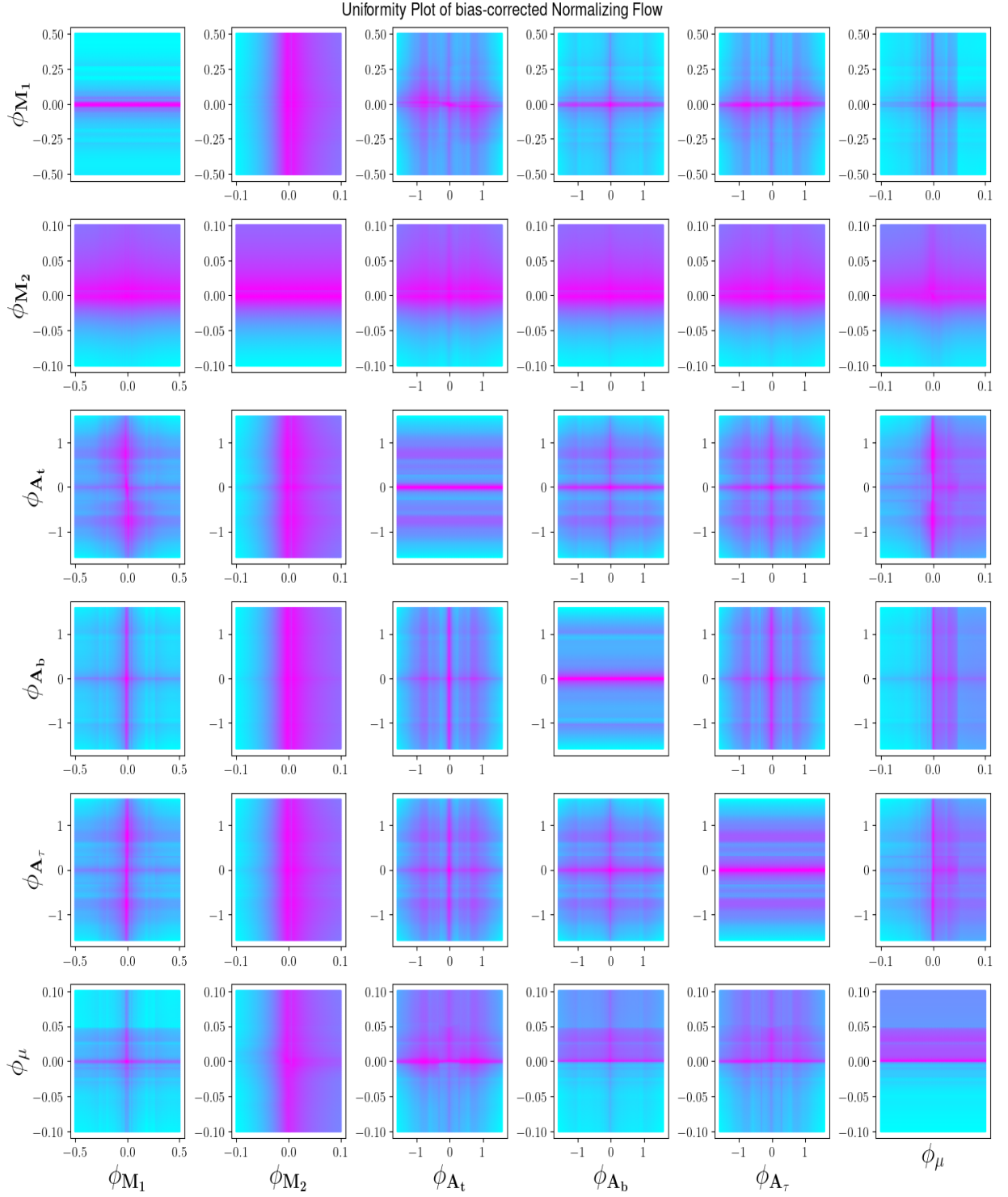


Figure B.2: Uniformity plots for each 2-dimensional combination of phases, where the colour represents the relative likelihood (pink means higher, blue means lower) according to the bias-corrected model for each phase combination using the two non-zero values depicted within the grid. On the ‘diagonal’ there is only one non-zero value for the associated phase.

B.2 Scatter plot for a different correct pMSSM point

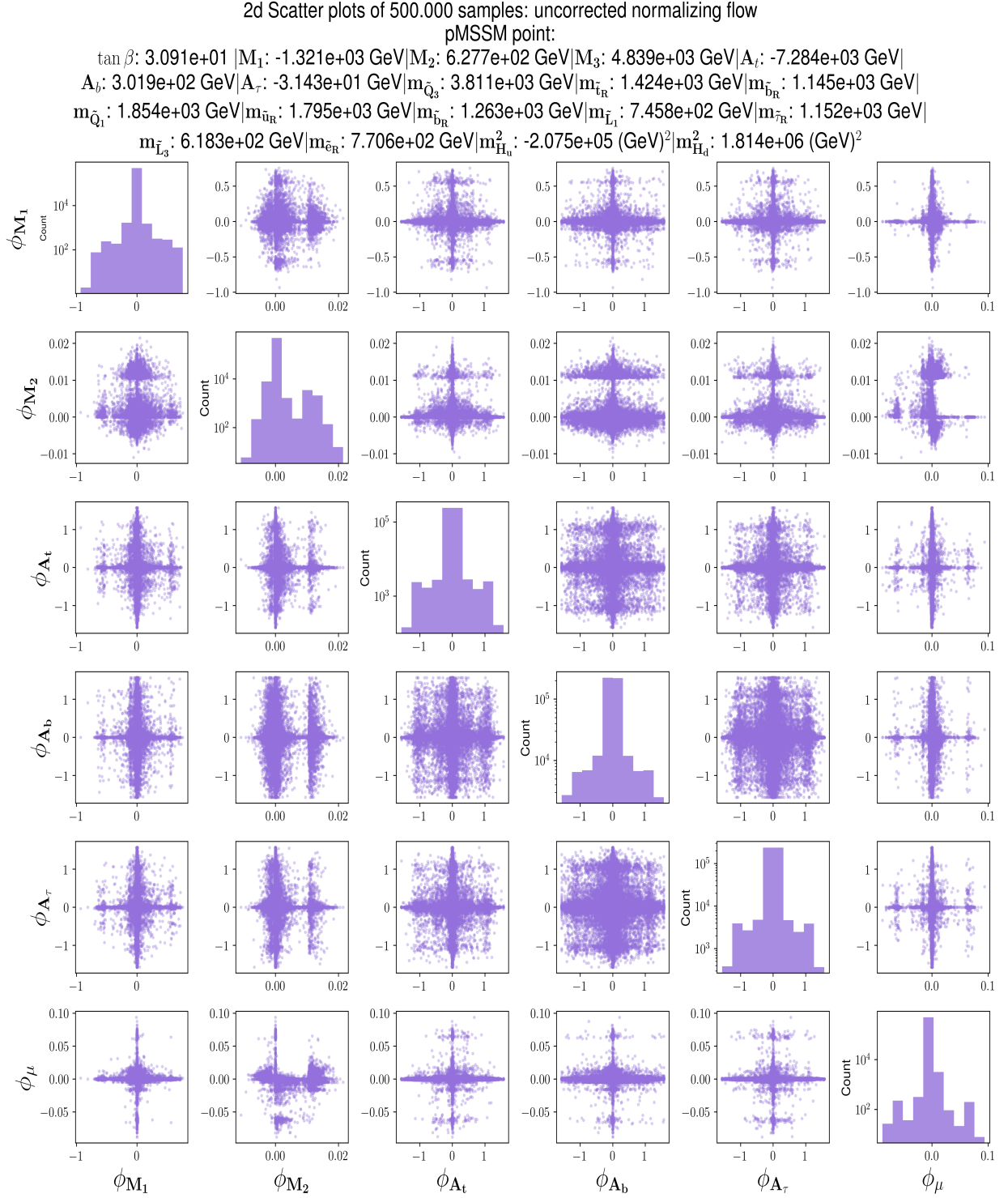


Figure B.3: Scatter plots for each 2-dimensional combination of phases sampled by the uncorrected normalizing flow. On the ‘diagonal’ are logarithmically scaled histograms of the range of each phase. Note that this plot is made for a different original pMSSM point.

Appendix C

Calculation Software

This appendix presents the needed details concerning the calculation software used in this thesis. First a list of the used software packages (including used version) is given in table C.1. Afterwards the pipeline of the calculation is visualized in figure C.1. Lastly, the experimental limits that are used to filter (c)pMSSM points are given in section C.3.

C.1 The Software Packages

Table C.1: Software (packages) used in this thesis, including download links to the webpage on which the used software package can be retrieved. In addition, (*) denotes that LowEnergy.py is not an available software package, but is an in-house code from the PhD thesis of Dr. Marrit Schutten.

Name and Reference	Purpose	Version	URL
Spheno(-CPV) [55]	Generate mass spectrum of (s)particles.	4.0.4	Download
FeynHiggs [56]	Calculation of the Higgs mass(es)	2.18.1	Download
MicrOMEGAs [57]	Calculation of DM observables	5.2.13	Download
LowEnergy.py (*) [17]	Calculation of eEDM and a_u	1.0	N.A.

C.2 Visualization of the internal calculation Pipeline

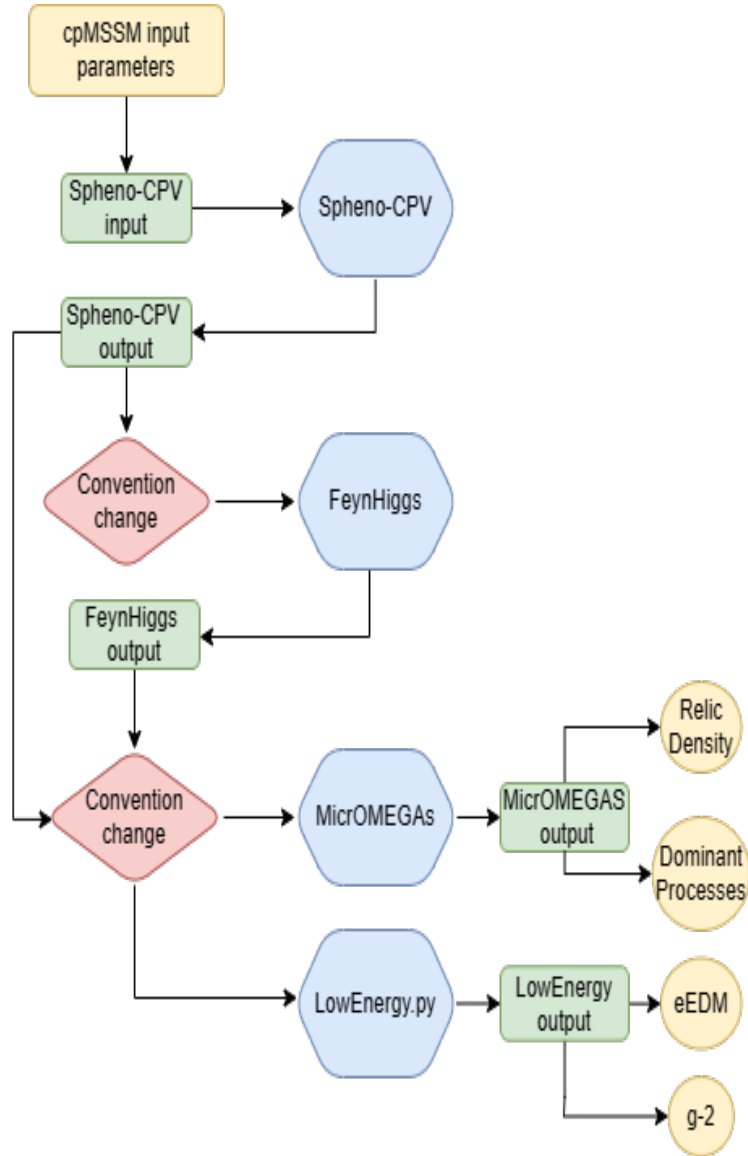


Figure C.1: Visualization of the internal pipeline of the calculation software. This pipeline was set-up by Dr. Marrit Schutten during her PhD thesis [17]. Note the multiple convention changes between the software packages. The LowEnergy.py software is an in-house code.

C.3 Experimental Limits

All limits listed below are required to hold for all correct pMSSM points.

- $(\mathcal{O}_{13})^2 < 0.1$ [58]
- $122 \text{ GeV} < m_{H_1} < 128 \text{ GeV}^1$ [2].
- $m_{\tilde{\chi}_2^0} - m_{\tilde{\chi}_1^0} < 90 \text{ GeV}$ if $m_{\tilde{\chi}_2^0} < m_{\tilde{e}_1}$, LHC (Compressed Search), \tilde{e}_1 refers to the lightest first/second generation non-sneutrino slepton.

¹Note that this range takes into account calculational uncertainties.

- $m_{\tilde{\chi}_1^\pm} > 200$ GeV if $m_{\tilde{\chi}_1^\pm} < m_{\tilde{e}_1}$, LHC (Compressed Search).
- $|m_{\tilde{e}_1} - m_{\tilde{\chi}_1^0}| > 0.00032477704536642546 \cdot m_{\tilde{\chi}_1^0}^2 - 0.251232260566112 \cdot m_{\tilde{\chi}_1^0} + 51.7432725862738$ GeV if $m_{\tilde{e}_1} > 240$ GeV, [59] (Compressed Search).
- $m_{\tilde{u}_1} > 1000$ GeV if $m_{\tilde{\chi}_1^0} < 400$ GeV, LHC, \tilde{u}_1 is the lightest mass eigenstate of first/second generation up-squark.
- $m_{\tilde{d}_1} > 1000$ GeV if $m_{\tilde{\chi}_1^0} < 400$ GeV, LHC, \tilde{d}_1 is the lightest mass eigenstate of first/second generation down-squark.
- $m_{\tilde{g}} > 1800$ GeV if $m_{\tilde{\chi}_1^0} < 800$ GeV, LHC
- $m_{\tilde{g}} > 1100$ GeV if $m_{\tilde{g}} - m_{\tilde{\chi}_1^0} > 100$ GeV, LHC.
- $m_{\tilde{t}_1} > m_{\tilde{\chi}_1^0} + 100$ GeV, LHC, where \tilde{t}_1 is the lightest mass eigenstate of the top squark.
- $m_{\tilde{e}_1} > 95$ GeV, LHC
- $m_{\tilde{\chi}_1^0} < m_{\tilde{\nu}_e}$ and $m_{\tilde{\chi}_1^0} < m_{\tilde{\nu}_\tau}$, LSP related limits: these make sure that the lightest neutralino becomes the LSP.
- $m_{H_2} > 350$ GeV, [15, 60]
- $m_{\tilde{\chi}_2^\pm} > 103.5$ GeV, LEP [61].

The citations for LHC limits are [62, 63, 64, 65, 66]. These specifically link to the ‘SModelS’ software package, which implements these limits. The package itself was not used in this thesis, however the limits of that package were used.

We further note for the above limits that these could potentially be outdated by newer limits. However these limits are used, as they are the most interesting limits for this thesis used within [17]. Thus these limits give the best comparison with earlier work.